ABSTRACT

Title of Dissertation: Bose Einstein Condensates for Analogue Cosmology Experiments

Mónica Gutiérrez Galán
Doctor of Philosophy, 2021

Dissertation Directed by: Professor Gretchen Campbell
Joint Quantum Institute,
National Institute of Standards and Technology,
and
Department of Physics, University of Maryland

This thesis presents the construction and characterization of an experimental apparatus to produce sodium Bose-Einstein condensates (BECs) in arbitrary potentials. Particular attention is devoted to the study of toroidal BECs as platforms for analogue cosmology models.

We also report the first results from this apparatus in which we studied the red-shifting and attenuation of azimuthal phonons in expanding toroidal BECs as well as blue-shifting and amplification of azimuthal phonons in contracting toroidal BECs. The amplification and attenuation of the azimuthal phonons is the result of a non-dissipative friction term that arises from the changing geometry of the background BEC, this non-dissipative friction is analogous to the Hubble friction present in cosmology models.

BOSE EINSTEIN CONDENSATES FOR ANALOGUE COSMOLOGY EXPERIMENTS

by

Mónica Gutiérrez Galán

Dissertation submitted to the Faculty of the Graduate School of the
University of Maryland, College Park in partial fulfillment
of the requirements for the degree of
Doctor of Philosophy
2021

Advisory Committee:
Professor Gretchen Campbell, Co-Chair/Advisor
Professor Ian Spielman
Professor James Williams, Chair
Professor Theodore Jacobson
Professor Ronald Walsworth, Dean's Representative

Dedication

to

Ken Wright,

Mónica Galán Loredo and José Carlos Gutiérrez Fernández

Acknowledgments

I am very grateful for the opportunity of working at the Joint Quantum Institute (JQI) where I have met brilliant, highly motivated, and friendly physicists. Getting to this point in my life would not have been possible without the help and support of so many people; this is not a comprehensive list of all the people that have influenced my career, but I will do my best at acknowledging many of them.

First of all I would like to thank my parents who always encourage me to be curious, even when that meant breaking things around the house. They have always supported me despite being far away. Thanks to my brother who became the family IT guy always helping my parents setup video chats so that we could see each other.

I would like to thank all the teachers that, from an early age, noticed my interest in mathematics and physics and motivated me to continue on a path of constant learning and growth; special thanks to those that let me borrow their physics books to learn beyond what was part of the school curriculum. I am particularly grateful for having had Eduardo Gómez as a professor and advisor at UASLP, his passion for atomic physics and quantum mechanics motivated me to work in an ultra-cold atoms laboratory.

I am very grateful to Gretchen Campbell for letting me form part of the ErNa team and for her advice and patience when things in the laboratory did not work

as expected. She has always given us the freedom to experiment and play around with ideas in the laboratory, which has been fundamental in developing a sense of confidence and independence in my work as a physicist. In addition to Gretchen's advice we were lucky to have the advice of another great physicist, Ian Spielman, who for many years now has joined our group meetings and shared his knowledge with us.

Very special thanks to Luis Orozco, he is the reason why the JQI was ever on my radar. He has done a magnificent job opening a path for latinamerican students to pursue advanced degrees in physics in the US—and frankly speaking all around the world!—. His stories and advice are always plentiful, and his amazing taste in food was constantly appreciated.

Building a laboratory is not an easy task, this work would not have been possible without the collaboration of all my lab mates—the ErNa team—, Swarnav Banik, Madison Anderson and Hector Sosa, and the never ending advice of former graduate student Avinash Kumar and former postdoc Steve Eckel. We were lucky to have a sibling laboratory, Gretchen's Sr lab, full of graduate students with vast expertise building an ultra-cold atoms experiment and whose advise continues to be helpful. Thank you, Neal Pisenti, Dan Barker and Ben Reschovsky, and to the younger generation, Peter Elgee and Ananya Sitaram. There were, of course, all the CPRK[1] members who have offered their help and advice over the years. Special thanks to Alessandro Restelli whose expertise in electronics is greatly appreciated.

Being at an institution like UMD has been a great opportunity to meet bright

[1]Named after professors Campbell, Porto, Rolston, and Kollár.

scientists from all around the world. I was very lucky to be a graduate student at the same time as many other latinamerican graduate students, their friendship and shared love for tacos made it easier to be far from México. Thank you, Ana, Paco, Dalia, David, Kristel, Israel and Carlos. I was also very lucky to make great friends from Russia, Natalia Pankratova and Artur Peralov; and from Greece, Antonis Kyprianidis. I will always cheerish your friendship!

One of the most hard working physicists I have ever met is Ken Wright, I would not have survived grad-school without his support. He has been a great partner, always helping me stay positive and forcing me to enjoy life outside the lab. Last but not least, thanks to Ella and Lola who managed to turn a bad day into a joyful day as soon as I got home.

This work was supported by the National Science Foundation through the Physics Frontier Center at the JQI.

Table of Contents

List of Tables

List of Figures

List of Abbreviations

AOM	Acousto-Optic Modulator
BEC	Bose-Einstein Condensate
CCD	Charge-Coupled Device
DMD	Digital Micromirror Device
EMCCD	Electron-Multiplying CCD
FWHM	Full Width at Half Maximum
GPE	Gross-Pitaevskii Equation
IR	Infrared
JQI	Joint Quantum Institute
MOT	Magneto-Optical Trap
NA	Numerical Aperture
NI	National Instruments
NIST	National Institute of Standards and Technology
OD	Optical Density
ODT	Optical Dipole Trap
PBS	Polarizing Beam Splitter
PCA	Principal Component Analysis
PD	Photodiode
PSF	Point Spread Function
PTAI	Partial Transfer Absorption Imaging
RF	Radio Frequency
SRS	Stanford Research Systems
TEM	Transverse Electro-Magnetic
TF	Thomas-Fermi
UHV	Ultra-High Vacuum

Chapter 1: Introduction

While the study of astrophysical systems is sometimes thought of as limited to astronomical observations, there are many experiments that elucidate different aspects of the cosmos, starting with the study of spectroscopic lines to identify elements in distant stars [2] to the more recent developments of tabletop systems where it is possible to study phenomena predicted and studied by general relativity. There are a variety of physical platforms that enable the study of relativistic phenomena under well-controlled laboratory conditions, including but not exclusive to, classical fluids [3, 4], optical fibers [5, 6], semiconductor microcavities [7], superconducting circuits [8], ion traps [9], and cold atomic systems [10]. Some of the recent experiments in the field of analogue cosmology include the realization of acoustic black hole horizons [3, 5, 7]; stimulated and spontaneous Hawking radiation [6, 11, 12]; and scattering processes around rotating black holes [13]. Ultracold atoms, with their unprecedented control and measurement capabilities, are an emerging platform for realizing minimal models in the context of high energy physics [14], astrophysics [15, 16, 17, 18], and cosmology [19, 20, 21, 22].

This thesis presents the construction and characterization of the experimental apparatus used to produce toroidal Bose-Einstein condensates (BECs) as well as

the techniques to study cosmology analogues in expanding and contracting toroidal BECs.

Chapter 2 reviews the basic theory that describes BECs in dilute atomic gases, as well as a brief discussion of the connection between BECs and cosmological models.

Chapter 3 describes the interactions between Alkalai atoms and electromagnetic fields. The description is presented in the context of laser and magnetic cooling and trapping of neutral atoms which forms the basis of tools to engineer BECs for analogue cosmological experiments.

While chapter 4 presents an overview of the experimental apparatus built to produce BECs, chapter 5 combines the techniques from chapter 3 with the tools developed in chapter 4 to produce toroidal BECs and to generate azimuthal phononic modes in the BECs.

Finally, chapter 6 presents the experimental results from our publication in preparation, "Hubble Attenuation and Amplification in Expanding and Contracting Cold-Atom Universes". In this work, we studied the red-shifting and attenuation of azimuthal phonons in expanding toroidal BECs as well as the time reversed process, contraction of toroidal BECs, which results in blue-shifting and amplification of azimuthal phonons.

Appendix A presents a detailed description of the design and construction of the imaging and projection optics as well as their characterization.

Appendix B summarizes a (non-comprehensive) list of aspects of our experimental system that offer vast room for improvement.

Chapter 2: Theoretical Background

Almost a century ago Einstein [23], based on the work of Bose [24], predicted the existence of a new state of matter now known as a Bose Einstein Condensate (BEC). London proposed, in 1938, [25] superfluidity and superconductivity as examples of BEC, however, experimental realization of a dilute atomic-gas BEC did not happen until several decades later [26, 27]. Since then, the theoretical understanding of BECs has become a fruitful field in physics [28, 29], and the techniques that were developed to create these dilute atomic-gas condensates [30] form part of the toolbox used to study new phenomena beyond traditional atomic, molecular and optical (AMO) physics with BECs as the experimental platform.

The general approach to understanding the phenomena of Bose-Einstein condensation in an ideal gas of bosons—meaning uniform and non-interacting— in 3D can be found in most graduate-level statistical mechanical books [31, 32, 33, 34], a summarized version of the derivations will be presented in section 2.1. Understanding the same many-body system in which weak interactions, meaning small coupling, between particles are taken into account leads to the development of Bogoliubov's theory of superfluidity [35]. If in addition to weak interactions between particles we consider the case in which there is an external potential, e.g. a confining potential,

we arrive at the derivation of the Gross-Pitaevskii equation (section 2.2).

The Gross-Pitaevskii equation (GPE) describes a dilute gas of bosons at zero temperature and provides the framework for studing superfluidity in BECs. It has been of interest in recent years to use BECs as a platform to study physical phenomena that is described by equations analogous to those that describe the physics of a superfluid, this phenomena includes models relevant to high energy physics [14], astrophysics [15, 16, 17, 18], and cosmology [19, 20, 21, 22]. We are currently interested in studying physics that relates to the inflationary stage of the early universe and in section 2.3 we will derive the equations that describe the evolution of elementary excitations in a condensate which are analogous to the equations that describe the evolution of elementary excitations of the vacuum in cosmological systems.

2.1 The Ideal Bose-Einstein Gas

The theory of Bose-Einstein condensation in a uniform gas of identical, non-interacting bosonic particles follows the derivations found in Refs. [31, 32, 33, 34]. This derivation begins with the grand canonical ensemble which assumes a system that can exchange energy and particles with a reservoir. The system and the reservoir exist in thermal equilibrium and are in equilibrium with respect to particle exchange. The thermodynamical variables that facilitate the description of such systems are the temperature (T) and chemical potential (μ) of the system. The chemical potential in this context can be understood as the energy required to add

or remove a particle from the system and is defined by

$$\mu = \left(\frac{\partial E}{\partial N}\right)_{S,V}, \tag{2.1}$$

where E is the internal energy of the system, S is its entropy, V is its volume and N is the number of particles.

Deriving the thermodynamic properties of the system requires knowledge of the grand canonical partition function, which in turn depends on the probability distribution function for the occupation of the energy levels of the system. In the classical limit (high temperature, low phase-space density) the distribution function takes the form of the Maxwell-Boltzmann distribution in terms of the continuous energy variable ε, $f_T(\varepsilon) = \exp\left[(\mu - \varepsilon)/k_B T\right]$, with k_B the Boltzmann constant. In the low temperature, high phase-space density regime, the thermal de Broglie wavelength ($\lambda_{\mathrm{T}} = \sqrt{2\pi\hbar^2/Mk_B T}$, with M the mass of a particle and $\hbar$ the reduced Plank constant) becomes comparable to the interatomic separation, in this regime the quantum nature of the particles must be taken into account through the Bose distribution

$$f_B(\varepsilon_j) = \left[\exp\left(\frac{\varepsilon_j - \mu}{k_B T}\right) - 1\right]^{-1}, \tag{2.2}$$

where ε_j is the energy of the j-th state. In general $f_B(\varepsilon_j) \geq 0 \ \forall \ j$, the particular case of the ground state, nominally $j = 0$, sets the condition $\mu = \varepsilon_0$.

The condition for condensation, as well as the critical temperature at which it occurs (T_c), can be found by setting $N_e(T_c, \mu = \varepsilon_0) = N$, were $N_e = \sum_{j \neq 0} f_B(\varepsilon_j)$ are

the particles in all excited states, $N = N_0 + N_e$ the total number of particles, and N_0 the number of particles in the ground state. Assuming that the energy of the system ($k_B T$) is much larger than the typical separation between energy states allows us to approximate the summation by an integral, $N_e = \int_0^\infty g(\varepsilon)\, f_B(\varepsilon)\, \mathrm{d}\varepsilon$. Here, $g(\varepsilon)$ is the density of states which can be calculated given the Hamiltonian of the system as follows: let $G(\varepsilon)$ be the total number of energy states available with energy equal to or smaller than ε, then the density of states is $g(\varepsilon) = \mathrm{d}G(\varepsilon) \,/\, \mathrm{d}\varepsilon$. We will derive the solutions for two cases of interest: particles in a box and particles in a harmonic oscillator potential (see for example [36, 37]).

Particles in a box. Consider particles with mass M in a d-dimentional box with volume $V = L^d$, L is the length of the box. The energy eigenvalues $\varepsilon(k) = \hbar^2 k^2 / 2M$ can be represented as points in a discrete grid in k-space[1], then the number of available energy levels and the density of states are given by

$$G(k) = \frac{V}{(2\pi)^d}\Omega_d(k) \quad \longrightarrow \quad g(\varepsilon) = \frac{Vd}{2}\left[\frac{M}{2\pi\hbar^2}\right]^{d/2} \frac{\varepsilon^{d/2-1}}{\Gamma(d/2+1)}. \tag{2.3}$$

Here $\Omega_d(k)$ is the volume of a d-sphere in k-space and Γ is the gamma function[2].

Particles in a harmonic potential. Consider a harmonic potential in d-dimensions. The energy eigenvalues are $\varepsilon = \sum_{j=1}^{d}(n_j + 1/2)\hbar\omega_j$ where j labels the dimension and n_j is the number of particles in the j-th mode with angular frequency

[1] The dimensionality of the k-space is also d.

[2] Mathematical curiosity: the Γ function in Eq. (2.3) arises from integrating the volume of a d-sphere.

System	η	$\Gamma(\eta)$	$\zeta(\eta)$
Box in 1D	$1/2$	$\sqrt{\pi}$	-1.46
Box in 2D	1	1	∞
Box in 3D	$3/2$	$\sqrt{\pi}/2$	2.612
HO in 1D	1	1	∞
HO in 2D	2	1	$\pi^2/6$
HO in 3D	3	2	1.202

Table 2.1: Values of η and corresponding $\Gamma(\eta)$ and $\zeta(\eta)$ for particles in a box and in a harmonic potential up to dimension 3.

ω_j, then

$$G(\varepsilon) = \frac{\varepsilon^d}{d! \prod_j (\hbar\omega_j)} \quad \longrightarrow \quad g(\varepsilon) = \frac{\varepsilon^{d-1}}{\Gamma(d) \prod_j (\hbar\omega_j)}. \tag{2.4}$$

Generally, the density of states can be written as $g(\varepsilon) = C_\eta \varepsilon^{\eta-1}$, where C_η is a constant and η depends on on the geometry of the system. We can rewrite the condition $N = N_e(T_c, \mu = 0)$ to determine the critical temperature as

$$\begin{aligned} N &= \int_0^\infty \mathrm{d}\varepsilon \, \frac{C_\eta \varepsilon^{\eta-1}}{\exp(\varepsilon/k_B T_c) - 1}, \\ &= C_\eta \left(k_B T_c\right)^\eta \int_0^\infty \mathrm{d}u \, \frac{u^{\eta-1}}{e^u - 1}, \\ &= C_\eta \Gamma(\eta) \zeta(\eta) \left(k_B T_c\right)^\eta, \end{aligned} \tag{2.5}$$

where $u = \varepsilon/k_B T_c$ is a change of variables used for integration and $\zeta(\eta)$ is the Reimann zeta function. From this expression we find the critical temperature

$$k_B T_c = \left(\frac{N}{C_\eta \Gamma(\eta) \zeta(\eta)} \right)^{1/\eta}. \tag{2.6}$$

Table 2.1 shows the values of η and corresponding $\Gamma(\eta)$ and $\zeta(\eta)$ for particles in a box

and particles in a harmonic potential. The value of C_η for particles in a d-dimensional box is found from Eq.(2.3), $C_\eta = (Vd/2)(M/2\pi\hbar)^{d/2}$; for particles in a d-dimensional anisotropic harmonic potential we find from Eq.(2.4) that $C_\eta = (\prod_j^d \hbar\omega_j)^{-1}$ where j labels the dimension. The cases of a 2D-box and a 1D-harmonic potential are interesting in that $\zeta(\eta = 1)$ diverges, thus condensation can only occur at $T_c = 0$. By contrast, systems with $T_c > 0$ exhibit Bosonic stimulation [38] which refers to how, even though the system at T_c has enough energy to occupy excited energy levels, having atoms in the ground state favors further accumulation of atoms in the ground state due to bosonic quantum statistics. In general, the number of atoms that are in the condensed state, $N_0 = N - N_e$, is

$$N_0 = N\left[1 - \left(\frac{T}{T_c}\right)^\eta\right]. \tag{2.7}$$

2.2 Weakly-Interacting Bose Gas

The theory of Bose-Einstein condensation presented in the previous section, while illustrative, does not fully represent atomic gases like sodium in which interactions exist between atoms. The solution to the weakly-interacting Bose gas problem was first derived by Bogoliubov [35], the general approach can be found in [28, 29] and assumes that:

1. The gas is at $T = 0$.

2. The gas is rarified, the condition for diluteness being $|a| \ll n^{-1/3}$ where a is the s-wave scattering length and $n = N/V$ is the number density of the gas.

The first assumption allows us to consider only slow particles in the derivations, the second assumption allows us to ignore interactions between more that two particles. Together, the assumptions justify describing the weak interactions between particles in terms of the two-particle s-wave scattering length characterized by a (see for example [36, 37]).

The problem at hand concerns the large number of particles, in experimental settings, N is typically of the order 10^5 to 10^6 atoms, a mean-field approach simplifies the many-body wave function expressing it in terms of a single-particle wave function. Then, the Hamiltonian of the system can be written in the notation of the second quantization as

$$\begin{aligned}\hat{H} = &\int \mathrm{d}\mathbf{r}\hat{\Psi}^\dagger(\mathbf{r})\left[-\frac{\hbar^2}{2M}\nabla^2 + V_{\mathrm{ext}}(\mathbf{r},t)\right]\hat{\Psi}(\mathbf{r}) \\ &+ \frac{1}{2}\int \mathrm{d}\mathbf{r}\mathrm{d}\mathbf{r}'\hat{\Psi}^\dagger(\mathbf{r})\hat{\Psi}^\dagger(\mathbf{r}')\,V(\mathbf{r}-\mathbf{r}')\,\hat{\Psi}(\mathbf{r}')\,\hat{\Psi}(\mathbf{r}). \end{aligned} \tag{2.8}$$

With M the mass of a particle, V_{ext} the external potential, $V(\mathbf{r}-\mathbf{r}')$ the interaction potential and $\hat{\Psi}^\dagger$ the bosonic creation field operator which is normalized to the total number of particles, $N = \int_0^\infty \mathrm{d}\mathbf{r}\left\langle\hat{\Psi}^\dagger(\mathbf{r})\hat{\Psi}(\mathbf{r})\right\rangle$. The first integral in Eq. (2.8) corresponds to the Hamiltonian of the system in the absence of interactions, the second integral models the interactions of the particles in terms of a two-body potential V.

The field operator in the Heisenberg representation satisfies the equation

$$
\begin{aligned}
i\hbar\partial_t\hat{\Psi}^\dagger(\mathbf{r},t) &= \left[\hat{\Psi}^\dagger(\mathbf{r},t), \hat{H}\right], \\
&= \left[-\frac{\hbar^2}{2m}\nabla^2 + V_{\text{ext}}(\mathbf{r},t) + \int \mathrm{d}\mathbf{r}'\hat{\Psi}^\dagger\left(\mathbf{r}',t\right) V\left(\mathbf{r}'-\mathbf{r}\right)\hat{\Psi}\left(\mathbf{r}',t\right)\right]\hat{\Psi}(\mathbf{r},t).
\end{aligned}
\tag{2.9}
$$

The first simplification to this equation comes from the Bogoliubov approximation where we consider that the condensate fraction is large, $N_0/N \sim 1$, and replace the field operator with the mean value and a small fluctuating field $\hat{\Psi}(\mathbf{r},t) = \Psi_0(\mathbf{r},t) + \hat{\Phi}(\mathbf{r},t)$. Here, Ψ_0 is a complex number (and a classical field) representing the ground state wave function, $\hat{\Phi}(\mathbf{r},t)$ represents the non-condensed component of the field operator and is treated as a small perturbation.

The second approximation used in simplifying Eq. (2.9) takes into account the diluteness of the atomic cloud and the fact that at $T < T_c$ only particles with small momentum play a role, this justifies substituting the interatomic potential $V(\mathbf{r}-\mathbf{r}')$ by a "soft" potential $V_{\text{eff}}(\mathbf{r})$ that results in the same value of a, the scattering length[3]. Then, we can rewrite the interaction term in Eq. (2.9) as

$$
\begin{aligned}
\hat{H}_I &= \int \mathrm{d}\mathbf{r}'\hat{\Psi}^\dagger\left(\mathbf{r}',t\right) V\left(\mathbf{r}'-\mathbf{r}\right)\hat{\Psi}\left(\mathbf{r}',t\right), \\
&= g\left|\hat{\Psi}(\mathbf{r},t)\right|^2,
\end{aligned}
\tag{2.10}
$$

where $g := 4\pi\hbar^2 a/M$ is the interaction coupling constant. Using Eq. (2.9) and (2.10)

[3]The purpose of a "soft" potential is to allow integrability of the Schrödinger equation that would otherwise diverge for $r \to 0$ for typical interatomic potentials of the form $V(r) \propto \left(1/r^2 - 1/r^6\right)$.

and the Bogoliubov approximations result in the equation

$$i\hbar\,\partial_t\Psi_0(\mathbf{r},t) = \left[\frac{-\hbar^2}{2m}\nabla^2 + V_{\text{ext}}(\mathbf{r},t) + g|\Psi_0(\mathbf{r},t)|^2\right]\Psi_0(\mathbf{r},t). \tag{2.11}$$

Equation (2.11) is known as the time-dependent Gross-Pitaevskii equation (GPE) after Gross [39] and Pitaevskii [40] who independently derived the equation in the context of superfluid liquid ^{4}He.

Let us consider an external potential that does not depend on t, then we can write the the ground state wave function as

$$\Psi_0(\mathbf{r},t) = \psi_0(\mathbf{r})\exp\left(\frac{-i\mu t}{\hbar}\right), \tag{2.12}$$

where $\mu = \partial E/\partial N$ is the chemical potential and the wavefunction satisfies the normalization condition $\int \mathrm{d}\mathbf{r}\,|\psi_0(\mathbf{r})|^2 = N$. Then, $|\psi_0(\mathbf{r})|^2 = n(\mathbf{r})$, where $n(\mathbf{r})$ is the number density. Equation (2.11) and (2.12) yield the time-independent GPE

$$\left[\frac{-\hbar^2\nabla^2}{2m} + V_{\text{ext}}(\mathbf{r}) - \mu + g\,|\psi_0(\mathbf{r})|^2\right]\psi_0(\mathbf{r}) = 0. \tag{2.13}$$

Equation (2.13) admits multiple solutions, the one with the lowest energy plays the role of order parameter of the condensate, for a specific choice of the overall phase this solution is typically a real function. In contrast, the higher energy solutions corresponding to excited states are usually complex functions.

The ground state solution for $V_{\text{ext}}(\mathbf{r}) = 0$ corresponds to the zero momentum state, in the momentum basis $|\psi_0(\mathbf{p})|^2 = N\delta(\mathbf{p})$. The energy of the ground state is

$E_0 = N^2 g/2V$. From the expression for the energy of the condensate we can derive a quantity that will be of importance in describing the low momentum excitation spectrum[4] of the condensate in section 2.2.3, namely the speed of sound, which is defined in terms of the mass density ($\rho = Mn$) as

$$c^2 = \frac{\partial P}{\partial \rho} = \frac{\partial}{\partial \rho}\left(-\frac{\partial E_0}{\partial V}\right) = \frac{\rho g}{M^2} \tag{2.14}$$

There are two characteristic lengths of importance when studying condensates, the first one—introduced earlier in this chapter—is the thermal de Broglie wavelength which determines the distance over which quantum statistics become relevant; the second one, known as the healing length, is the characteristic length over which the wave function of the condensate varies. The healing length is defined through the relation $\hbar^2/2M\xi^2 = ng$, where the kinetic energy per particle is equated to the bulk interaction energy. Then,

$$\xi = \sqrt{\frac{1}{8\pi n a}}. \tag{2.15}$$

2.2.1 Thomas-Fermi Approximation

Let us consider two cases of interest regarding the time-independent GPE. First, we note that in the absence of interactions, i.e. $g = 0$, Eq. (2.13) reduces to the time-independent Schrödinger equation. On the other hand, when the interaction energy ($g\,|(\psi_0)|^2$) is much higher than the ground state kinetic energy, we can ignore

[4] In the low momentum (p) regime the dispersion relation of the elementary excitations is approximately linear in p.

the contribution of the latter,

$$V_{\text{ext}}(\mathbf{r}) - \mu + g\, n(\mathbf{r}) = 0. \tag{2.16}$$

This equation is known as the Thomas-Fermi (T-F) approximation of the GPE and shows that the density distribution resembles the shape of the confining potential.

The implications of the T-F approximation can be studied by considering a BEC confined by an isotropic harmonic potential[5], $V_{\text{ext}}(\mathbf{r}) = M\omega^2 r^2/2$. At the edge of the condensate ($r = r_{\text{TF}}$) the density vanishes and Eq. (2.16) results in $V(r_{\text{TF}}) = \mu$, this condition is used to define the Thomas-Fermi width (or radius) of the condensate, in this case $r_{\text{TF}} = \sqrt{2\mu/M\omega^2}$. On the other hand, at the center of the condensate ($r = 0$) the external potential vanishes and we find $\mu = gn_0$, where n_0 is the peak density of the condensate. In this context the chemical potential can be understood as the value of the mean-field interaction at peak density.

2.2.2 Hydrodynamic Equations

There are a couple of conservation laws associated with the time-dependent GPE. Let us write the condensate field function as

$$\Psi_0(\mathbf{r}, t) = \sqrt{n(\mathbf{r}, t)}\, \exp[i\phi(\mathbf{r}, t)], \tag{2.17}$$

[5]The choice of a harmonic potential is not arbitrary, it is rather a pragmatic choice since experimentally BECs are typically produced in harmonic traps. The isotropy of the potential is chosen to simplify the derivations.

with $\phi(\mathbf{r},t)$ the phase of the condensate. The first quantity to be conserved, derived from the normalization condition for $\Psi_0(\mathbf{r},t)$, is mean particle number

$$N = \int_0^\infty \mathrm{d}\mathbf{r}\,|\Psi_0(\mathbf{r},t)| = \int_0^\infty \mathrm{d}\mathbf{r}\,n(\mathbf{r},t). \tag{2.18}$$

The second conservation law relates to the condensate current density, defined as

$$\begin{aligned}\mathbf{j}(\mathbf{r},t) &= -\frac{i\hbar}{2M}\left(\Psi_0^*\nabla\Psi_0 - \Psi_0\nabla\Psi_0^*\right), \\ &= n(\mathbf{r},t)\,\frac{\hbar\nabla\phi(\mathbf{r},t)}{M}, \\ &= n(\mathbf{r},t)\,\mathbf{v}_s(\mathbf{r},t);\end{aligned} \tag{2.19}$$

where we have introduced the velocity of the condensate flow, $\mathbf{v}_s(\mathbf{r},t) = \hbar\nabla\phi(\mathbf{r},t)/M$. We find from Eq. (2.11) that density of the condensate satisfies the continuity equation

$$\partial_t n(\mathbf{r},t) + \nabla\cdot\mathbf{j} = 0. \tag{2.20}$$

From Eq. (2.18), (2.19) and (2.20) follows that $\nabla \times \mathbf{v}_s = 0$, which implies that the condensate is irrotational[6].

Using the explicit form of Ψ_0 [Eq. (2.17)] and and the time independent GPE [Eq. (2.11)] we find

$$\hbar\partial_t\phi + \left[\frac{M\mathbf{v}_s^2}{2} + V_{\text{ext}} + gn - \frac{\hbar^2}{2M\sqrt{n}}\nabla^2\sqrt{n}\right] = 0. \tag{2.21}$$

[6] A common feature of superfluids is being irrotational.

The last term inside the square brackets is known as the quantum pressure and arises from the kinetic energy associated with the curvature of the wave function, the length scale over which the wave function changes in the BEC is the healing length (ξ) defined by Eq. (2.15).

2.2.3 Elementary Excitations

The low-energy excitations of a Bose gas can be studied as small oscillations around the equilibrium state, these excitations play a crucial role in the physics of a condensate [41]. Consider the trial function $\Psi_0(\mathbf{r},t) = \Psi'(\mathbf{r},t)\mathrm{e}^{-\mathrm{i}\mu t/\hbar}$ with $\Psi'(\mathbf{r},t) = \psi_0(\mathbf{r}) + \delta\psi(\mathbf{r},t)$, where $\delta\psi$ is a small perturbation of the from

$$\delta\psi(\mathbf{r},t) = \sum \left[u_i(\mathbf{r})\mathrm{e}^{-\mathrm{i}\omega_i t} + v_i^*(\mathbf{r})\mathrm{e}^{\mathrm{i}\omega_i t}\right], \tag{2.22}$$

here ω_i is the frequency of the oscillation. Using the trial function and the time-dependent GPE [Eq. (2.11)] we find a set of differential equations for $u_i(\mathbf{r})$ and $v_i(\mathbf{r})$,

$$\begin{bmatrix} \hat{H}' & g\left(\Psi_0(\mathbf{r})\right)^2 \\ g\left(\Psi_0^*(\mathbf{r})\right)^2 & \hat{H}' \end{bmatrix} \begin{bmatrix} u_i(\mathbf{r}) \\ v_i(\mathbf{r}) \end{bmatrix} = \hbar\omega_i \begin{bmatrix} u_i(\mathbf{r}) \\ -v_i(\mathbf{r}) \end{bmatrix}, \tag{2.23}$$

with $\hat{H}' = -\left(\hbar^2/2m\right)\boldsymbol{\nabla}^2 + V_{\mathrm{ext}}(\mathbf{r}) - \mu + 2gn(\mathbf{r})$.

The solution to Eq. (2.23) depends on the confining potential and may not necessarily have an analytical solution. One instance where an analytical solution does exist is the case of the uniform Bose gas, $V_{\mathrm{ext}} = 0$, in this case $\mu = gn$ and

$\Psi_0 = \sqrt{n}$. Using the ansatz $u(\mathbf{r}) = u \exp(i\,\mathbf{k}\cdot\mathbf{r})$ and $v(\mathbf{r}) = v \exp(i\,\mathbf{k}\cdot\mathbf{r})$ we find

$$(\hbar\omega)^2 = \left(\frac{\hbar^2 k^2}{2M}\right)^2 + \frac{\hbar^2 k^2}{M} gn, \tag{2.24}$$

which can be rewritten in terms of the energy ($\epsilon = \hbar\omega$) and momentum ($\mathbf{p} = \hbar\mathbf{k}$) of the excitations,

$$\epsilon\,(p) = \sqrt{\left(\frac{p^2}{2M}\right)^2 + (cp)^2} \tag{2.25}$$

where c is the speed of sound defined in Eq. (2.14). The dispersion relation of the low momenta solutions can be approximated by $\epsilon(p) \approx cp$, which corresponds to phononic excitation modes. Conversely, the high momenta solutions resemble the free-particle solution with $\epsilon(p) \approx p^2/2M$.

Consider a condensate in a harmonic potential

$$V_{\text{ext}}(\boldsymbol{r}) = \frac{1}{2}M\omega_x^2 x^2 + \frac{1}{2}M\omega_y^2 y^2 + \frac{1}{2}M\omega_z^2 z^2. \tag{2.26}$$

The characteristic length of the harmonic oscillator is $a_{HO} = \sqrt{\hbar/M\bar{\omega}}$, with $\bar{\omega} = (\omega_x\,\omega_y\,\omega_z)^{1/3}$. In the T-F limit ($Na/a_{\text{HO}} \gg 1$) the quantum pressure term in Eq. (2.21) can be neglected and the hydrodynamic equations [Eq. (2.20) and (2.21)] can be linearized for the perturbation $\delta n = n - n_0$, with n_0 the equilibrium density, yielding

$$\frac{\partial^2}{\partial t^2}\delta n = \boldsymbol{\nabla}\cdot\left[c^2(\boldsymbol{r})\boldsymbol{\nabla}\delta n\right]. \tag{2.27}$$

If the harmonic confinement is isotropic ($\bar{\omega} = \omega_i\,\forall i$), we expect the density

perturbation will have spherical symmetry, then $\delta n(\boldsymbol{r}) = P_\ell^{(2n_r)}(r/r_{\rm TF})r^\ell Y_{lm_l}(\theta,\phi)$, with $P_l^{2n_r}$ polynomial functions, n_r the radial quantum number, l the angular momentum and m_l its projection along $\hat{e}_z$. Using this ansatz in Eq. (2.27) we obtain the dispersion relation

$$\omega\left(n_r,\ell\right) = \bar{\omega}\left(2n_r^2 + 2n_r\ell + 3n_r + \ell\right)^{1/2} \tag{2.28}$$

for the normal modes of the condensate in the harmonic trap. The dipole mode[7] $(n_r = 0, l = 1)$ with $\omega = \bar{\omega}$ corresponds to oscillations of the center of mass of the condensate which are decoupled from the internal degrees of freedom of the system. The dipole mode derivation can be generalized to anisotropic potentials (in this case m_l remains a good quantum number but different l values are coupled), resulting in oscillation of the center of mass along each trapping direction at the corresponding trapping frequency. This result is particularly useful in the laboratory to determine the harmonicity of the trap [42] and the trapping frequency [43].

2.3 Bose Einstein Condensates for Analogue Cosmology

There are certain similarities between the physics of a system comprised of weakly-interacting massive-bosons and a system comprised of non-interacting massless-bosons, namely photons [28]. In the case of massive-bosons, a large occupation of a particular state allows us to describe the system in terms of the classical field Φ, as opposed to the quantum field $\hat{\Phi}$. Similarly, a large occupation number of a

[7] Also known as sloshing mode.

particular mode in a system of photons allow us to describe the system in terms of the classical electromagnetic field E, as opposed to the quantum field operator $\hat{a}$. Whereas Maxwell's equations govern the evolution of the classical electromagnetic field, the Gross-Pitaevskii equation governs the evolution of the classical field Ψ_0.

We derive in this section the equation that governs the evolution of azimuthal phonons in an expanding toroidal BEC, this equation resembles the field equation for a minimally coupled massless scalar field in an expanding homogeneous universe [44, 45]. The evolution of the scalar field in an expanding universe exhibits red-shifting, and attenuation due to "Hubble friction". The concept of Hubble friction refers to a term that arises from the changing metric of the universe, however, it is not a real dissipative friction. If time is reversed in the system—implying a contracting universe as opposed to an expanding universe—the term coined as Hubble friction will reverse sign, therefore amplifying the scalar field.

2.3.1 Evolution of a Phonon in an Expanding Ring Trap

The equations that govern the evolution of phononic excitations in a background condensate can be derived from the action for the Gross-Pitaevskii wave function [44, 46]. Using Eq. (2.11) we can write the action of the field Ψ_0 defined in Eq. (2.17) as

$$S = \int \mathrm{d}t\, \mathrm{d}\mathbf{r} \left[i\hbar\Psi_0^*\partial_t\Psi_0 - \frac{\hbar^2}{2M}\boldsymbol{\nabla}\Psi_0^* \cdot \boldsymbol{\nabla}\Psi_0 - V(\mathbf{r},t)\left|\Psi_0\right|^2 - \frac{g}{2}\left|\Psi_0\right|^4 \right]. \tag{2.29}$$

Phonons can be thought of as a small perturbations in the density and phase of the background BEC,

$$\begin{aligned} n(\mathbf{r},t) &= n_0(\mathbf{r}) + \delta n_{3\mathrm{D}}(\mathbf{r},t), \\ \phi(\mathbf{r},t) &= \phi_0(\mathbf{r}) + \delta\phi_{3\mathrm{D}}(\mathbf{r},t); \end{aligned} \tag{2.30}$$

with the density perturbation ($\delta n_{3\mathrm{D}}$) and phase perturbation ($\delta\phi_{3\mathrm{D}}$) related by $\delta n_{3\mathrm{D}} = -(\hbar/g)(\partial_t + \mathbf{v}_s \cdot \boldsymbol{\nabla})\delta\phi_{3\mathrm{D}}$, where $\mathbf{v}_s$ is the velocity of the background condensate flow. From Eq. (2.29) and (2.30), the action can be written, at second order, in terms of the phase perturbation only

$$S = \frac{\hbar^2}{2g}\int \mathrm{d}t\,\mathrm{d}\mathbf{r}\left\{\left[\left(\partial_t + \mathbf{v}_s\cdot\nabla\right)\delta\phi_{3\mathrm{D}}\right]^2 + c^2[\nabla(\delta\phi_{3\mathrm{D}})]^2\right\}. \tag{2.31}$$

Let us consider a toroidally shaped BEC with the confining potential

$$V(\rho,z) = \mu\left[\left(\frac{\rho}{\rho_\mu}\right)^{n_\rho} + \left(\frac{z}{z_\mu}\right)^{n_z}\right] = V_0\left(\rho^{n_\rho} + z^{n_z}\right), \tag{2.32}$$

where μ is the chemical potential, $\rho := r - R(t)$ is the comoving cylindrical coordinate (see Fig. 2.1), n_z and n_ρ are even positive integers, ρ_μ (z_μ) is the condensate Thomas-Fermi width along the ρ (z) trap direction, and $V_0 = \mu/\rho_\mu^{n_\rho} = \mu/z_\mu^{n_z}$ is the trap depth. We can derive an equation for the azimuthal phonon modes assuming that the vertical[8] trapping frequency is higher than the radial trapping frequency and that the ring is thin, $r_\mu \ll R$. In this regime, $\delta\phi_{3\mathrm{D}}(\mathbf{r},t) \to \delta\phi_{1\mathrm{D}}(\theta,t)$ and the action

[8]In this thesis the vertical direction corresponds to the z axis. See Fig. 4.1 and Fig. 4.9 for reference regarding the coordinate system.

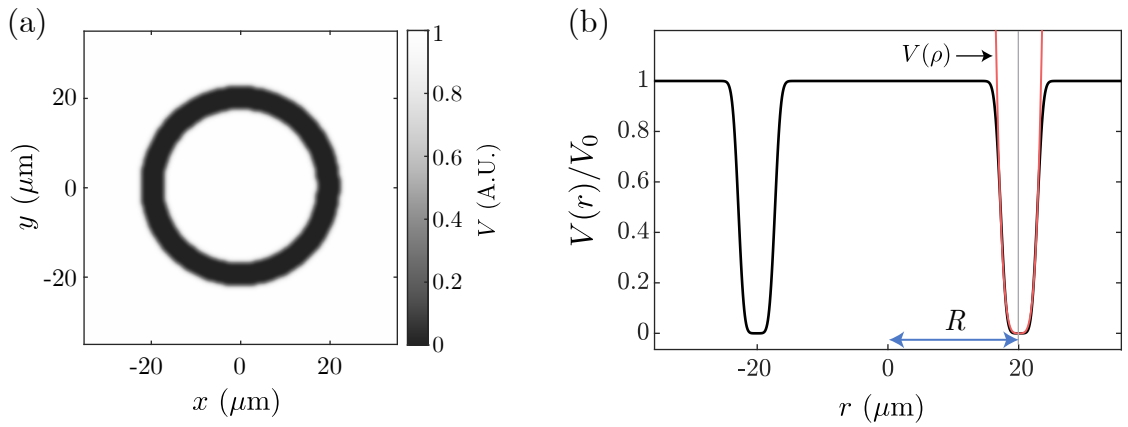

Figure 2.1: Ring potential. (a) Horizontal confinement $V(r)$ for a ring with radius $R = 20\mu$m. (b) Cross section of $V(r)$ which is approximated by the power law potential $V(\rho) = V_0\rho^{n_\rho}$, with $\rho = r - R$; here $n_\rho = 4$.

given by Eq. (2.31) can be integrated along the transverse coordinates ρ and z, yielding

$$\left\{\partial_t^2 + \frac{\dot{\mathcal{V}}(t)}{\mathcal{V}(t)}\partial_t - \left[\frac{c_\theta(t)}{R(t)}\right]^2 \partial_\theta^2\right\}\delta\phi_{1\mathrm{D}} = 0, \tag{2.33}$$

where $\mathcal{V}(t) := \int r\,\mathrm{d}r\,\mathrm{d}\theta\,\mathrm{d}z = 2\pi\int \mathrm{d}z\,\mathrm{d}\rho\,[R(t)+\rho]$ is the time-dependent volume[9] of the condensate and

$$c_\theta^2(t) := \frac{2\pi R(t)}{\mathcal{V}(t)}\int \mathrm{d}z\,\mathrm{d}\rho\,\frac{c^2}{1+\rho/R(t)}, \tag{2.34}$$

is the azimuthal speed of sound. The term $\dot{\mathcal{V}}/\mathcal{V}$ that arises from the changing metric [47] defined by the background condensate is identified as the non-dissipative "Hubble friction".

From the T-F approximation, Eq. (2.16), and Eq. (2.32) we find that the

[9]The integral is performed inside the T-F distribution found through Eq. (2.16) and Eq. (2.32)

chemical potential scales with R as

$$\mu = R^{-\alpha} \left[\frac{gN}{2\pi \mathcal{C}(n_\rho, n_z)} \right]^{\alpha} V_0^{1-\alpha}, \tag{2.35}$$

where $\mathcal{C}(n_\rho, n_z) = 4\Gamma(1+1/n_\rho)\Gamma(1+1/n_z)/\Gamma(1+1/\alpha)$ is a constant and we have introduced the geometric factor

$$\alpha = \frac{1}{1+1/n_\rho+1/n_z}. \tag{2.36}$$

From Eq. (2.35) we can derive the scaling with R of relevant parameters in this model: the effective speed of sound scales as $c_\theta^2 \propto \mu \propto R^{-\alpha}$ and the volume scales as $\mathcal{V} \propto R\rho_\mu z_\mu \propto R^\alpha$, therefore $\dot{\mathcal{V}}/\mathcal{V} = \alpha \dot{R}/R$.

Assuming azimuthal phonon mode solutions $\delta\phi_{1\mathrm{D}}(\theta, t) = \delta\phi(t)\sin(m\theta)$, with $\delta\phi$ the time-dependent phonon amplitude and m the integer phonon mode, we can rewrite Eq. (2.33) as

$$\left\{ \partial_t^2 + \left[2\gamma_m + \alpha \frac{\dot{R}(t)}{R(t)} \right] \partial_t + \omega_m^2(t) \right\} \delta\phi(t) = 0, \tag{2.37}$$

were we have introduced the instantaneous angular frequency $\omega_m = mc_\theta(t)/R(t)$, and γ_m that accounts for phenomenological damping. This phenomenological damping term can account for both Landau and Beliaev damping mechanisms [48], as well as imperfections in the confining potential. We note that the term $\alpha(\dot{R}/R)\partial_t\,\delta\phi(t)$ plays the role of "Hubble friction". Equation (2.37) serves as the model to study Hubble amplification and attenuation of in our experimental setup (Chapter 6).

2.3.2 Phonon evolution in terms of observable parameters

This section derives a set of equations that are suitable to analyze the data obtained from experimental realizations of contraction or expansion of the toroidal BEC. We measure in our experimental setup the density perturbation $\delta n_{2D}(r,\theta,t) = \int \mathrm{d}z\, \delta n_{3\mathrm{D}}(\mathbf{r},t)$, which is related to the phase perturbation according to[10]

$$\delta n_{3\mathrm{D}}(\mathbf{r},t) \quad = -(\hbar/g)\partial_t[\delta\phi_{3\mathrm{D}}(\mathbf{r},t)]. \tag{2.38}$$

Integrating both sides over the transverse directions yields[11]

$$-\frac{\hbar}{2\pi g}\partial_t[\delta\phi_{1\mathrm{D}}(\theta,t)] = \frac{1}{\mathcal{V}}\int \mathrm{d}z\, r\, \mathrm{d}r\, \delta n_{3\mathrm{D}}(\mathbf{r},t), \tag{2.39}$$

$$= \frac{\delta n_{1\mathrm{D}}(\theta,t)}{\mathcal{V}}, \tag{2.40}$$

were $\delta n_{1D}(\theta,t) = \int r\, \mathrm{d}r\, \delta n_{2\mathrm{D}}(r,\theta,t)$. We assume $\delta n_{1\mathrm{D}}(\theta,t) = \delta n(t)\sin(m\theta)$, then

$$\partial_t\left[\delta\phi_{1\mathrm{D}}\right] \propto \frac{\delta n(t)\sin\left(m\,\theta+\varphi_0\right)}{[R(t)]^{\alpha}}. \tag{2.41}$$

[10] This relation is derived from Eq. (2.20), (2.21) and (2.30) assuming, as in Ref. [22], that $\boldsymbol{\nabla}\phi_0$ only has components along $\hat{e}_r$ and $\hat{e}_z$ while $\boldsymbol{\nabla}\delta\phi_{3\mathrm{D}}$ only has a component along $\hat{e}_\theta$.

[11] It is assumed that the rings are thin such that the trap frequencies are much higher than the phonon frequency, $\omega_z, \omega_\rho \gg \omega_m$.

Since we can measure $\delta n(t)$ and $R(t)$ we define a parameter χ that simplifies analyzing experimental data, defined by

$$\frac{\partial}{\partial t}\chi = \frac{\delta n(t)}{[R(t)]^{\alpha}}. \tag{2.42}$$

Using eq. (2.42) we can rewrite eq. (2.37) as

$$\frac{\partial^2}{\partial t^2}\chi + \left[2\gamma_m(t) + \alpha\frac{\dot{R}(t)}{R(t)}\right]\frac{\partial}{\partial t}\chi + \left[\frac{mc_\theta(t)}{R(t)}\right]^2 \chi = 0. \tag{2.43}$$

While Eq. (2.37) is the model derived from first principles to study Hubble amplification and attenuation in a contracting or expanding toroidal BEC, Eq. (2.43) will be used to understand the response of our system and to analyze the experimental results. This will be presented in Chapter 6.

Chapter 3: Laser Cooling and Trapping

This chapter presents an overview of the theory that underlies the experimental techniques used for cooling, trapping, manipulating and probing ultracold neutral atoms. In section 3.1 we look at the basic properties common to alkali atoms. Section 3.2 presents a semi-classical description of interactions between atoms and light, this is the basis of the techniques used for laser cooling and trapping described in sections 3.3 and 3.5, as well as for probing atoms using absorption imaging (section 3.6). The interaction of atoms and magnetic fields together with forced evaporation in magnetic traps, which is essential to produce BECs, is described in section 3.4.

3.1 Alkali Atomic Structure

Alkali atoms present a hydrogen-like electronic structure, that is, they all have one valence electron in the ground state. The energy levels of hydrogen-like atoms can be written in terms of the quantum numbers **S**, the intrinsic spin of the electron, **L**, the orbital angular momentum of the valence electron, and **I**, the nuclear spin. The state of the electron is commonly written in spectroscopic notation as $n^{2S+1}L_J$, where **J** is he total angular momentum of the electron given by $\mathbf{J} = \mathbf{L} + \mathbf{S}$.

The total angular momentum of the electron couples to the nuclear spin caus-

ing an energy shift of the degenerate J states, namely, the hyperfine splitting. Given the total atomic angular momentum, $\mathbf{F} = \mathbf{I} + \mathbf{J}$, we can write the hyperfine shift as

$$\Delta E_{\mathrm{HFS}} = g_N \mu_K B_J \left[\frac{F(F+1) - J(J+1) - I(I+1)}{2\sqrt{J(J+1)}} \right] , \tag{3.1}$$

where g_N is the nuclear g-factor, μ_K is the nuclear magneton and B_J is the internal magnetic field produced by the electron, which in turn depends on the electron angular momentum J.

Given the quantization axis $\hat{z}$, we can fully describe the state of the electron in the basis $|F, m_F\rangle$ where m_F is the projection of the total angular momentum F along the z-axis.

3.1.1 Atomic Structure of Sodium

We use sodium in our experiment. Sodium is an alkali atom with atomic number $Z = 11$, and one stable isotope, ^{23}Na. The electronic structure of which is $1s^2 2s^2 2p^6 3s^1$. The ground state of ^{23}Na has two hyperfine manifolds because of its nuclear spin of $I = 3/2$. The first excited electronic state of sodium is a $3p$ state that, due to spin-orbit coupling, splits into two states $3P_{1/2}$ and $3P_{3/2}$. The transition between the ground state and the $3P_{3/2}$ state is known as the D_2 line and has a wavelength of 589 nm. Figure 3.1 shows the hyperfine levels of the D_2 line, the ground state hyperfine levels are labeled by F while the excited state hyperfine levels are labeled by F'. Cooling and probing happen on the cycling transition ($F = 2 \rightarrow F' = 3$). Due to off-resonant scattering atoms can be excited to $F' = 2$

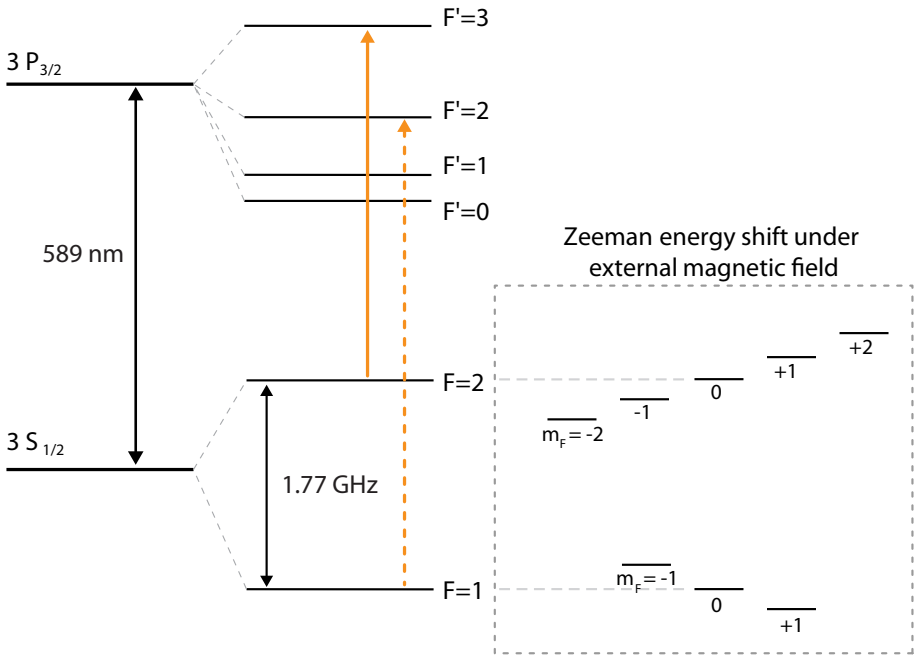

Figure 3.1: Energy level structure of the D_2 line in sodium. Values taken from [1]. The solid yellow line corresponds to the cycling transition used for Doppler cooling. The dashed yellow line corresponds to the repumping transition. Inset shows the Zeeman splitting of the ground state hyperfine manifolds in the presence of an applied external magnetic field.

from which state they can decay either into $F = 1$ or $F = 2$. This off-resonant excitation leads to optical pumping of atoms out of the cycling transition. To prevent this, repumping into the cycling transition is needed applying light resonant with the $F = 1 \rightarrow F' = 2$ transition.

3.2 Atom light interaction

Ultracold atom experiments rely on the interaction between electromagnetic fields and atoms for trapping and cooling. Fine tuning these interactions allow for precise control of the atoms.

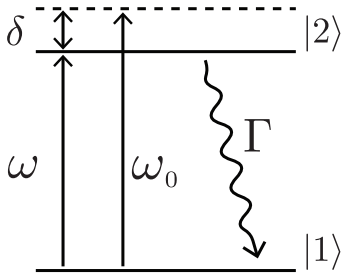

Figure 3.2: Energy diagram of a two level atom. $|1\rangle$ is the ground state and $|2\rangle$ is the excited state. The energy difference between these states is $\hbar\omega = \hbar(\omega_2 - \omega_1)$. The laser field frequency is denoted as ω_0 with $\delta = \omega - \omega_0$ the detuning from the transition. The excited state can spontaneously decay into the ground state with decay rate Γ.

3.2.1 The two level atom

A semiclassical description of the interaction of a laser field and a two level atom suffices to understand the system. This approach regards the laser light as a classical field and the atom as a two level quantum system with dipole coupling between the ground state and the excited state. The description presented here follows a standard treatment that can be found in several textbooks [37, 49, 50, 51, 52].

The Hamiltonian that describes the two level atom in the absence of light is

$$H_0 = \begin{pmatrix} E_1 & 0 \\ 0 & E_2 \end{pmatrix} , \tag{3.2}$$

where E_1 is the energy of the ground state $|1\rangle$, E_2 is the energy of the excited state $|2\rangle$ and $E_2 - E_1 = \hbar(\omega_2 - \omega_1) = \hbar\omega_0$. The generalized solution to the time-dependent

Schrödinger equation for this Hamiltonian is the wavefunction

$$\Psi(\mathbf{r},t) = c_1|1\rangle \mathrm{e}^{-\mathrm{i}\omega_1 t} + c_2|2\rangle \mathrm{e}^{-\mathrm{i}\omega_2 t} \ . \tag{3.3}$$

We begin the description of the atom-light interaction assuming that the laser light is monochromatic and homogeneous. Then, we can write the oscillating electric field as

$$\mathbf{E}(t) = \frac{\hat{\varepsilon} E_0}{2}\left(e^{i\omega t} + e^{-i\omega t}\right) \ . \tag{3.4}$$

Here, E_0 is the amplitude of the field, $\hat{\varepsilon}$ its polarization and ω its frequency. The interaction between the atom and the field in the dipole approximation is described by the Hamiltonian

$$H_I(t) = -\mathbf{d}\cdot\mathbf{E}(t) \ , \tag{3.5}$$

where $\mathbf{d}$ is the electric dipole moment of the atom. Since this Hamiltonian is proportional to $\mathbf{r}$ its matrix representation will only have off-diagonal elements

$$H_I = \begin{pmatrix} 0 & \hbar\Omega \\ \hbar\Omega^* & 0 \end{pmatrix} \cos(\omega t) \ , \tag{3.6}$$

where we have defined the Rabi frequency as

$$\Omega := -\frac{\langle 1|\, \hat{\varepsilon}\cdot\mathbf{d}\, |2\rangle}{\hbar} E_0 \ . \tag{3.7}$$

The full Hamiltonian that describes the atom-light system is then

$$H(t) = \begin{pmatrix} \hbar\omega_1 & \hbar\Omega\cos(\omega t) \\ \hbar\Omega^*\cos(\omega t) & \hbar\omega_2 \end{pmatrix} . \tag{3.8}$$

Using this Hamiltonian and equation 3.3 in the time-dependent Schrödinger equation yields the differential equations

$$\begin{aligned} i\dot{c}_1 &= \tfrac{\Omega}{2}e^{-i\omega_0 t}(e^{i\omega t} + e^{-i\omega t})c_2 \\ i\dot{c}_2 &= \tfrac{\Omega^*}{2}e^{+i\omega_0 t}(e^{i\omega t} + e^{-i\omega t})c_1 \end{aligned} \tag{3.9}$$

The oscillating terms on the RHS of (3.9) oscillate at two different frequencies, $\omega \pm \omega_0$. For near resonant radiation ($\omega_0 \approx \omega$) $\omega + \omega_0 >> |\omega - \omega_0|$. Since the dynamics of the atom are slow compared to the fast oscillating terms we can neglect the terms proportional to $\omega + \omega_0$[1] leading to the equations

$$\begin{aligned} i\dot{c}_1 &= \tfrac{\Omega}{2}e^{i\delta t}c_2 \ , \\ i\dot{c}_2 &= \tfrac{\Omega^*}{2}e^{-i\delta t}c_1 \ , \end{aligned} \tag{3.10}$$

with $\delta := \omega - \omega_0$ the laser detuning from resonance. Going into the rotating frame given by the transformation

$$\begin{aligned} i\tilde{c}_1 &= c_1 e^{-i\delta t/2} \ , \\ i\tilde{c}_2 &= c_2 e^{+i\delta t/2} \ , \end{aligned} \tag{3.11}$$

[1] This is known as the Rotating Wave Approximation (RWA).

we can rewrite the equations (3.10) as

$$\begin{aligned} \dot{\tilde{c}}_1 &= \tfrac{1}{2}(\delta\tilde{c}_1 + \Omega\tilde{c}_2) \ , \\ \dot{\tilde{c}}_2 &= \tfrac{1}{2}(\Omega^*\tilde{c}_1 + \delta\tilde{c}_2) \ , \end{aligned} \tag{3.12}$$

So far the equations derived here consider the coherent evolution of the atom interacting with a monochromatic nearly-resonant classical field. However, to fully understand the evolution of this system one must take into account the spontaneous decay from the excited state. In order to include decay it is easier to work with the density matrix $\rho = |\Psi\rangle\langle\Psi|$,

$$\rho = \begin{pmatrix} c_1c_1^* & c_1c_2^* \\ c_2c_1^* & c_2c_2^* \end{pmatrix} = \begin{pmatrix} \rho_{11} & \rho_{12} \\ \rho_{12}^* & \rho_{22} \end{pmatrix} \ . \tag{3.13}$$

Using equations (3.11) and (3.12), we find that $\tilde{\rho}_{ii} = \rho_{ii}$ and $\tilde{\rho}_{12} = \tilde{\rho}_{21}^* = \rho_{12}\exp(-i\delta t)$. Then, we can write the time derivative of the population in the excited state as[2]

$$\dot{\rho}_{22} = -\frac{i\Omega}{2}(\tilde{\rho}_{12} - \tilde{\rho}_{21}) \ . \tag{3.14}$$

We now include a term to account for decay, rewriting equation (3.14) in the form

$$\dot{\rho}_{22} = -\frac{i\Omega}{2}(\tilde{\rho}_{12} - \tilde{\rho}_{21}) - \Gamma\rho_{22} \ . \tag{3.15}$$

Following a similar procedure for all the ρ_{ij} terms leads to the Optical Bloch Equa-

[2]Here we assume that $\Omega^* = \Omega$.

tions (OBE):

$$\begin{aligned}
\dot{\rho_{11}} &= +\tfrac{i\Omega}{2}(\tilde{\rho}_{12} - \tilde{\rho}_{21}) + \Gamma\rho_{22} \ , \\
\dot{\rho}_{22} &= -\tfrac{i\Omega}{2}(\tilde{\rho}_{12} - \tilde{\rho}_{21}) - \Gamma\rho_{22} \ , \\
\dot{\rho}_{12} &= -(\gamma_\perp + i\delta)\tilde{\rho}_{12} - \tfrac{i\Omega}{2}(\rho_{11} - \rho_{22}) \ .
\end{aligned} \tag{3.16}$$

Here, $\gamma_\perp = (\Gamma/2) + \gamma_c$, with γ_c a term that accounts for dephasing effects that do not affect the populations ρ_{ii}, like atom-atom collisions.

Two key results that arise from solving the OBE are:

- For a strong field, $\Omega \to \infty$, the populations become equal, $\rho_{ii} \to 1/2$.
- The steady-state excited state population is given by

$$\rho_{22} = \frac{1}{2}\frac{\Omega^2/2}{\delta^2 + \Omega^2/2 + \Gamma^2/4} \ . \tag{3.17}$$

3.2.2 Scattering Rate and Power Broadening

The excitation rate and the decay rate are equal in steady state; thus, the total spontaneous decay rate of light from the laser field is given by

$$R_{sc} = \Gamma\rho_{22} = \left(\frac{\Gamma}{2}\right)\frac{\Omega^2/2}{\delta^2 + \Omega^2/2 + \Gamma^2/4} \ . \tag{3.18}$$

However, in the laboratory it is more convenient to think in terms of laser intensity (I) rather than Rabi frequency. Using the relation

$$S := \frac{I}{I_{\text{sat}}} = \frac{2|\Omega|^2}{\Gamma^2} \ , \tag{3.19}$$

where S is the saturation parameter and $I_{\text{sat}} := \pi hc\Gamma/(3\lambda^3)$ is the saturation intensity, we can rewrite equation (3.18) as:

$$R_{sc} = \left(\frac{\Gamma}{2}\right) \frac{I/I_{\text{sat}}}{1 + (I/I_{\text{sat}}) + (4\delta^2/\Gamma^2)} \ , \tag{3.20}$$

$$= \left(\frac{S}{1+S}\right) \frac{\Gamma/2}{1 + (2\delta/\Gamma')^2} \ . \tag{3.21}$$

Here, $(\Gamma')^2 = (1+S)\Gamma^2$. For $S = 1$ we find from (3.21) that the maximum scattering rate is $\Gamma/4$. In the limit $S \to \infty$ the scattering rate saturates at $\Gamma/2$. The effect of increasing the intensity of the laser field beyond I_{sat} can be seen as a broadening of the natural linewidth of the transition. This effect is known as power broadening.

3.2.3 AC Stark Shift

We can rewrite equations (3.12) in matrix form

$$i\partial_t \begin{pmatrix} \tilde{c}_1 \\ \\ \tilde{c}_2 \end{pmatrix} = \begin{pmatrix} \delta/2 & \Omega/2 \\ \\ \Omega/2 & -\delta/2 \end{pmatrix} \begin{pmatrix} \tilde{c}_1 \\ \\ \tilde{c}_2 \end{pmatrix}. \tag{3.22}$$

Using the ansatz

$$\begin{pmatrix} \tilde{c}_1 \\ \\ \tilde{c}_2 \end{pmatrix} = \begin{pmatrix} a \\ \\ b \end{pmatrix} e^{-i\lambda t} \tag{3.23}$$

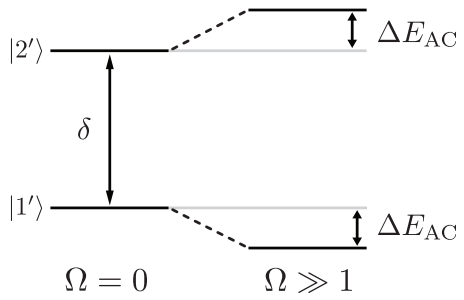

Figure 3.3: AC Stark shift. Diagram depicting the perturbed states and the corresponding energy shifts.

and solving for the eigenvalues λ yields $\lambda = \pm\sqrt{\delta^2 + \Omega^2}/2$. When $\Omega = 0$, the splitting of the unperturbed dressed-states is $\omega_2' - \omega_1' = \delta$. When $|\delta| >> \Omega$,

$$\lambda \approx \pm\left(\frac{\delta}{2} + \frac{\Omega^2}{4\delta}\right). \tag{3.24}$$

Thus, the energy of the perturbed states is shifted with respect to the energy of the unperturbed states by $\Delta E_{\mathrm{AC}} = \hbar\omega_{\mathrm{AC}}$ with

$$\omega_{\mathrm{AC}} = \frac{\Omega^2}{4\delta}. \tag{3.25}$$

3.2.4 Light Force on Atoms

The interaction of an atom with light has not only the effect of changing the internal state of the atom but it also has a mechanical effect. When light interacts with an atom it exerts forces on the atom that can be generalized into two types[3]:

- *Radiation pressure force* due to absorption and re-scattering of light.

[3]It is worth noting that this separation is historical; both forces are just one interaction. In the case of radiation-pressure force spontaneous emission dominates; meanwhile, the dipole force is the limit when stimulated emission dominates.

- *Dipole force* due to the potential energy of the atom in the laser electric field.

Radiation Pressure Force. The treatment of light so far has been from a classical perspective. However, in order to understand how light exerts a radiation pressure force on the atom it is convenient to briefly treat light as photons.

When an atom absorbs a photon that carries momentum $\hbar\mathbf{k}$, the momentum of the atom is changed by $m\Delta\mathbf{v} = \hbar\mathbf{k}$. The rate at which an atom can scatter photons is given by equation (3.20). The force that photons exert on the atom can be written as

$$F_{sc} = (\hbar k)R_{sc} = (\hbar k)\left(\frac{\Gamma}{2}\right)\frac{I/I_{\text{sat}}}{1 + (I/I_{\text{sat}}) + (4\delta^2/\Gamma^2)} \,. \tag{3.26}$$

The atoms can emit photons either coherently (stimulated emission) or incoherently (spontaneous emission). While stimulated emission is a reversible process, spontaneous emission cannot be reversed. As a consequence, spontaneous emission is the only emission that results in the dissipative scattering force.

Dipole Force. Let us consider laser light with $|\delta| >> \Gamma$ and $|\delta| >> \Omega$. In this regime the dipole force can be derived from the potential that an atom experiences due to the AC Stark shift

$$V_{\text{dipole}} = \hbar\omega_{AC} \,. \tag{3.27}$$

From equations (3.19) and (3.25), we can rewrite (3.27) as

$$V_{\text{dipole}} \approx \frac{\hbar\Omega^2}{4\delta} = \frac{\hbar\Gamma}{8}\frac{\Gamma}{\delta}\frac{I}{I_{\text{sat}}} \,. \tag{3.28}$$

Then,

$$\mathbf{F}_{\text{dipole}} = -\boldsymbol{\nabla} V_{dipole} \ ,$$

$$\approx -\frac{\hbar\Gamma}{8}\frac{\Gamma}{\delta}\frac{\boldsymbol{\nabla} I}{I_{\text{sat}}} \ . \tag{3.29}$$

We can see from equation (3.28) that

- If $\delta < 0$ (*red-detuned* laser) $\rightarrow V_d \propto -I$. The potential has a minimum where the intensity is highest. In this case the atoms will be attracted to the intensity maximum.

- If $\delta > 0$ (*blue-detuned* laser) $\rightarrow V_d \propto I$. The potential has a maximum where the intensity is highest. In this case the atoms will be repelled from regions of intensity maxima.

This result becomes the fundamental tool that enables tailoring arbitrary potentials for trapping atoms using light.

3.3 Laser Cooling and Trapping

3.3.1 Optical Molasses

To reduce the temperature of an atomic cloud the velocity of the atoms must be reduced in three dimensions, this can be achieved with three pairs of counter-propagating beams. To understand how this works consider the one dimensional case of an atom moving with speed $\mathbf{v}$ along the propagation axis of two counter-

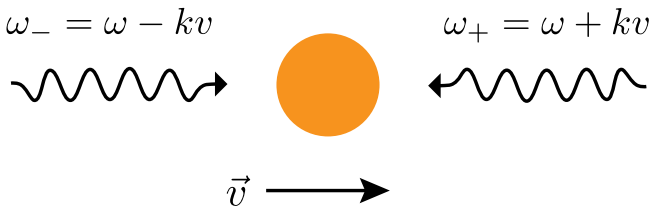

Figure 3.4: Doppler shift. An atom travels along the propagation axis of two counter-propagating beams. In the rest frame of the atom the frequency of each beam is shifted by $-\mathbf{k}\cdot\mathbf{v}$. Here ω is the laser frequency in the laboratory frame, $\mathbf{k}$ is the light wave vector and $\mathbf{v}$ is the velocity of the atom in the laboratory frame.

propagating beams with wave vector $\mathbf{k}$, see Fig. 3.4, in the rest frame of the atom the beams have different frequencies

$$\omega_\pm = \omega \pm kv, \tag{3.30}$$

with ω the frequency of the light in the laboratory frame and $kv = |\mathbf{k}\cdot\mathbf{v}|$. If the frequency of the beams is chosen to be red-detuned, the Doppler shift enhances scattering off of the counter-propagating beam which has the effect of slowing down the atom. This follows from the force that each of the beams exerts on the atom which can be found from (3.26) to be

$$\mathbf{F}_\pm = \pm\frac{\hbar\mathbf{k}\Gamma}{2}\frac{S}{1+S+\left[2\left(\delta\mp|\omega_D|\right)/\Gamma\right]^2}\ . \tag{3.31}$$

For $|\omega_D| \ll \delta$, the denominator can be expanded in powers of $(kv/\Gamma)^2$, the resulting expression is[4]

$$\mathbf{F}_{\rm OM} \cong \frac{8\hbar k^2\delta S\mathbf{v}}{\Gamma\left(1+S+(2\delta/\Gamma)^2\right)^2} \equiv -\alpha\mathbf{v}\ . \tag{3.32}$$

[4]Terms $\mathcal{O}((kv/\Gamma)^4)$ and higher are ignored.

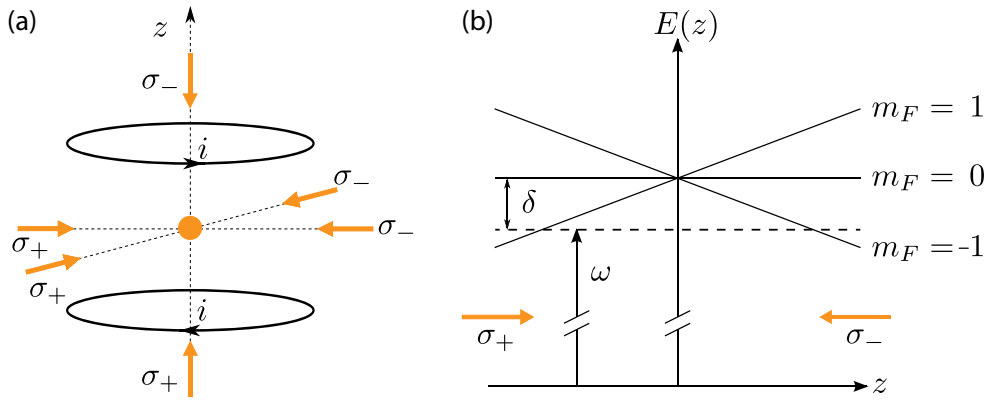

Figure 3.5: Magneto Optical Trap (MOT). (A) Schematic of a 3D-MOT setup consisting of three orthogonal pairs of counter-propagating beams and a pair of coils in quadrupole configuration producing a linear magnetic field at the center of the trap. (B) Energy diagram of the excited state with F=1.

This equation has the form of a frictional force with damping coefficient α and is why this effective force is typically referred to as Optical Molasses.

Although the atoms cooled down by the technique of Optical Molasses are effectively trapped at the center of the counter-propagating beams, since diffusion out of the region of overlap is slow (typ. $\sim$ 5 s), this configuration is not a robust trap. However, making a few modifications to the Optical Molasses scheme gives rise to the so called Magneto Optical Trap (MOT) which is a much more robust trap.

3.3.2 Magneto-Optical Trap

The experimental configuration of a MOT in three dimensions is depicted in figure 3.5. In addition to the three counter propagating beams used for Optical Molasses, an external magnetic gradient is provided by a pair of coils in quadrupole configurations. The magnetic gradient causes a position dependent Zeeman split-

ting. This leads to an imbalance between the scattering forces from each of the beams that results in a position dependent force.

Although the principle of a MOT will be explained in terms of a system where the ground state has $F_g = 0$ and the excited state has $F_e = 1$, this mechanism can be generalized to atoms for which there is a transition $F_g \to F_e = F_g + 1$. By means of optical pumping, for example by the σ_+ beam, the atoms will end up in the stretched state $m_g = +F_g$ which forms a closed system with $m_e = +F_e$.

The force on an atom in the simple one-dimensional case is

$$\mathbf{F}_\pm = \pm \frac{\hbar \mathbf{k} \Gamma}{2} \frac{S}{1 + S + \left[2\left(\delta_\pm\right)/\Gamma\right]^2} \ , \tag{3.33}$$

where the detuning is given by

$$\delta_\pm = \delta \pm \omega_D \pm \omega_Z \ . \tag{3.34}$$

Here, $\omega_D = -\mathbf{k} \cdot \mathbf{v}$ is again the Doppler shift and $\omega_Z := \mu' B/\hbar$ is the Zeeman shift with an effective magnetic moment $\mu' := (g_2 m_2 - g_1 m_1)\,\mu_B$. For $\omega_D \ll \delta$ and $\omega_Z \ll \delta$ the expression can be approximated as was done with (3.32), yielding

$$\mathbf{F}_{\mathrm{MOT}} = -\alpha \mathbf{v} - \beta \mathbf{r} \ , \tag{3.35}$$

where α is defined in (3.32) and $\beta := (\mu' B'/\hbar k)\alpha$, with B' the magnetic field gradient.

The minimum expected temperature for a gas of two-level atoms is set by the

balance of the Doppler cooling forces and the recoil forces experienced by the atoms, this limit known as the Doppler limit is given by

$$T_{\mathrm{D}} = \frac{\hbar\Gamma}{2k_{\mathrm{B}}} \tag{3.36}$$

with k_{B} Boltzmann's constant. For sodium $T_{\mathrm{D}} = 235\mu\mathrm{K}$ [1].

3.4 Magnetic Trapping and Evaporative Cooling

Atoms placed in an external magnetic field B experience an energy shift given by

$$H_B = \frac{\mu_B}{\hbar}\left(g_s S_z + g_L L_z + g_I I_z\right) B_z, \tag{3.37}$$

where S_z, L_z and I_z are the z-component of the angular momentum operators $\mathbf{S}$, $\mathbf{L}$ and $\mathbf{I}$, and g_i the corresponding Landè g-factors.

When the energy shift due to the external magnetic field is small compared to the hyperfine splitting, the Hamiltonian from equation (3.37) can be treated as a perturbation of the atomic Hamiltonian. Thus, we can still work in the basis $|n, L, J, F, m_F\rangle$ to describe the state of the atom (F,m_F remain good quantum numbers). In this regime

$$H_B = \mu_B\, g_F\, m_F\, B_z \ , \tag{3.38}$$

with g_F the corresponding Landè g-factor. The resulting Zeeman energy shift is given by

$$U_B(\mathbf{r}) = -\boldsymbol{\mu}_F \cdot \mathbf{B}(\mathbf{r}) = \mu_B\, g_F\, m_F\, B_z \ , \tag{3.39}$$

and the resulting force exerted on an atom can be written as

$$F_B(\mathbf{r}) = -\nabla U_B(\mathbf{r}) = -\mu_B \, g_F \, m_F \, \nabla B_z \ . \tag{3.40}$$

Since (for static fields) there cannot be a magnetic field local maximum, the only way for equation (3.39) to have a local minimum is if $g_F \, m_F > 0$. States for which this is true are called low-field seeking and only those states are magnetically trappable using static magnetic fields. In the case of sodium there are three low-field seeking states: $|1, -1\rangle$,$|2, 1\rangle$ and $|2, +2\rangle$.

3.4.1 Evaporative Cooling

The basic principle behind evaporative cooling is to remove the most energetic atoms form the trap and to allow the remaining atoms to re-thermalize to a lower temperature. This process usually takes place while atoms are trapped in a a magnetic trap. In order to remove atoms from said trap, a radio frequency (RF) field is applied to flip the spin of the more energetic atoms. Once an atom undergoes this transition, the atom is no longer trappable by the magnetic potential.

The energy of the atoms in the magnetic trap is given by

$$E = \frac{1}{2} m v^2 + \mu \, |B(\mathbf{r})| \ . \tag{3.41}$$

Since the magnitude of the magnetic field is position dependent, the atoms interact

with the RF field where

$$\hbar\omega_{RF} = \mu \left|B(\mathbf{r})\right| \ . \tag{3.42}$$

Atoms with energy higher than this will be removed from the trap. The truncation potential energy is given by

$$\varepsilon_t = \hbar(\omega_{RF} - \omega_0), \tag{3.43}$$

with $\omega_0 = \mu \left|B(0)\right| / \hbar$. The truncation parameter is defined as

$$\eta_t = \frac{\varepsilon_t}{k_B T}, \tag{3.44}$$

where $k_B T$ is the average energy of the atoms in the trap (given their average temperature T).

In order to efficiently cool the atoms the ratio of elastic to inelastic collisions must be large. Elastic collisions lead to re-thermalization while inelastic collisions lead to atom loss. During evaporation the dominant loss process is collisions with the background gas. This is why having good vacuum (at least a few 10^{-10} Torr) is essential for ultra-cold atom experiments. In our system (full details will be presented in chapter 5) the evaporation sequence lasts approximately 10 s while the lifetime in the hybrid trap where the final stage of evaporation takes place is approximately 25 s.

3.4.2 Majorana Losses

When placed in a magnetic field, B, the atom's magnetic dipole moment precesses about the local external field at the Larmor frequency $\omega_L = \frac{\mu_B B}{\hbar}$. Magnetic trapping works as long as the atom moves adiabatically in the trap, this implies slow variations in the local magnetic field direction compared to the Larmor frequency. The condition for adiabaticity can be written as [50]

$$\omega_L \gg \frac{1}{B}\left|\frac{\mathrm{d}B}{\mathrm{d}t}\right| \ . \tag{3.45}$$

When this criterion is satisfied, the orientation of the atom's magnetic moment can follow the direction of the field. If equation (3.45) is violated the atom may transition into a state with opposite m_F value, this phenomena is known as a Majorana spin-flip [53]. Once the atom transitions from the state $|F, m_F\rangle$ to $|F, -m_F\rangle$ it is no longer magnetically trappable; thus, it is ejected from the trap.

Typically, atoms that have been optically cooled and transferred to a magnetic trap are energetic enough to spend most of the time in orbits for which adiabaticity is satisfied. However, as atoms are further cooled down via RF evaporation, they spend more time near the zero field point of the trap where equation (3.45) no longer holds. There are a number of common techniques used to prevent atoms from escaping the trap due to Majorana losses, e.g., Time Orbiting Potentials [26, 54] that keep the atoms away from the zero-field point. Alternatively, one can take advantage of this loss process to load the coldest atoms into a red detuned dipole trap [55]. We

implement the latter method in our laboratory to reach degeneracy.

3.5 Red Detuned Dipole Trap

A tightly focused Gaussian beam far detuned to the red from resonance produces an attractive dipole trap. The intensity of the beam, in cylindrical coordinates, is given by

$$I(\rho, z) = \frac{P}{\pi w(z)^2} \exp\left[-\frac{2\rho^2}{w(z)^2}\right], \tag{3.46}$$

where P is the power of the laser beam and

$$w(z) = w_0\sqrt{1 + (z/z_R)^2}. \tag{3.47}$$

Here w_0 is the beam waist and $z_R = \pi w_0^2/\lambda$ is its Rayleigh length. The potential can be found from equation (3.28). In the case of atoms with energy $k_B T \ll U_0$, where U_0 is the trap depth, the potential can be Taylor expanded and approximated as a harmonic trap

$$U(\rho, z) = -U_0\left[1 - 2\left(\frac{\rho}{\omega_0}\right)^2 - \left(\frac{z}{z_R}\right)^2\right]. \tag{3.48}$$

This harmonic trap has characteristic frequencies

$$\begin{aligned} \omega_\rho &= \sqrt{4U_0/m\omega_0^2}\,, \\ \omega_z &= \sqrt{2U_0/mz_R^2}\,. \end{aligned} \tag{3.49}$$

In most applications $\omega_\rho \gg \omega_z$ which makes necessary the addition of extra confinement along the weak trapping axis (z in this case).

3.6 Resonant Absorption Imaging

The general idea of absorption imaging is to record on a CCD camera the shadow that the atoms cast as a near-resonant probe beam traverses the cloud. The probe beam is attenuated due to light being scattered by the atoms. The attenuation of a near-resonant probe beam is given by [56]

$$\frac{dI}{dz} = -n\sigma I \ , \tag{3.50}$$

where n is the atomic cloud density, and σ is the absorption cross section,

$$\sigma = \frac{\sigma_0}{1 + 4(\delta/\Gamma)^2 + (I/I_{\rm sat})} \ . \tag{3.51}$$

Here, σ_0 is the on-resonance cross section, δ is the detuning, and Γ the transition linewidth.

The solution to equation (3.50), accounting on first order in $(I/I_{\rm sat})$ for saturation effects, is

$$\tilde{n}(x,y)\sigma_0 = -\ln\frac{I_{\rm a} - I_{\rm b}}{I_{\rm p} - I_{\rm b}} + \frac{I_{\rm p} - I_{\rm a}}{I_{\rm sat}} \ , \tag{3.52}$$

where $\tilde{n}(x,y)$ is the column density—the density of the cloud integrated along the propagation of the probe beam—, $I_{\rm a}$ is the intensity of the probe in the presence of atoms scattering light, $I_{\rm p}$ is the intensity of the probe in the absence of atoms, and

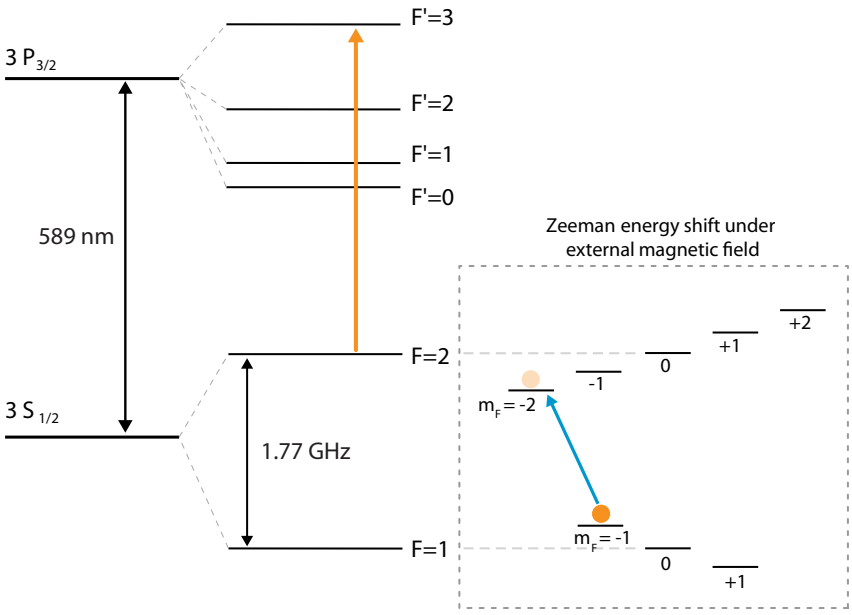

Figure 3.6: PTAI scheme in ^{23}Na. The initial population is in the ground state $|1,-1\rangle$, a short microwave pulse (blue arrow) transfers a small fraction of the population to the stretched state $|2,-2\rangle$. We image the population in the latter state by applying a short pulse of probe light on-resonance with the cycling transition (yellow line).

I_{b} is the intensity of the background when no probe light is shone. Equation (3.52) is known as the Beer-Lambert law and the term $\tilde{n}(x,y)\sigma_0$ is refer to as the optical density (OD) of the cloud.

3.6.1 Partial-Transfer Absorption Imaging (PTAI)

Although absorption imaging with probe powers below I_{sat} works well when imaging thermal clouds, once the atoms reach condensation, typical ODs are greater than 5. At this point it is difficult to detect subtle atom density variations with high fidelity.

From equation (3.51) we see that the tunable parameters in absorption imaging are the detuning and the intensity of the probe beam. A work around for high

ODs when imaging dense clouds is implementing off-resonant imaging or high probe intensity imaging. However, reconstructing the density distribution from such images is complicated and not always accurate [30, 57]. We have taken a more straight forward approach which involves transferring a fraction of the population into a state that is resonant with the probe light while the rest of the atoms remain in the dark (see figure 3.6). This technique is known as Partial-Transfer Absorption Imaging (PTAI) [58]. Another advantage of this technique is that it is (relatively) non-destructive; it allows us to take multiple images of the same cloud since the atoms that remain in the dark are undisturbed by the probe beam [59].

Chapter 4: Experimental Apparatus

The sodium rings experiment in the JQI at UMD is the second generation of this experiment in the Campbell group. We designed and built an upgraded version of the original apparatus that was formerly at NIST Gaithersburg [60, 61]. The vacuum chamber is described in section 4.1 and the design is completely different from the design of the chamber used in previous generations. Section 4.2 describes the optical layouts of the laser systems used for production of the BEC. The optics used for imaging the atoms and to project arbitrary potentials using a DMD are described in sections 4.3 and 4.4, respectively.

4.1 Vacuum Chamber

Production of ultra-cold atomic clouds can only be achieved in chambers at ultra-high-vacuum (UHV) pressures, i.e., below 10^{-7} mbar. The quality of the vacuum system limits the lifetime of the atomic cloud since collisions with the background gas can exchange energy with the cold atoms and kick them out of their shallow traps [30]. Figures 4.1 and 4.2 show front and top views of our vacuum system, respectively, which is divided into two main chambers—the production chamber and the science chamber—. The chambers are connected via a differential pumping

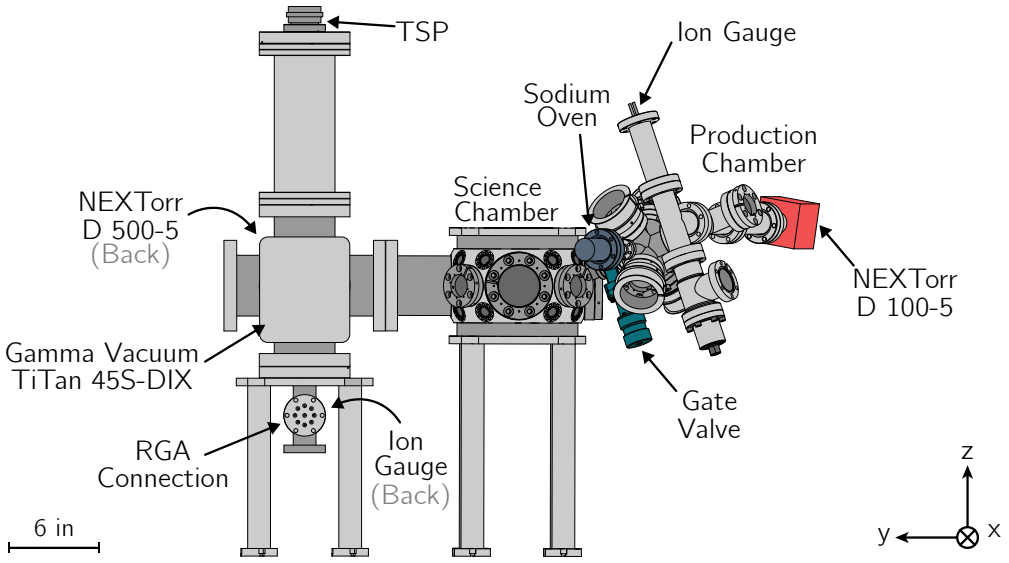

Figure 4.1: Vacuum Chamber (front view).

tube and a gate valve to maintain UHV on the science chamber. The ion gauges read 4×10^{-9} mbar in the production chamber and 4×10^{-10} mbar in the science chamber.

The production chamber, right section of figures 4.1 and 4.2, follows the design of [62]. This chamber contains the sodium oven which consists of a reservoir—a capped 2.75" half-nipple containing ≈ 5 mg of metallic sodium—, and a nozzle—a copper pinch off adapter gasket for 2.75" flange[1]. Both the reservoir and the nozzle are heated by out-of-vacuum clamp heaters and the whole assembly is insulated using a ceramic insulation blanket. Each heater is independently controlled by a proportional integral derivative (PID) temperature controller (Omega CNi16D44-EIT) that actuates a solid state relay (Omega SSRL240DC25). The reservoir's operation temperature is 215°C and the nozzle's is 265°C; both are kept at room temperature during downtime. We control the oven's PIDs via ethernet to automate turning on

[1]Unless stated otherwise, all flanges are CF conflats.

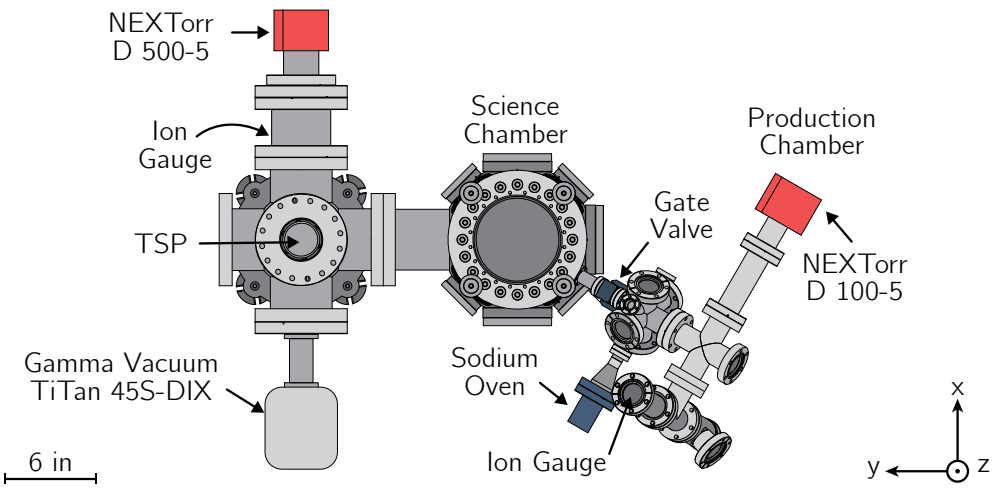

Figure 4.2: Vacuum Chamber (top view).

and off the oven using LabVIEW[2]. The only pumping element on the production chamber is a non-evaporative getter (NEG) ion combination pump (SAES NEXTorr D 100-5); we measure the pressure using an ion gauge (Agilent UHV-24P).

Atoms exiting the nozzle are trapped and cooled using a 2D MOT. The magnetic field required for trapping in the 2D MOT is produced by permanent neodymium magnets, as described in reference [62] (see also [63]). The magnets produce a quadrupole magnetic field that is used for magneto-optical trapping and a gradient that is used to slow down hot atoms out of the oven in similar fashion to a Zeeman slower (see Fig. 4.8). Additionally, there are two pairs of coils in Helmholtz configuration to shim the magnetic fields in the production chamber.

The production chamber is connected to the main body of the science chamber, central section of figures 4.1 and 4.2, via a differential pumping tube and a gate valve (MDC UHV Gate Valve 302000). The gate valve is connected to an interlock that

[2]The temperature of the oven is ramped on or off at a rate of $\approx 2°$C/min to minimize thermal stress and to avoid overshooting during ramp-up.

shuts if the pressure read by the ion gauges on either side exceeds a given threshold. The main body of the science chamber is from Kimball Physics (8 in "spherical square", MCF800-SphSq-G2E4C4A16). The top and bottom viewports are custom order recessed CF flanges with 2.75 in diameter windows to increase optical access for imaging, more details can be found in Appendix A (see also figure A.1).

The pumping elements in the science chamber are located on the left section of figures 4.1 and 4.2. The chamber was originally designed with only one active pump, a NEG ion combination pump (SAES NEXTorr D 500-5) and a passive titanium sublimation pump (TSP) from Agilent Technologies (916-0050). We found that additional pumping capacity was needed to bring the pressure down to the UHV regime[3], thus we installed a 35 L/s ion pump (Gamma Vacuum TiTan 45S-DIX). In addition to the vacuum pumps, the left section of the chamber hosts an ion gauge (Agilent UHV-24P) to monitor the pressure and a residual gas analyzer (SRS RGA200) which was mainly used during initial pump-down.

There are three sets of magnetic coils and their mounts located around the experiment chamber, in addition to the elements depicted on figures 4.1 and 4.2. These sets are:

- **Shimming coils.** Two pairs of coils in Helmholtz configuration to shim the fields in the x and y axis.

- **Quadrupole coils.** Two pairs of coils[4] in the receded vertical viewports to

[3]We found that firing the TSP only helps during the initial pump-down of the chamber, right after bake-out, decreasing the vacuum pressure by a factor of about two. Subsequent activations of the TSP did not have a significant effect in decreasing the pressure.

[4]The pairs of coils are wound around each other, which is why we typically refer to them as inner-quadrupole-coils and outer-quadrupole-coils

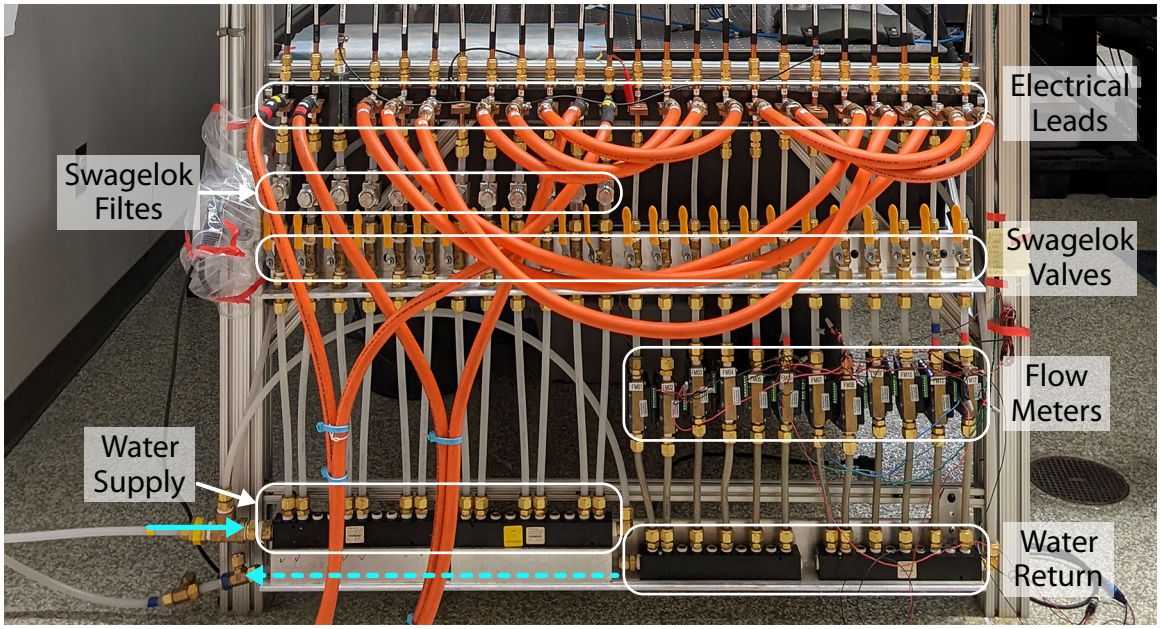

Figure 4.3: Electrical Connections and Water Manifold. Picture showing the elements that form part of the electrical connections to the magnetic coils as well as the water manifold that runs chilled water through the coils.

provide a quadrupole field for magnetic trapping.

- **Conical coils.** A pair of coils on the top and bottom of the chamber.Currently they are used as the additional z axis shimming coils.

While the Shimming coils are designed to run a couple of amperes through them, the quadrupole coils and conical coils are designed to operate at high currents on the order of 200 A. The high currents will heat the coils substantially, therefore the coils are constructed of hollow copper tubing which allows us to run chilled water through them to keep them at room temperature. The water cooling and current delivery assembly is depicted in figure 4.3. On the input, two manifold blocks distribute water coming from the chiller (NESLAB ThermoFlex 5000) to the 12 coil lines, each of them has an in line Swagelok filter on the input and independent Swagelok valves on the input and output to facilitate servicing the line. On the

return, each line has a flow meter (Proteus 800 - 0804BN03) to monitor water flow, the 12 lines merge back at two manifold blocks and the output is sent back to the chiller reservoir.

4.2 Laser Systems

An essential tool in an ultracold atom experiment is the laser systems used to cool, trap and manipulate the atoms. Alkaline atoms can be trapped and cooled down to the Doppler regime with the use of a single wavelength. The transition we use for magneto-optical trapping and cooling in sodium ($3S_{1/2} \rightarrow 3P_{3/2}$) corresponds to a wavelength of 589 nm, we use two laser systems to deliver $P \approx 1.5$ W for cooling, trapping and imaging (described in section 4.2.1). In addition to these systems, we work with two high-power lasers (wavelenghts 532 nm and 1064 nm) to generate optical dipole traps (ODTs). The 1064 nm ODT is used during evaporation to produce a BEC and the 532 nm ODTs are used to project arbitrary potentials onto the atoms. The ODT laser systems are described in section 4.2.2.

4.2.1 589 nm Laser Systems

One of the biggest constraints in a cold atom experiment is laser power, paradoxically, the more power available the more is used without it being seemingly enough[5]. In our case, this situation led to the use of two separate 589 nm laser systems, one to produce light for cooling and one for repumping. The first system generates all the beams with frequencies within 200 MHz of the cycling transition,

[5]One tends to optimize the system to operate with the maximum amount of resources available.

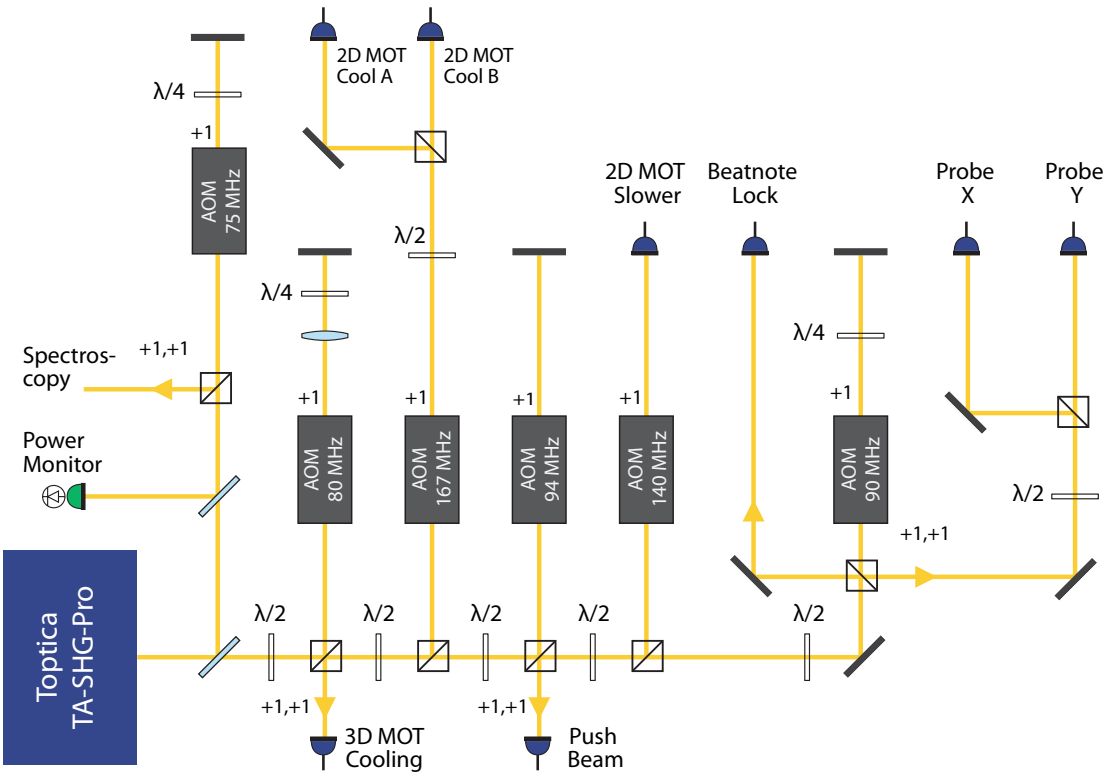

Figure 4.4: Cooling light laser setup (589 nm). The laser frequency is stabilized using Doppler-free absorption spectroscopy. The AOM elements indicate the frequency used to drive them. In each case the order used is indicated next to the AOM, for example, "+1". The text "+1,+1" indicates that the beam comes from a double-pass AOM where the +1 diffraction order is selected in each pass. In front of each fiber there is a coupling lens and a shutter (not shown).

$|g, \mathrm{F} = 2\rangle \rightarrow \left|e, \mathrm{F}' = 3\right\rangle$, where g is the ground state $3S_{1/2}$ and e is the excited state $3P_{3/2}$ (see figure 3.1). The second system generates all the beams with frequencies within 200 MHz of the repumping transition, $|g, \mathrm{F} = 1\rangle \rightarrow \left|e, \mathrm{F}' = 2\right\rangle$.

Figure 4.4 shows the layout of the cooling light setup. We use a commercial laser, Toptica TA-SHG-Pro system (DL-RFA-SHG pro), to produce 1.2 W of light with wavelength 589 nm. This system consists of a diode laser that emits light in the infra-red ($\lambda = 1178$ nm), the light frequency is doubled in a second harmonic generation cavity to produce light in the visible ($\lambda = 589$ nm). This model includes

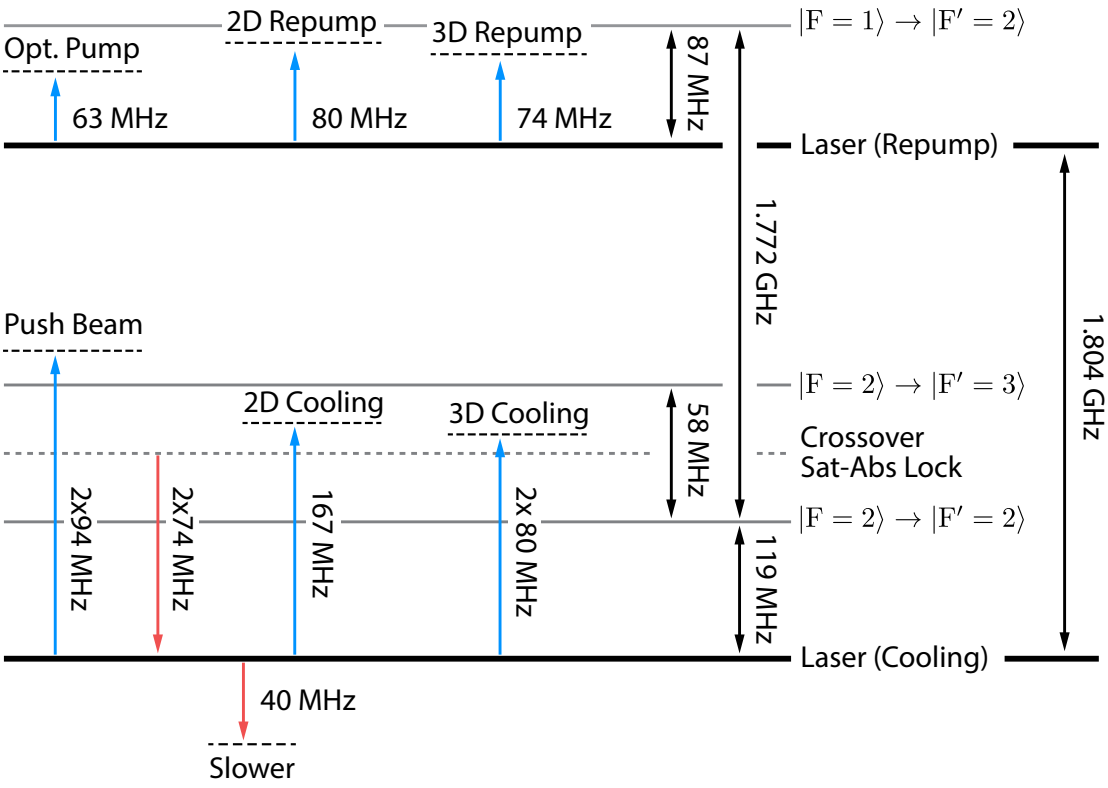

Figure 4.5: Detunings (589 nm). This schematic shows the detunings of all 589 nm light used in our setup. In this representartion the lines stack vertically according to increasing frequency (not to scale). The thick horizontal black lines indicate the frequency of the main laser systems. The grey horizontal lines indicate the resonant frequency of relevant transitions in the D_2 sodium line. Vertical arrows indicate the frequency offsets—red (blue) arrows correspond to red (blue) shifted frequencies—.

a Raman Fiber Amplifier that outputs 1.2 W at 589 nm.

The frequency of the cooling laser system is stabilized using Doppler-free saturated absorption spectroscopy [64]. We lock the laser to the crossover between the transitions $|g, \mathrm{F} = 2\rangle \rightarrow \left|e, \mathrm{F}' = 3\right\rangle$ and $|g, \mathrm{F} = 2\rangle \rightarrow \left|e, \mathrm{F}' = 2\right\rangle$, where g is the ground state $3S_{1/2}$ and e is the excited state $3P_{3/2}$. Figure 4.5 shows a schematic with detunings of the beams used in the exoeriment. One can see that all paths are detuned from their main laser by at most 200 MHz.

The beams branching out from the cooling-light laser are all coupled into

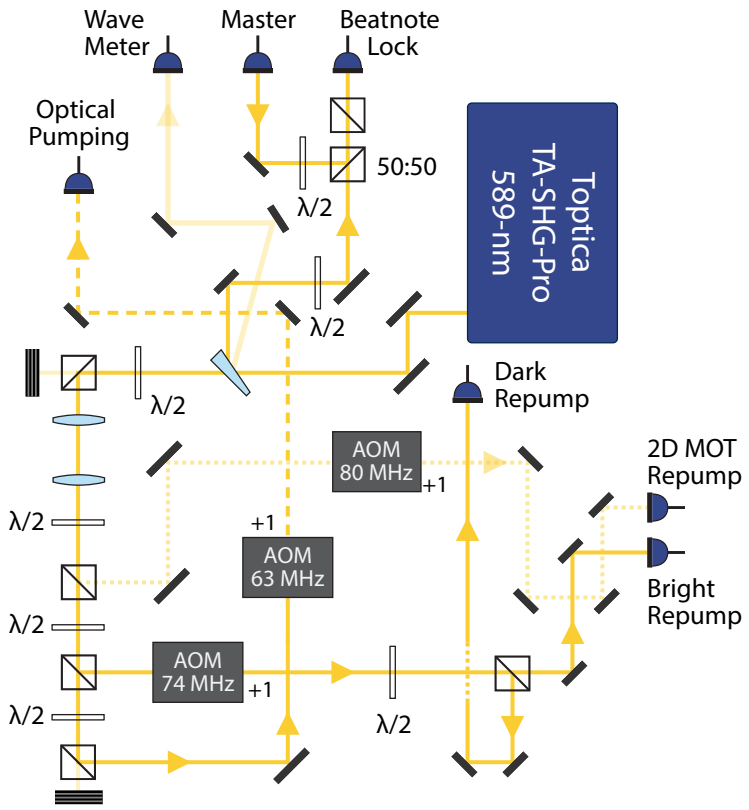

Figure 4.6: Repumping light laser setup (589 nm). The laser frequency is stabilized using a beat-note lock (see text for details). The AOM elements indicate the frequency used to drive them. In each case the order used is indicated next to the AOM, for example, "+1". In front of each fiber there is a coupling lens and a shutter (not depicted).

fibers[6] and sent to the production and experiment chambers located on an independent optical table[7]. Each fiber input is preceded by a mechanical shutter — we use SRS SR475 shutters in all 589 nm paths with the exception of the 3D cooling path that uses an old Uniblitz shutter.

The second 589 nm system consists on an additional Toptica TA-SHG-Pro

[6]The fibers used with 589 nm light are single mode, non polarization maintaining fibers from Thorlabs (P1-460B-FC) and from Coastal Connections.

[7]Sending light through fibers is convenient since it decouples alignment of optics needed for tailoring the beams near the vacuum chamber from optics needed to control the frequency and intensity of the beam. Additionally, using single mode fibers clean the mode of the beam that is usually distorted by deflection in the AOM.

system that is used to generate laser light with frequency close to the repumping transition frequency (see figure 4.6). Stabilization of the laser's frequency is achieved using a beat-note lock [65], the basic operation of this lock consists on using a fast photo-diode (Thorlabs DET025AFC) to detect the beat-note signal between a master laser (light coming from the cooling laser system) and light from the repumping laser system. The signal is amplified and sent to a phase-locked loop (PLL) which compares the signal to a reference RF signal from a function generator. The output of the PLL is used to control the repumping laser's piezoelectric voltage[8,9].

4.2.2 Laser Systems for Optical Dipole Traps

The laser systems previously mentioned are sufficent to produce a 3D MOT of sodium. The remaining laser systems are used to cool the atoms to degeneracy in a hybrid magnetic-optical trap [55] and to tailor arbitrary potentials to confine the BEC. The laser systems in question are two IPG Photonics lasers, one that produces 532 nm wavelength light, and one to produce 1064 nm wavelength light, figure 4.7 shows a schematic of these laser setups.

There are two main differences between these two systems and the 589 nm laser systems. First, we do not care about the precise frequency of the ODT lasers since they are far-detuned from any atomic transition; therefore, we do not stabilize the frequency of the lasers. Second, the power coupled into the fibers is higher than in the 589 nm systems. While the power sent into the 589 nm system fibers is at

[8]The piezoelectric actuator forms part of the external-cavity diode-laser and tunes its frequency by finely adjusting the length of the cavity.

[9]The signal from the PLL can be alternatively used to control the diode current. This lock system is designed to be able to lock the phase of the laser and not just the frequency.

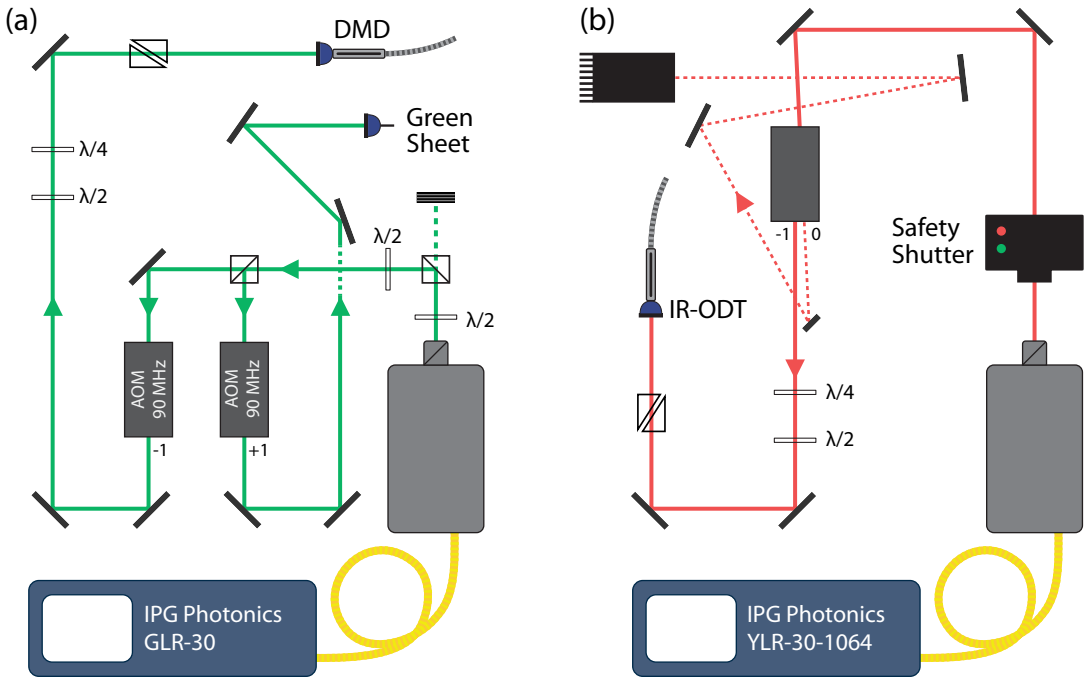

Figure 4.7: Optical Dipole Traps Laser Systems. (a) 532 nm laser system. System used to produce blue-detuned ODTs. (b) 1064 nm laser system. System used to produce the red-detuned ODT. The fibers used for the DMD path and the IR-ODT are photonic crystal fibers from NKT Photonics.

most 350 mW, the power sent into the DMD fiber and the IR-ODT fiber exceeds a couple of watts. We found that the optical fibers used in the laboratory for lower powers do not perform well at high power, resulting in power instability on the output. Consequently, we use photonic crystal fibers from NKT Photonics for the DMD path (LMA-PM-10) and the IR-ODT (15P SMA-905).

4.2.3 Laser Beams and Vacuum Chamber

The schematics shown in Fig. 4.8 and Fig. 4.9 show the orientation of the beams as they are sent into the chamber to address the atoms, the first diagram shows a top view of the chamber and all of the beams necessary to produce a 3D

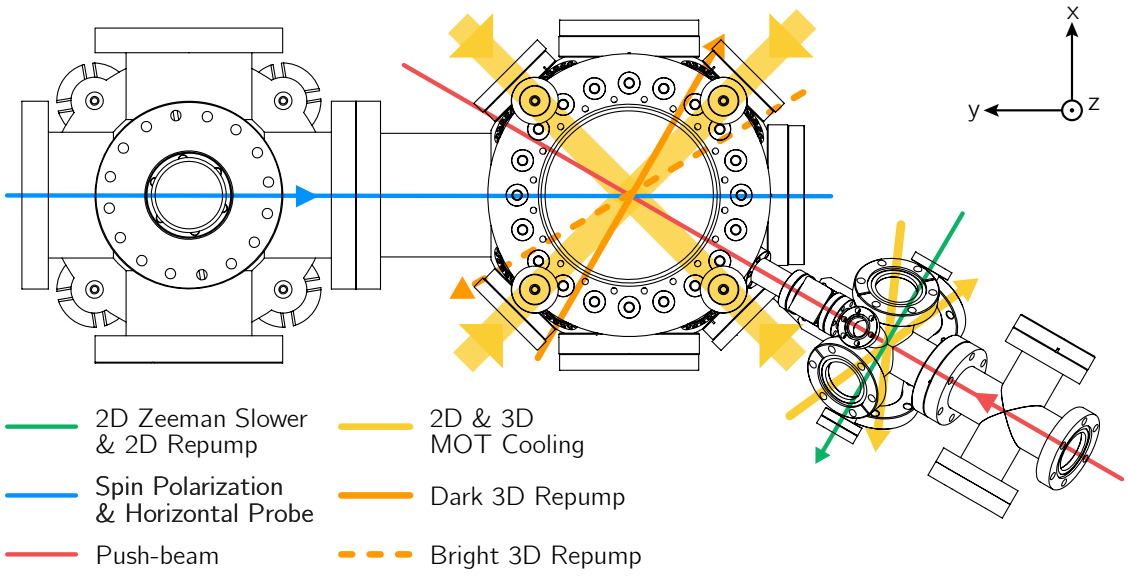

Figure 4.8: Top view of the vacuum chamber and laser beams for 3D MOT production. There are three pairs of orthogonal, counter propagating 3D cooling beams, two pairs on the x-y plane and a third pair that travels along z at the center of the experiment chamber. In the case of the 2D MOT there are only two orthogonal cooling beams that are retro-reflected (mirrors not depicted), the 2D MOT is formed along the axis of propagation of the push-beam which is orthogonal to the plane defined by the 2D MOT cooling beams. The 2D Zeeman slower and repump travel against the flow of the atomic beam coming out of the sodium oven (oven not depicted).

MOT, while the second diagram shows the beams corresponding to the ODTs. A detailed discussion on the production of the 3D MOT and BEC will be presented in chapter 5, additional details on the optics used to generate the blue-detuned ODTs will be presented on section 4.4.

The right side of Fig. 4.8 shows in yellow the two orthogonal cooling beams that are sent into the chamber to produce a 2D MOT, these beams come out of the fiber and are allowed to expand freely. A 2 in. diameter, 75 mm focal length lens then collimates the beams ($1/e^2$ radius ≈20 mm). The beams are circularly polarized, one of them is left-hand polarized while the other one is right-hand polarized, the

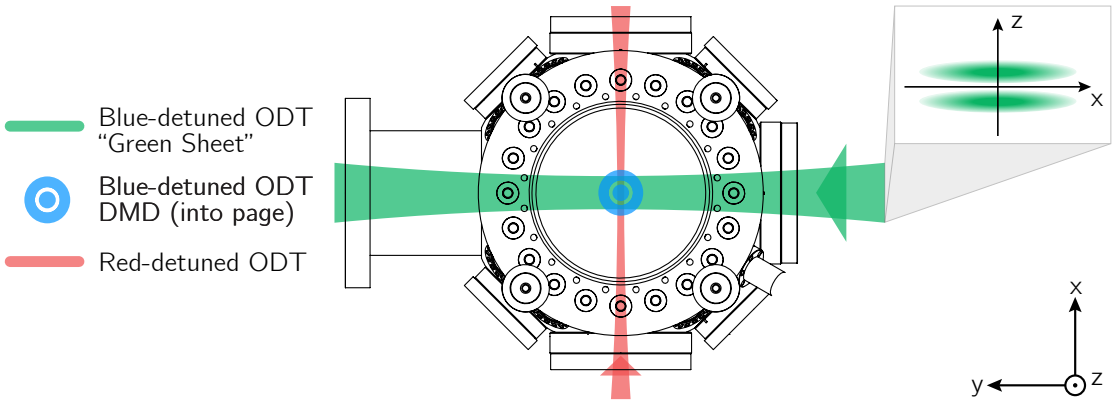

Figure 4.9: Top view of the vacuum chamber and ODT laser beams. The red detuned ODT and the green-sheet ODT are focused at the center of the chamber where the atoms are trapped. The inset depicts a cross section of the green-sheet trap showing the double lobe structure of the beam.

polarization is set using fiber paddles (Thorlabs FPC560). The green arrow in the figure indicates the direction of the 2D Zeeman Slower beam and the 2D repumping beam, each of these beams comes out of its own fiber and is collimated before passing through a half-wave retarder and a quarter-wave retarder, each, to control the polarization. Then, two independent telescopes are used to expand each beam to a $1/e^2$ radius $\approx$10 mm, after being expanded to their final size the beams are combined using a polarizer beam splitter (PBS) and sent into the chamber. The red beam depicted in Fig. 4.8 indicates the axis of propagation of the push-beam which is the axis along which the 2D MOT is oriented. This beam pushes the atoms through the differential pumping tube into the science chamber and crosses the chamber at its center.

The yellow beams on the science chamber side of Fig. 4.8 come out of a fiber splitter from Evanescent Optics[10] that has two inputs and six outputs. Each output

[10]Custom fiber splitter (S.N. 7428-1).

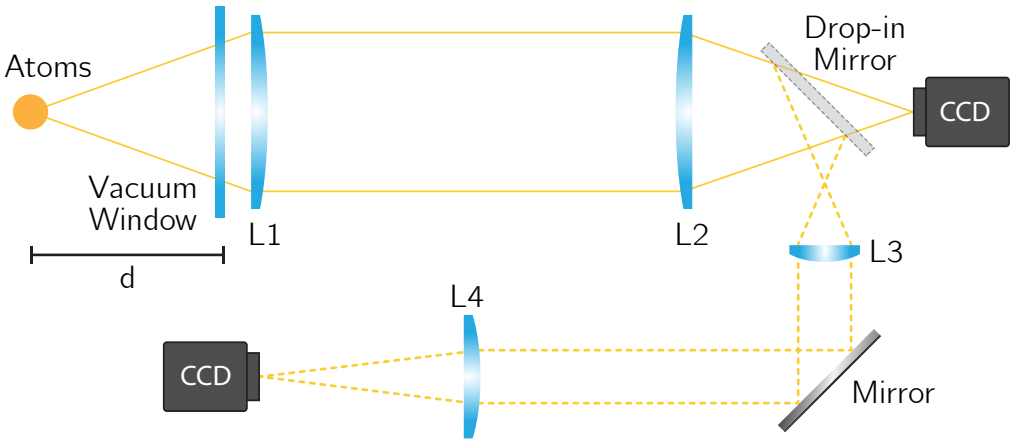

Figure 4.10: Horizontal Imaging. All lenses are commercial (see Table 4.1). Both cameras are Fleas (FL3-FW-20S4M).

is collimated, then expanded using a telescope, and finally goes through a half-wave retarder and a quarter-wave retarder to set the polarization as described in Fig. 3.5. The orange arrows indicate the orientation of the bright-repump and the dark-repump. The blue line indicates the axis of propagation of the beam used for spin polarization (optical pumping) and the horizontal probe. The spin polarization beam is collimated and sent though a Glan-Thompson polarizer (Thorlabs GTH10), it is then combined with the horizontal probe—that has been collimated out of the fiber—using a PBS.

4.3 Imaging Systems

Ultracold atom experiments, this one included, rely on images of the cloud as the main probing technique [30]. We use resonant absorption imaging and partial-transfer absorption-imaging (PTAI) to image the atoms in-situ and in time of flight. There are two imaging systems, a horizontal imaging system and a vertical imaging

system. The vertical imaging system is distinct in that it serves a dual purpose, it is used to both image the atoms and project arbitrary potentials on them. This section provides a brief overview of both systems. Additional information on the design and characterization of the systems can be found in Appendix A.

4.3.1 Horizontal Imaging

The horizontal imaging system, shown in Fig. 4.10, consist of a main 4f-telescope imaging path with magnification $M_{\mathrm{H1}} \approx 0.99$ and a Flea camera (FL3-FW-20S4M)[11]. An auxiliary path is available with the use of a drop-in mirror. This additional path relays the image using a two-lens telescope, the combined magnification is $M_{\mathrm{H2}} = 5.10(3)$, the image is captured by another Flea camera (FL3-FW-20S4M).

Lens	Part Number	f (mm)
L1	AC-508-200-A	200
L2	AC-508-200-A	200
L3	AC-254-100-A	100
L4	AC-508-500-A	500

Table 4.1: Lenses used in the horizontal imaging system. All lenses are form Thorlabs.

4.3.2 Vertical Imaging

The vertical imaging system, shown in Fig. 4.11, consist on a microscope formed by a high NA objective (see Appendix A for a detailed description) and a lens with 500-mm focal length. The real image formed by the microscope is re-imaged onto an electron-multiplied CCD (EMCCD) camera, Andor iXon-DV887,

[11]The Flea cameras are from FLIR which was formerly Point-Grey

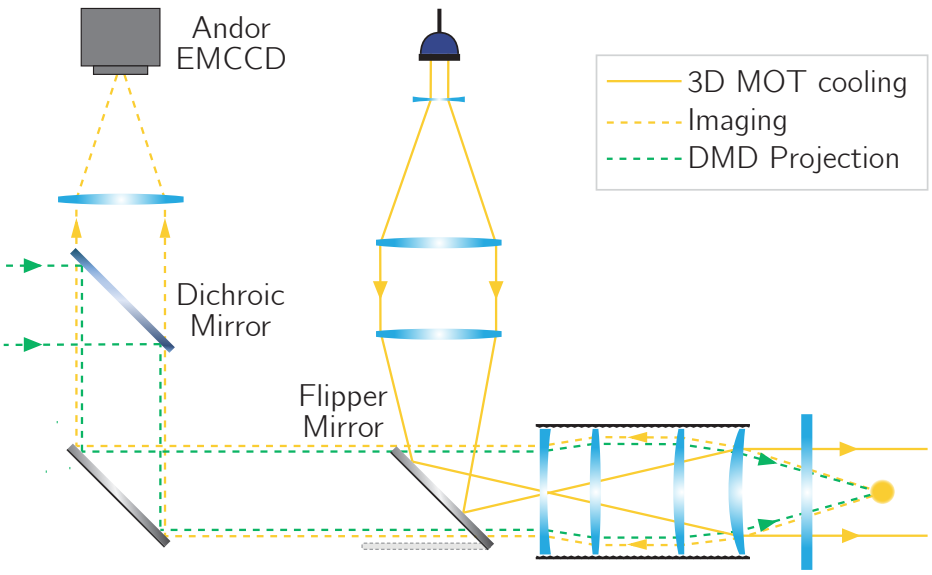

Figure 4.11: Vertical imaging system. There are three paths going through the microscope objective: the vertical imaging path (dashed yellow lines), the path for the top 3D-MOT cooling beam (solid yellow lines) and the DMD projection path (dashed green lines). Switching between paths is done with the aide of a motorized flipper mirror (Newport 8892-K).

with a zoom lens from Edmunds Optics (VZM 1000 Zoom Imaging Lens). The total magnification of the vertical imaging path is $M_{\mathrm{V1}} = 40.3(6)$.

In addition to imaging the atoms along the gravity axis, the vertical imaging system is used to project arbitrary potentials resulting from relay-imaging a digital micromirror device (DMD). Additional details on the DMD path are discussed in Section 4.4.2.2.

4.4 Blue-Detuned ODTs

We are interested in studying the dynamics of a BEC in arbitrarily-shaped traps. In order to tailor arbitrary traps created by light we first confine the condensate in a highly anisotropic potential such that $\omega_z/\omega_\perp \gg 1$, where ω_z is the vertical

trapping frequency and $\omega_\perp$ is the transverse trapping frequency. This anisotropy guarantees that the energy level spacing along one dimension exceeds the interaction energy between the atoms. In this case the particles obey 2D statistics but interact in the same way as in a 3D system [66].

The vertical confinement of the condensate is provided by a blue-detuned dipole trap that, at the position of the atoms, to first approximation has the intensity profile of a Hermite-Gaussian TEM_{01} beam. For a blue-detuned dipole trap, the atoms are confined in the antinode of the intensity profile; we call this the green-sheet trap and it will be discussed further in section 4.4.1. Horizontal confinement is provided by a second blue-detuned dipole trap that results from imaging a digital micromirror device (DMD) onto the atoms; a detailed description of the DMD system can be found in section 4.4.2.

4.4.1 Blue Detuned TEM_{01} Dipole Trap

The green-sheet trap is produced by an elongated Gaussian beam (TEM_{00}) that passes through a π-phase plate which imprints the top half of the beam with a π phase relative to the bottom half. The beam is then focused onto the atoms by a spherical lens. The intensity of the beam at the focal plane is given by [67]

$$I_{\mathrm{foc}}(x,z) = \frac{2P}{\pi w_x w_z}\,\mathrm{erfi}\left(\frac{z}{w_z}\right)^2 \exp\left(-\frac{2z^2}{w_z^2}\right)\exp\left(-\frac{2x^2}{w_x^2}\right), \tag{4.1}$$

where P is the total power of the beam, ω_x the beam waist along the x-axis and ω_z the beam waist along the z-axis. The beam propagates along the y-axis and gravity

acts along the z-axis. For small values of z, the error function in equation (4.1) can be approximated by $\mathrm{erfi}(z) \approx 2/(\sqrt{\pi})z$,

$$\begin{aligned} I_{\mathrm{foc}}(x,z) &\approx \frac{2P}{\pi w_x w_z}\left(\frac{2z}{\sqrt{\pi}w_z}\right)^2 \exp\left(-\frac{2z^2}{w_z^2}\right)\exp\left(-\frac{2x^2}{w_x^2}\right), \\ &= \frac{1}{\pi}\frac{8P}{\pi w_z^3 w_x} z^2 \exp\left(-\frac{2z^2}{w_z^2}\right)\exp\left(-\frac{2x^2}{w_x^2}\right), \\ &= \frac{1}{\pi} I_{\mathrm{TEM}_{01}}(x,z). \end{aligned} \tag{4.2}$$

The phase plate is located at the Fourier plane of a 4-f imaging system that focuses the beam onto the atoms. As previously noted by other groups working with similar traps [66], the alignment of the phase plate is very sensitive. Even a 1 mm offset with respect to the beam propagation axis can result in deviations from the ideal TEM_{01} mode. This results in increased intensity between the bright lobes of the beam which causes a repulsive force at the position of the atoms.

4.4.2 DMD Potential

The transverse confinement consists of another blue-detuned dipole trap. In this case, the intensity profile of the beam is shaped with a DMD, a type of Spatial Light Modulator (SLM). The DMD is a bistable[12] spatial light modulator, consisting of an array of movable micromirrors mounted over a CMOS memory cell. The mirror

[12]Flat state occurs when the mirrors are not energized. This is not an active state of the DMD mirrors (not tristable). The resting position of the mirrors is nominally zero degrees, but the mirrors are not controlled or actuated to this position and may vary from it slightly. Flat-state mirrors exist only when the device is turned off, or parked, and no image is being formed.

Property	Value
DMD Array Size	1024×768
Micromirror Pitch (d)	13.68 μm
Micromirror Tilt Angle (γ)	12°
Micromirror Reflectivity	88%
Array Diffraction Efficiency	86%

Table 4.2: DMD Specifications. We work with a Texas Instruments DMD (DLP7000) controlled by a development kit from Digital Light Innovations (DLP Discovery D4100).

states are either $+\gamma$ degrees (*on* position) or $-\gamma$ degrees (*off* position). The tilt of each mirror is independently controlled by loading data into the memory cell below the mirror and can be dynamically updated by means of an external trigger.

Since the DMD is a 2D array of periodically spaced mirrors, diffractive effects, especially when illuminating the DMD with coherent light, must be understood and taken into account.

4.4.2.1 Diffraction from a DMD

The intensity distribution of a homogeneous monochromatic beam after it diffracts from a single slit[13] [68, 69, 70] can be written as,

$$I(\theta) = I_0 \operatorname{sinc}^2 \left[\frac{\pi a}{\lambda} (\sin\theta + \sin\theta_i) \right], \tag{4.3}$$

where I_0 is the intensity of the incident beam, a is the slit width, θ_i is the angle of incidence and λ is the wavelength of the illuminating beam. In the case of multiple

[13]The sign convention for angles in this derivation is: clockwise measured angles are positive, counter-clockwise measured angles are negative. For example, in figure 4.12 both incident angles are negative.

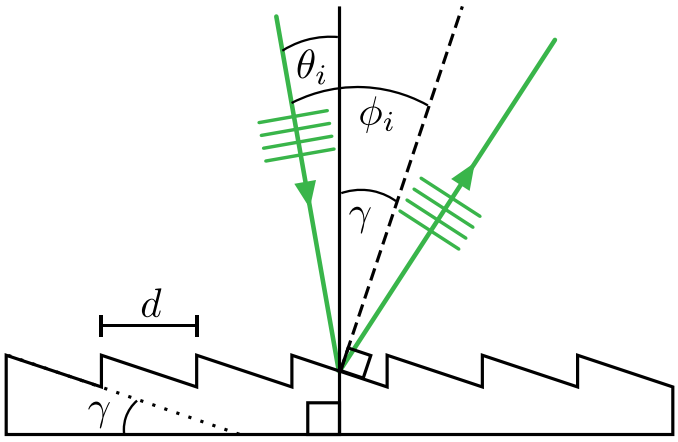

Figure 4.12: Schematic of a blazed Grating. The etched grooves from an angle γ with respect to the plane of the grating and have a width d. The solid vertical line represents the normal to the grating, the dashed line is the normal to the face of a groove. The incident beam forms an angle θ_i with respect to the grating normal, the incident angle measured with respect to the groove's normal is $\phi_i = \theta_i + \gamma$.

slit diffraction a similar expression is found

$$I(\theta) = I_0 \operatorname{sinc}^2\left[\frac{\pi a}{\lambda}(x + x_i)\right] \times \left[\frac{\sin\left(\frac{N\pi d}{\lambda}(x + x_i)\right)}{\sin\left(\frac{\pi d}{\lambda}(x + x_i)\right)}\right]^2 . \tag{4.4}$$

Here, $x = \sin\theta$, $x_i = \sin\theta_i$, N is the number of slits and the slit pitch is denoted by d. From equation (4.4) it follows that the diffraction orders will be located at angles θ_m that satisfy the grating equation

$$\sin\theta_m + \sin\theta_i = \frac{m\lambda}{d}. \tag{4.5}$$

The power diffracted from the grating into a non-zero order can be enhanced by decoupling the specular reflection envelope given by the sinc function from the diffraction orders given by the last term of equation (4.4). This is commonly achieved by engineering a reflective grating with a cross section that resembles a sawtooth,

like that schematically depicted in figure 4.12. These types of gratings are known as blazed gratings.

The slit's pitch (d) and width (a) of a blazed grating are equal, $a = d$. In this case the intensity of the diffracted beam is

$$I(\theta) = I_0 \operatorname{sinc}^2\left[\frac{\pi d}{\lambda}(\tilde{x} + \tilde{x}_i)\right] \times \left[\frac{\sin\left(\frac{N\pi d}{\lambda}(x + x_i)\right)}{\sin\left(\frac{\pi d}{\lambda}(x + x_i)\right)}\right]^2 . \tag{4.6}$$

Here, $\tilde{x} = \sin\phi$, $\tilde{x}_i = \sin\phi_i$, the angles ϕ are measured with respect to the groove's normal while angles θ are measured with respect to the grating normal (see figure 4.12). The intensity envelope is now centered at the specular reflection with respect to the groove surface, $\phi_r = -\phi_i$. Nevertheless, the diffraction orders remain centered at the specular reflection with respect to the grating normal, $\theta_r = -\theta_i$.

When the angle of incidence is such that a non-zero diffraction order is aligned with the intensity envelope it is said that the grating is in blaze configuration. If in addition we constraint the envelop to be centered at the grating normal, the blaze condition can be written as

$$\sin(2\gamma) = \frac{m\lambda}{d}. \tag{4.7}$$

The geometry of a DMD is that of a 2D blazed grating, therefore the intensity envelope of a DMD is,

$$\operatorname{Sinc}^2\left[\pi\frac{a_x}{\lambda}(x + x_i)\right] \operatorname{Sinc}^2\left[\pi\frac{a_y}{\lambda}(y + y_i)\right], \tag{4.8}$$

where a_j is the grating pitch along the j-axis. The generalization of equation (4.7)

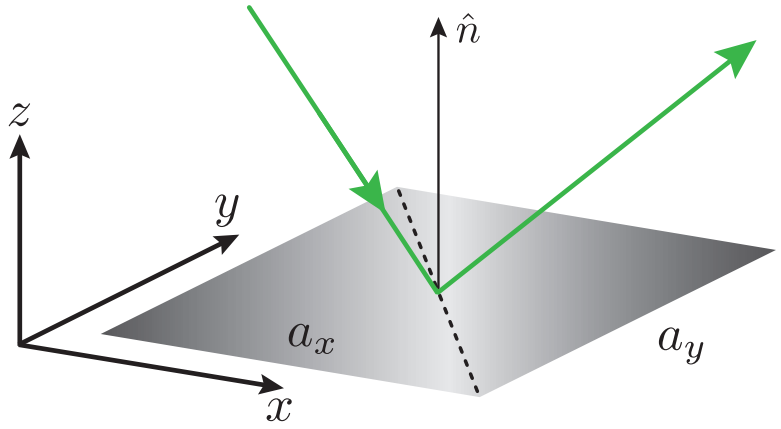

Figure 4.13: Micromirror geometry. The dashed line represents the mirror axis of rotation. The mirror's tilt about this axis is $\pm\gamma$ degrees.

to 2D is

$$\sin\theta_{m,j} + \sin\theta_{i,j} = \frac{m_j\lambda}{a_j}, \tag{4.9}$$

with $j = x, y$ and θ_j the projection of the incident angle on the z-j plane. The model of DMD that we work with has been designed for corner illumination, the mirror tilts about its diagonal (see figure 4.13). In this case the equations are simplified since $\gamma' = \arctan\Big(\tan(\gamma)/\sqrt{2}\Big)$. As a result, the intensity envelope can only be centered on diffraction orders with $m_x = m_y$ [71].

4.4.2.2 DMD Optical Setup

The optics used to image the surface of the DMD onto the atoms consist of three achromatic doublets and a custom made objective (for more details see Appendix A). The first two lenses ($f_1 = 500$ mm and $f_2 = 150$ mm) form a 4-f system with magnification $M_1 \approx f_1/f_2 = 0.3$. An aperture at the Fourier plane of this system blocks undesired diffraction orders. A second imaging system formed by

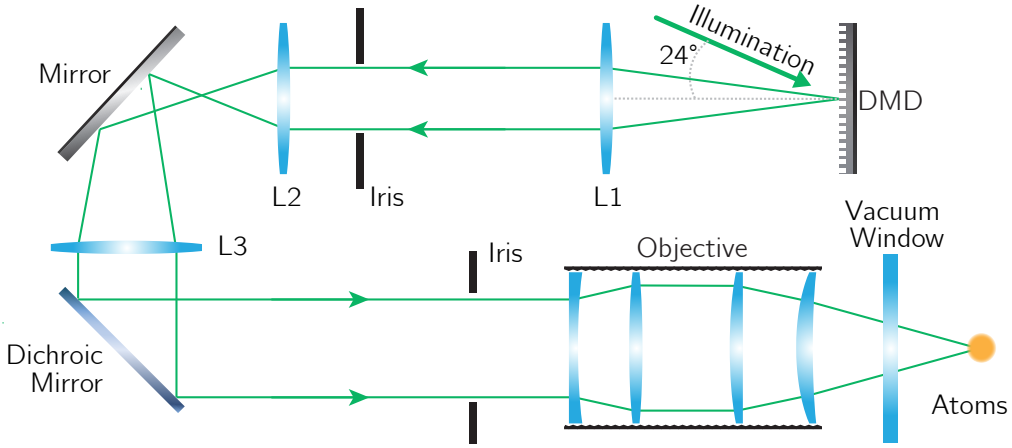

Figure 4.14: DMD optical setup. The DMD is illuminated with a collimated beam incident at an angle $\approx 24°$, the reflection propagates along the optical axis of the system that is normal to the plane defined by the DMD array. The first pair of lenses (L1 and L2) demagnify the DMD pattern by a factor of ≈3.3, an iris placed at the Fourier plane of L1 blocks undesired diffraction orders. Lens L3 and the objective further demagnify the DMD pattern by a factor of ≈ 7.4.

an achromat ($f_3 = 500$ mm) and the high NA objective (EFL = 68 mm) relays the image of the DMD surface and projects it onto the atoms. The magnification of the relay system is $M_2 \approx \text{EFL}/f_3 = 0.136$. The effective magnification of the projection optics is expected to be $M_{\text{DMD}} \approx M_1 M_2 = 0.04$, from characterization in situ the magnification of the path is $M_{\text{DMD}} = [28.6(4)]^{-1}$.

The magnification of the projection optics was chosen such that a micromirror of size $d = 13.68$ μm maps to a feature, on the plane of the atoms, smaller than the resolution of the objective. In this case the size of a micromirror on the plane of the atoms is expected to be

$$d' = M_{\text{DMD}}\, d = 0.479(7)\, \mu m. \tag{4.10}$$

The potential that the atoms will experience is the result of the convolution

of the DMD mask and the imaging system's point spread function (PSF); the PSF FWHM is approximately 2 μm. Since more than one micromirror contributes to the formation of a point-like image on the atoms plane, error-diffusion techniques can be implemented to smooth the potentials and to achieve intermediate intensity levels between the DMD allowed on/off states [22, 72].

4.5 Computer Control

There are two main computers used to run the experimental apparatus, a control computer that synchronizes the operation of all peripherals and an acquisition computer that controls the cameras. The control computer runs JQI's LabVIEW based control software (SetList[14]) which controls the master device (SpinCore Technologies Inc. PulseBlasterUSB) and the slave devices (two PCIe NI cards, one USB NI card and the DMD), see Fig. 4.15. The PulseBlaster has 24 digital output channels (DOs), four DOs are reserved for the slave devices, and the remaining control various equipment in the laboratory including triggering the cameras; the NI cards provide additional DOs and analog outputs (AOs). Communication between the control computer and the DMD via USB[15] allow loading of frames onto the DMD memory which are then refreshed upon triggering during the experimental sequence. Currently, the memory of the DMD is loaded at the beginning of each cycle and cleared at the end of each cycle[16]. The data acquired in our experiment consists of

[14]The SetList code and documentation are available on Github: https://github.com/JQIamo/SetList.

[15]The ground between the computer and the DMD is broken using an optical fiber extender.

[16]This is a time sink in the experimental sequence since the loading process takes approximately 1 s per 10 frames at the beginning of a cylce.

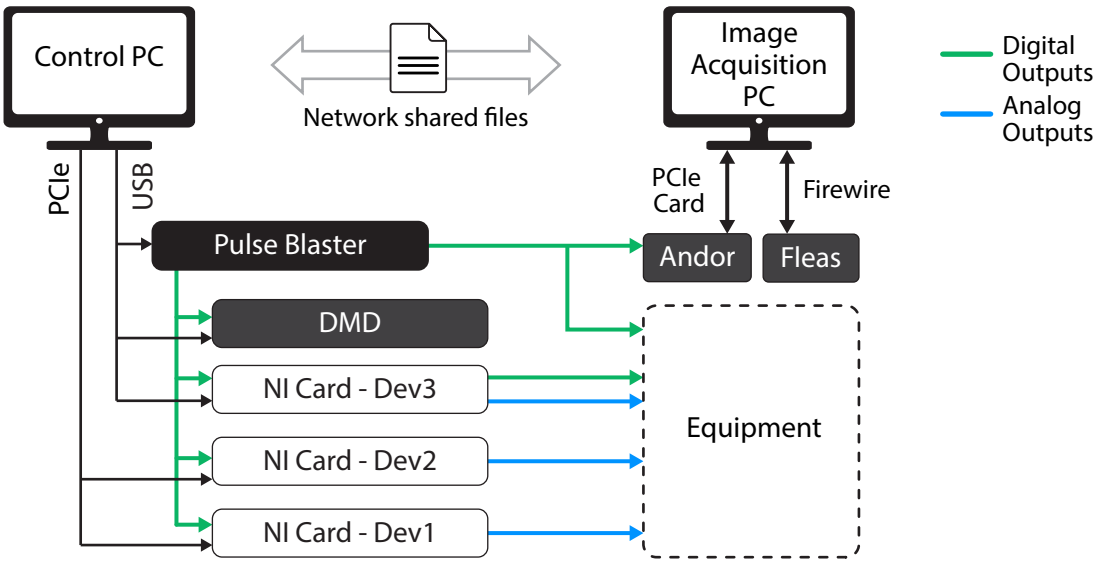

Figure 4.15: Schematic of the computer control and periphereals.

images of the atoms. The cameras used for this purpose are triggered by the Pulse-Blaster and image acquisition is performed by a dedicated computer. The control computer and image acquisition computer communicate via network shared strings.

Chapter 5: Toroidal BEC Production

This chapter describes the experimental sequence used to produce BECs in a toroidal trap as well as relevant characterizations. The first four sections cover the basic procedures to produce a BEC in a hybrid (ODT-Magnetic) trap, section 5.5 describes the process to transfer the BEC from the hybrid trap into a blue-detuned ODT. Section 5.6 discusses in detail the ring potential as well as the process to generate phononic excitations in the BEC. Section 5.7 describes the data processing of PTAI images of the condensate. In this chapter words written in `monospaced font` refer to variables used in the experimental sequence within SetList.

5.1 3D MOT

The experimental sequence begins by transferring atoms from the 2D MOT into the 3D MOT, during this time all the beams needed to produce a 2D MOT—2D cooling beam, 2D repumping beam, Zeeman slower beam— as well as the beams to produce the 3D MOT—3D cooling beams and dark repumping beam—and the push beam are kept on. We load atoms directly into the dark spontaneous-force optical trap (dark SPOT) [73]—we will refer to this trap as the dark MOT—instead of loading into the bright 3D MOT and then transferring into the dark MOT. We

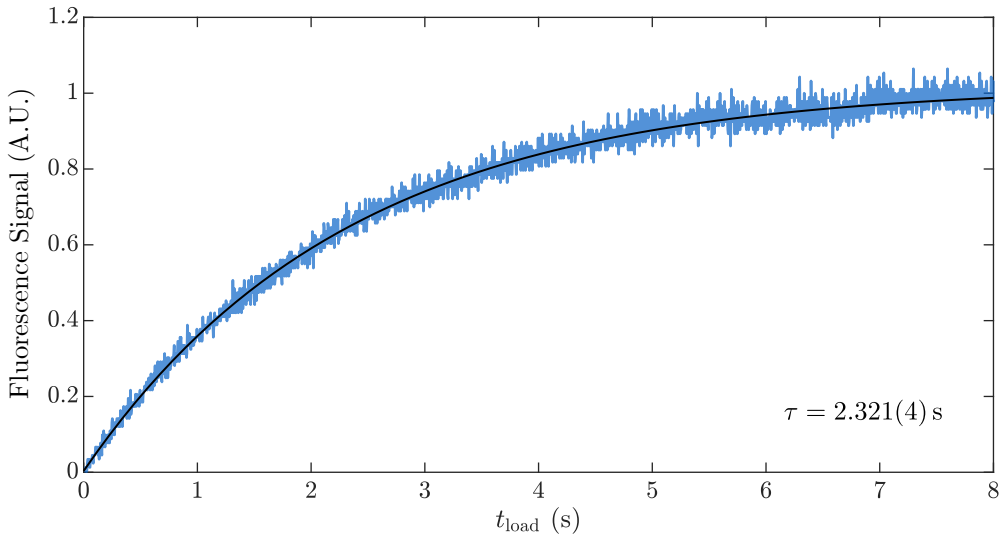

Figure 5.1: 3D MOT loading time. The plot shows in blue the signal from a fluorescence monitor that records fluorescence from the 3D MOT as a function of loading time (t_{load}), the black curve is the fit to the normalized data $[1 - \exp(-t/\tau)]$ with time constant $\tau \approx 2.3$ s.

made this decision because we saw no improvement in atom loading times when we implemented the latter scheme. Figure 5.1 shows the load of the dark MOT under optimal conditions based on atom fluorescence captured by a photodetector, in this case the loading time constant is $\tau \approx 2.3$ s; we note, however, that a time constant of 3 s better represents the loading of the dark MOT under regular operating conditions[1]. Consequently, we load the dark MOT for 10 s which corresponds to $\approx 96\%$ of the maximum atom number that can be captured. The magnetic field gradient at this stage is given by `HMOT`, shown in Table 5.1.

[1]The overall performance of the apparatus changes over time due to slow drifts of the alignment of the beams, small fluctuations of laser powers on the fiber outputs, etc.

Name	V_{ctrl} (V)	Current (A)	Gradient (T/m)
HMOT	0.225	7.5	0.097
HQ1	1.6	53.2	0.689
HQ2	5.5	182.7	2.367
HQ3	0.22	7.3	0.095
HQ4	0.2	6.6	0.086
HSG	0.5	16.6	0.215

Table 5.1: Values of the magnetic field gradient during the experimental sequence. The power supply is run in voltage mode, the current is sensed by a hall probe.

5.2 Sub-Doppler Cooling

After loading the dark 3D MOT, the 2D MOT beams and the push beam are turned off; the magnetic field gradient is also switched off. We then linearly scan the frequency modulation (FM) and amplitude modulation (AM) of the AOM used to generate the 3D cooling beams in order to achieve sub-doppler cooling—polarization gradient cooling (PGC) [27, 74]—. During the 3D MOT and PGC stages the bias fields are kept at a value that nulls the magnetic fields for the MOT. At the end of this stage we turn off the dark MOT repump beam and the 3D cooling beams.

The bias fields are then ramped in 3 ms to the value $\mathbf{B}_0 = (0, 0.4, 0)$ G, which defines a quantization axis along the axis of propagation of the optical pumping beam (see Fig. 4.9 for axis convention), the beam is circularly polarized so that the atoms are transferred into the state $|F, m_F\rangle = |1, -1\rangle$. These values are held for 2 ms during which we shine both cooling light and optical pumping light.

Stage	Ramp Type	`fstart` (MHz)	`fend` (MHz)	Duration (s)
RF1	Linear	60	25	0.5
RF2	Exponential	25	20	3
RF3	Exponential	20	13	3
RF4	Exponential	13	10	2

Table 5.2: Parameters for the RF evaporation sequence. For each stage the type of ramp, initial (`fstart`) and final (`fend`) frequencies and duration of the ramp are indicated.

5.3 Magnetic Trap and RF Evaporation

After spin polarizing the cloud we switch on the magnetic field gradient. The value of the gradient is given by `HQ1` (see table 5.1); simultaneously, we adiabatically ramp the bias field to $\mathbf{B}_0 = (0, 0, -0.1)$ G in 5 ms. We then compress the magnetic trap in 300 ms, going from a gradient `HQ1` to `HQ2`, the gradient is held at `HQ2` during the subsequent four stages of radio frequency (RF) evaporation[2]. Figure 5.2 shows the frequency ramp used during evaporation, the ramp is sectioned into four stages, the first stage is a fast linear sweep followed by three exponential stages.

The frequency ramps are programed using the frequency modulation (FM) functionality of an Agilent arbitrary waveform generator (AWG 33250A), the modulation voltages sent to the AWG are given by the functions[3]:

[2]The RF evaporation sequence was divided into four sections in order to skip frequency ranges that interfere with the operation of one of our lasers. The laser in question was later moved away from the RF antenna to avoid this issue, however, the ramp remained sectioned into four pieces.

[3]All functions in this section are written in Lua which is the mathematical evaluator used within SetList (see section 4.5).

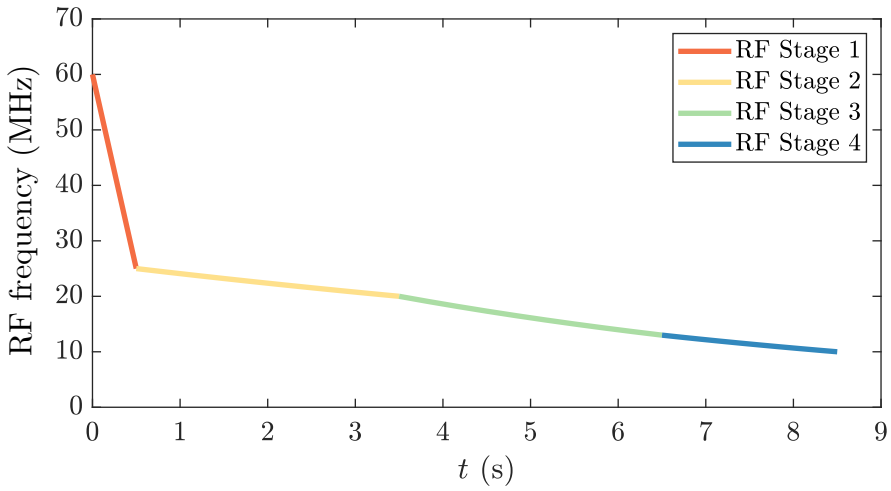

Figure 5.2: Evaporation ramp in the magnetic trap. We scan the radio frequency from 60 MHz to 10 MHz in 8.5 s divided in 4 stages.

```
-- Linear ramp
function RFlin(t,fstart,fend)
    local fc = 40; -- Carrier freq [MHz]
    local fd = 39; -- Deviation freq [MHz]
    local Vstart = 5*(fstart-fc)/fd;
    local Vend = 5*(fend-fc)/fd;
    local Vmod = Vstart + (Vend-Vstart)*(t/tMax);
    return Vmod;
end
-- Exponential ramp
function RFExp2(t,fstart,fend)
    local fc = 40; -- Carrier freq [MHz]
    local fd = 39; -- Deviation freq [MHz]
    local f;
    local Vmod;
    f = fstart*(fend/fstart)^(t/tMax);
    Vmod = 5*(x-fc)/fd;
    return Vmod;
end
```

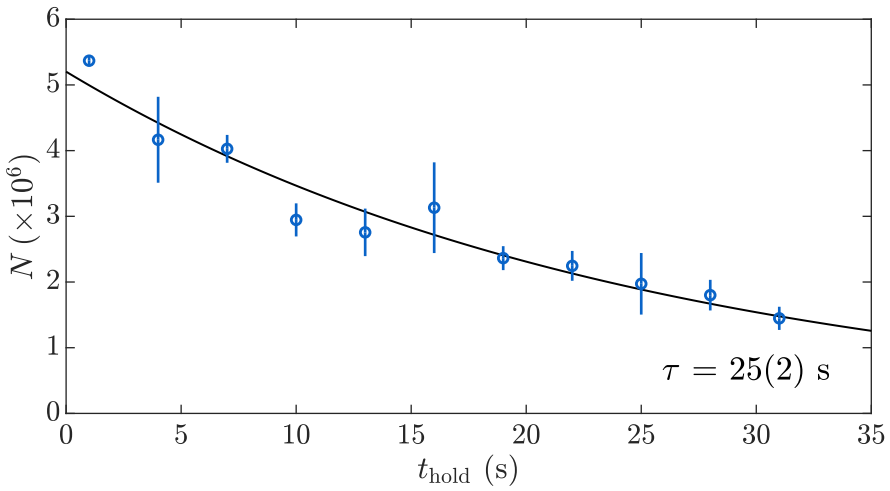

Figure 5.3: Lifetime of the hybrid red-detuned ODT and quadrupole magnetic trap. The symbols are the average and the error bars are the standard deviation of three repetitions, the black curve is the exponential decay fit to the data. The time constant of the trap is $\tau = 25(2)$ s corresponding to a half-life of ≈ 17 s.

5.4 Hybrid Trap: IR-ODT and Magnetic Quadrupole Trap

The atoms reach degeneracy in a trap configuration similar to [55], the confinement consists on a red detuned optical dipole trap (IR-ODT) and an offset quadrupole magnetic trap, for simplicity we will refer from now on to this trap as the "hybrid trap". At the end of the RF evaporation sequence the RF output is switched off, in addition the frequency is parked at 79 MHz to prevent any interaction of the radio frequency with the ultra-cold atoms. The bias magnetic field is adjusted so that the zero field point is moved above the IR ODT. Finally, the magnetic trap is decompressed in 5 s, going from a gradient `HQ2` to `HQ3`. At the end of this stage the atoms are confined in the hybrid trap. Figure 5.3 shows a measurement of the hybrid trap lifetime. To measure the lifetime, after transferring the atoms from the magnetic quadrupole trap to the hybrid trap we hold the atoms for

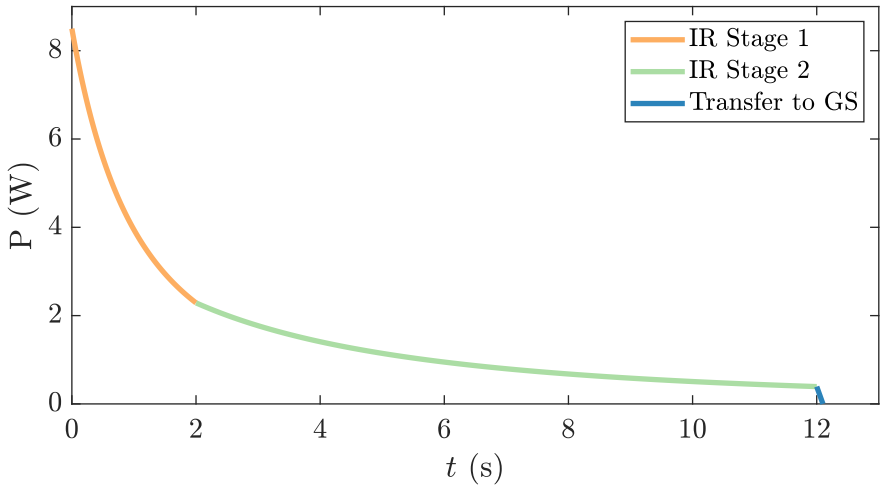

Figure 5.4: Evaporation ramp in the IR ODT.

a variable time t_{hold}, subsequently the atoms are released for a short time of flight (4.5 ms) and imaged using absorption imaging. The atom number is averaged over three repetitions, we fit the data to the model $N(t_{\text{hold}}) = N_0 \exp(-t_{\text{hold}}/\tau)$ from which we obtain the time constant of the trap, $\tau = 25(2)$ s; the half-life of the trap is $t_{1/2} = \tau \log(2) = 17(1)$ s.

After transferring the atoms into the hybrid trap we perform forced evaporation by lowering the power of the IR-ODT, see Fig. 5.4, this stage consists on two "O'Hara" decaying exponential ramps [75]:

```
-- "O'Hara" ramp from A to B, for dipole trap evaporation
function EvapRamp(t, a, b, tau)
    local c = log(a/b) / log(1+tMax/tau); -- constant
    local y = a * (1+t/tau)^(-c);
    return y;
end
```

At the end of forced evaporation—in the hybrid trap—the atoms reach degeneracy, we typically produce condensates with $N \approx 4 \times 10^5$ atoms in $t \approx 40$ s. Figure 5.5

Stage	Duration (s)	a	b	tau (s)
IR Stage 1	2	6.5	1.75	2
IR Stage 2	10	1.75	0.03	8

Table 5.3: Table with values used during evaporation in the IR-ODT. The values a and b indicate setpoints. The maximum setpoint is 6.5 V and corresponds to 8.4 W of IR laser power.

shows the stability in atom number for 60 consecutive repetitions, the condensate atom number fluctuation is typically on the order of 10%.

5.5 Blue-detuned ODTs

Once the atoms are condensed we transfer them into blue-detuned dipole traps. Vertical confinement is provided by the green-sheet trap (as discussed in section 4.4.1), and in-plane confinement is the result of imaging the surface of the

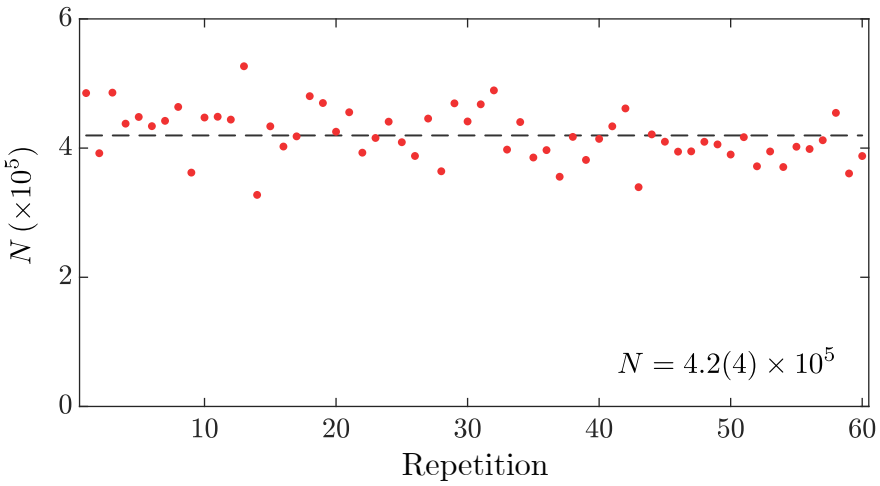

Figure 5.5: BEC atom number stability. The figure shows atom number measured during TOF from the hybrid trap, after the last stage of evaporation. The red circles correspond to 60 consecutive repetitions, the dashed line indicates the mean atom number. We reliably produce condensates with $N \approx 4 \times 10^5$ atoms in $t \approx 40$ s, the atom number fluctuation is typically on the order of 10%.

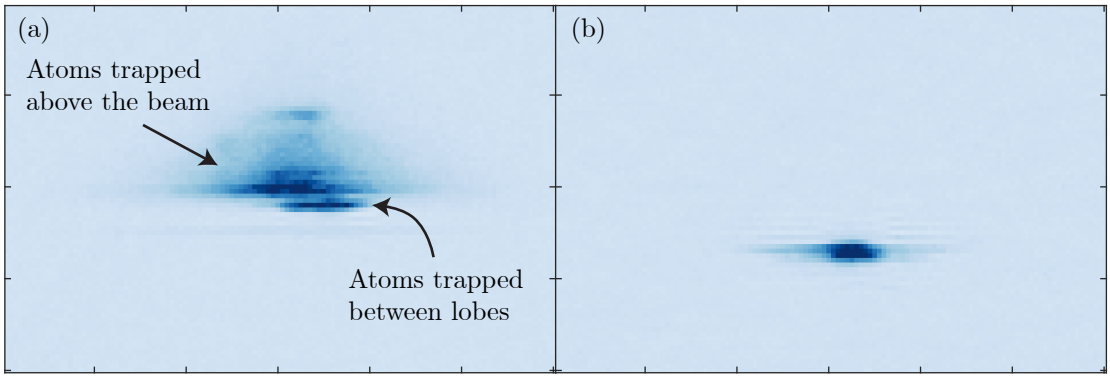

Figure 5.6: Alignment of the green-sheet trap. Images (a) and (b) are in-situ images of the atoms confined by the quadrupole magnetic trap and the green-sheet trap, the images were taken with the horizontal camera (FleaH1) and have the same field of view. Image (a) shows improper alignment that causes atoms to be trapped above the green-sheet beam (TEM_{01}) in addition to the atoms correctly trapped between the lobes of the beam. When the trap is properly aligned, the atoms are trapped only between the lobes of the beam, as shown in (b).

DMD onto the atoms (section 4.4.2); the hand over happens in three stages. First, the IR ODT power is linearly ramped to zero in 100 ms, while maintaining the quadrupole magnetic trap on at `HQ3`, at this stage vertical confinement is provided by the green-sheet that has been kept on[4] since the beginning of the sequence and in-plane confinement is provided by the quadrupole magnetic trap. The atoms are held in this configuration for 100 ms. Then, the power of the DMD trap is ramped over 500 ms from 0 to the maximum value[5] `DMD_SP1`. The initial trap projected with the DMD is a disk that best matches the distribution of the condensate in the green-sheet together with the magnetic trap, this "shape matching" step maximizes the number of atoms transferred into the blue-detuned ODTs. At this stage the atoms are confined by the resulting potential of the quadrupole magnetic trap and

[4]In SetList the green-sheet setpoint is `GS_SP1`= 1.5 V which corresponds to 215 mW of light going towards the atoms.

[5]This setpoint corresponds to 2.5 W of light ($\lambda = 532$ nm) impinging on the DMD, the power sent towards the atoms is 280 mW.

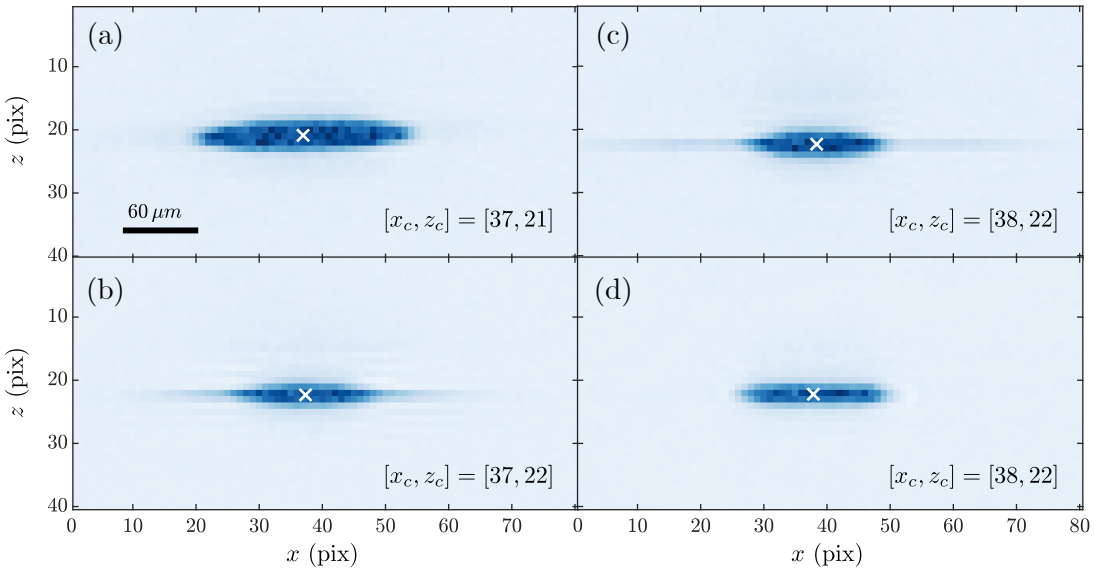

Figure 5.7: Alignment of traps based on horizontal camera positioning. (a) Hybrid trap consisting of IR ODT and magnetic trap. (b) Superposition of IR ODT, magnetic trap and green-sheet. (c) Magnetic trap and green-sheet. (d) Blue ODT consisting of green-sheet trap and DMD trap.

the blue-detuned ODTs. This state is held for 100 ms before finally ramping the magnetic field gradient from `HQ3` to `0`.

5.5.1 Alignment of the Traps

Good overlap between the magnetic trap, IR ODT, green-sheet and DMD trap is crucial to maximize atom number in the final disk trap. The optimization of these traps is based on positioning the atom cloud on the horizontal (Fig. 5.7) and vertical (Fig. 5.8) cameras, as well as on atom number in the final trap. In order to align the IR ODT and the magnetic trap we look at BEC atom number maximization while scanning the bias field; once the optimal bias field has been optimized we note the position of the hybrid trap on the horizontal [Fig. 5.7(a)] and vertical [Fig. 5.8(a)] cameras.

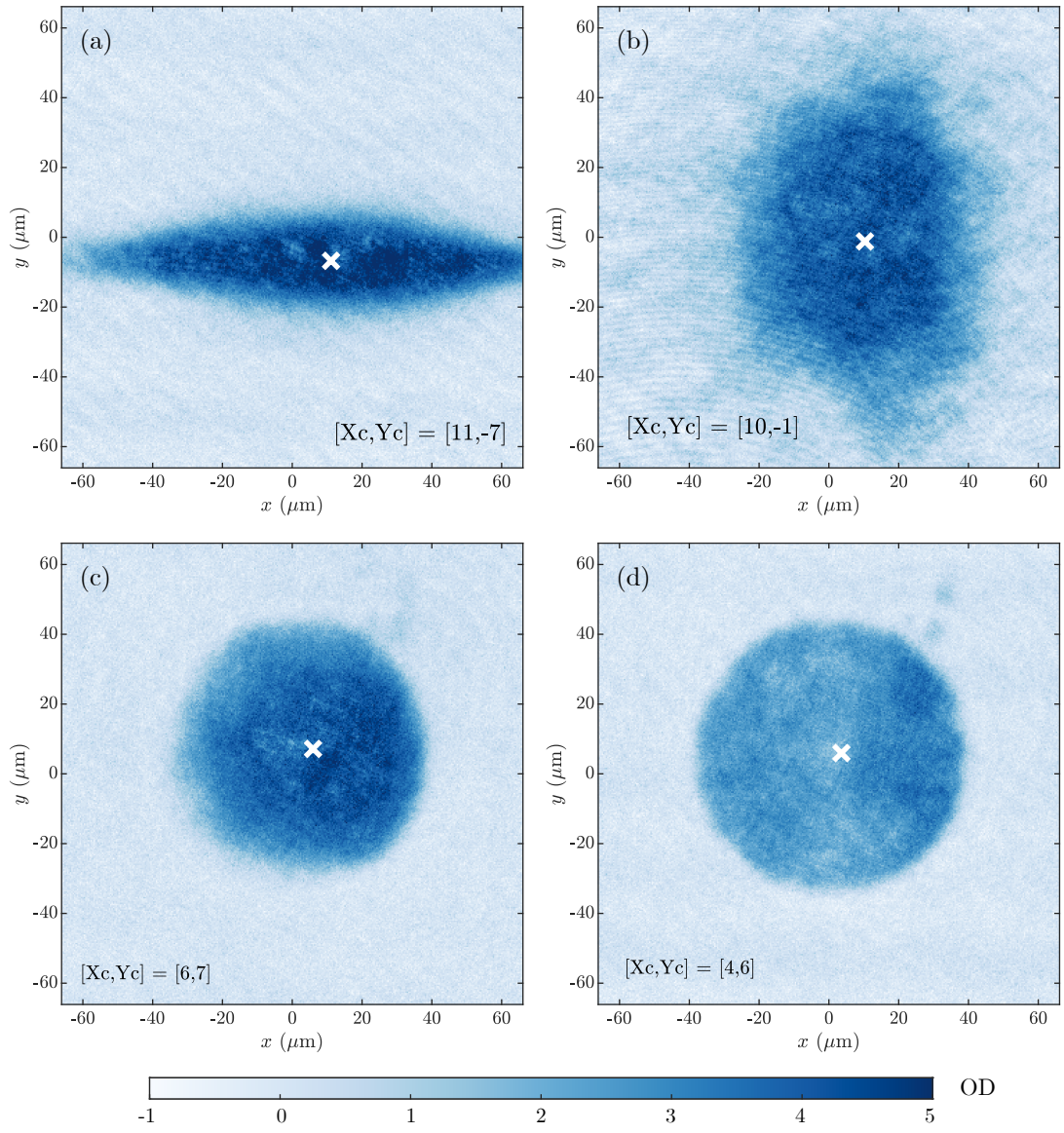

Figure 5.8: Alignment of traps based on the vertical camera positioning. All images have the same field of view and OD color scale. (a) Hybrid trap consisting of IR ODT and magnetic trap. (b) Superposition of IR ODT, magnetic trap and green-sheet. (c) Magnetic trap and green-sheet. (d) Blue ODT consisting of Green-sheet trap and DMD trap, the potential projected with the DMD is a disk that best matches the shape of the Magnetic trap and green sheet from panel (c). The cross marks the center of the cloud $[X_c, Y_c]$ found from a fit.

Once the hybrid trap is aligned, the green-sheet is aligned to overlap the hybrid trap, see Fig. 5.7(b) and Fig. 5.8(b); this alignment relies on turning the knobs on the mirror mounts that steer the beam for the green-sheet trap and translating a lens along the propagation axis of the beam in order to shift the focus of the beam at the position of the atoms. In addition to overlapping the green-sheet and hybrid traps we ensure that the green-sheet is not tilted by turning off the hybrid trap while keeping the green-sheet trap on, waiting a variable time t_{wait} and then imaging the atoms in-situ. When the green-sheet is tilted the center of mass of the cloud shifts as a function of t_{wait}. We iterate alignment of the trap until the center of mass stops shifting while maintaining good overlap with the hybrid trap. It is worth noting that it is possible to trap atoms above the two lobes of the green-sheet TEM_{01} beam, as opposed to in between the lobes as is shown in Fig. 5.6(a). This improper trap configuration happens when the IR beam does not intersect the TEM_{01} beam between the bright lobes, in order to fix this problem one should iterate aligning the IR beam and the green-sheet beam until they properly overlap resulting in confinement of the atoms as shown in Fig. 5.6(b). This process can take multiple iterations since the tilt and steer of the green-sheet trap are coupled—we do not have independent knobs (enough degrees of freedom) to change one without affecting the other—, it is strongly advisable to switch between horizontal and vertical imaging multiple times throughout the process since using a single camera to perform this alignment can be misleading.

The final step to align the traps consists of overlapping the disk trap projected by the DMD and the green-sheet. This is done by steering the DMD beam using the

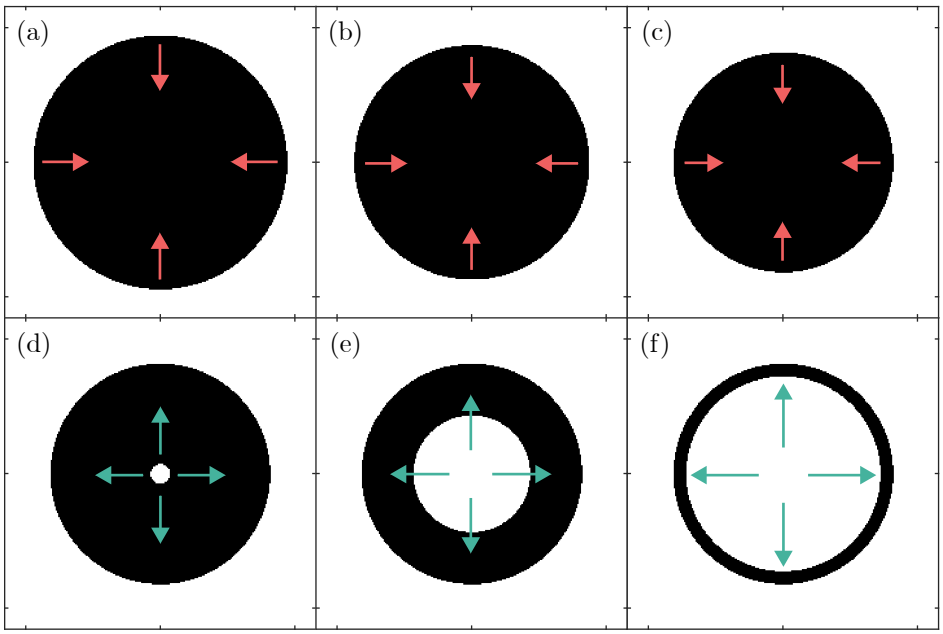

Figure 5.9: DMD frames: disk morphed into ring. Images (a)-(f) show the images projected by the DMD (cropped to the region of interest). The white (black) region corresponds to mirrors turned "on" ("off"), the atoms are confined in the dark region of the beam corresponding to the projected shape in black. Images (a)-(c) show the process of contracting the disk outer radius, as indicated by the red arrows. Image (d) shows the disk being pierced, subsequently the hole radius is expanded (d)-(f), as indicated by the green arrows, until reaching the size of the ring trap inner radius in (f).

knobs on the mount of the last mirror in the DMD path, right before the dichroic. Additional details on the alignment of the DMD beam are presented in appendix A.9.

5.6 Toroidal Trap and Phonon Modes

After confining the condensate in the disk-shaped blue-detuned ODT, the in plane confinement provided by the DMD trap is morphed from a disk into a ring—the disk diameter is reduced to the size of the ring outer radius followed by piercing the disk and expanding the inner hole to the size of the ring inner radius—. The process of going from a disk to a ring is schematically shown in Fig. 5.9, the images

in the figure represent the region of interest (ROI) from the actual frame image loaded into the DMD memory. In a typical sequence the process of going from the initial disk [Fig. 5.9(a)] to the ring trap [Fig. 5.9 (f)] is performed using 50 frames. The frames are switched at a rate of 1 kHz and the displacement of the trap wall from one frame to the next does not exceed 1 μm. This process reliably produces toroidal traps with $N \approx 1.2 \times 10^5$ atoms.

The radial confinement of the toroidal BEC is the result of imaging the surface of the DMD onto the atoms. Figure 5.10(a) shows the region of interest of a DMD frame used to generate a toroidal trap with radius $R \approx 38$ μm, the intensity of the beam in the atom plane is the result of convolving the frame of the DMD with the point spread function (PSF) of the projection path. The diffraction limited PSF of the system is given by the airy function $f_A(\tilde{r}) = 2J_1(\tilde{r})/\tilde{r}$, with J_1 the Bessel function of the first kind and $\tilde{r} = r/(\lambda\,\mathrm{NA})$ where λ is the wavelength of the light and NA the numerical aperture of the system; Fig. 5.10(b) shows in blue a radial cross section of the diffraction limited PSF assuming NA $= 0.25$ and $\lambda = 532$ nm. Additionally, an idealized "smooth" PSF that corresponds to a Gaussian curve with FWHM equal to that of $f_A(\tilde{r})$ is shown in red, this curve is used to understand the blurriness of the projected image without emphasizing the ripples that arise from diffraction due to coherent imaging. Figures 5.10(c)-(e) model the intensity of the light in the plane of the atoms assuming that the DMD is illuminated with a flat top beam[6]; (c) corresponds to the demagnified frame without considering diffraction effects, the

[6]The beam illuminating the DMD is Gaussian, however, the $1/e^2$ radius of the beam (≈ 20 mm) is so large compared to the size of the ring (≈ 1 mm) that we ignore it for the moment and focus only on the effects of diffraction.

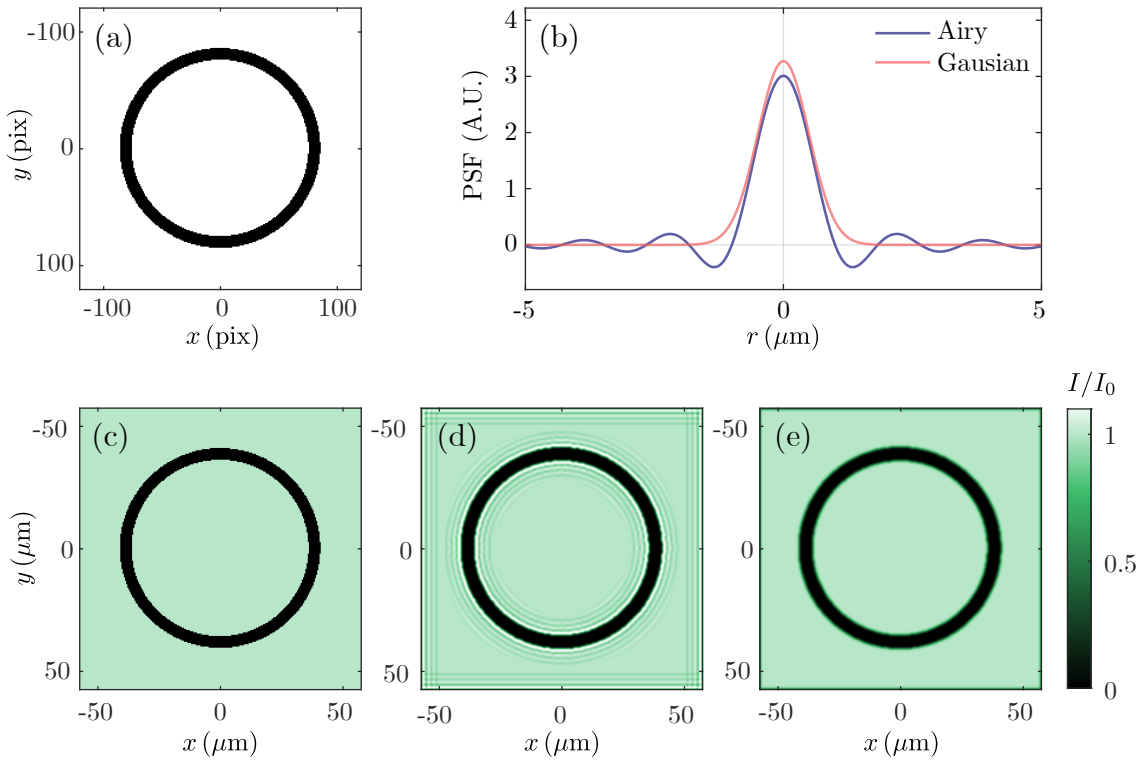

Figure 5.10: Ring trap. The radial confinement of the toroidal condensate is the result of imaging the DMD frame onto the atoms. (a) In this image the DMD frame is a ring with radius $R = 80$ pixels and 10 pixels in width. (b) Idealized point spread function (PSF) for an optical system with NA = 0.25 corresponding to a resolution of 1.3 μm, the blue line corresponds to a diffraction limited system, the red curve is a "smooth" PSF approximated by a gaussian with the same FWHM as the Airy PSF. The square of the function is normalized to unity. The intensity of the light in the plane of the atoms is simulated in (c) assuming no diffraction effects, only the magnification of the system [$1/M = 28.6(4)$] is taken into account, (d) is the convolution of (a) and the airy PSF, (e) is the convolution of (a) and the Gaussian PSF.

magnification of the system is $1/M = 28.6(4)$; (d) is the result of convolving the DMD frame shown in (a) with the Airy PSF, (e) is the convolution of (a) and the Gaussian PSF. The intensity in (c)-(e) is normalized to the intensity at the center of the ring, I_0. Both (d) and (e) are idealized intensities since the PSF is likely to have aberrations, however, both serve to illustrate the result of imaging artifacts,

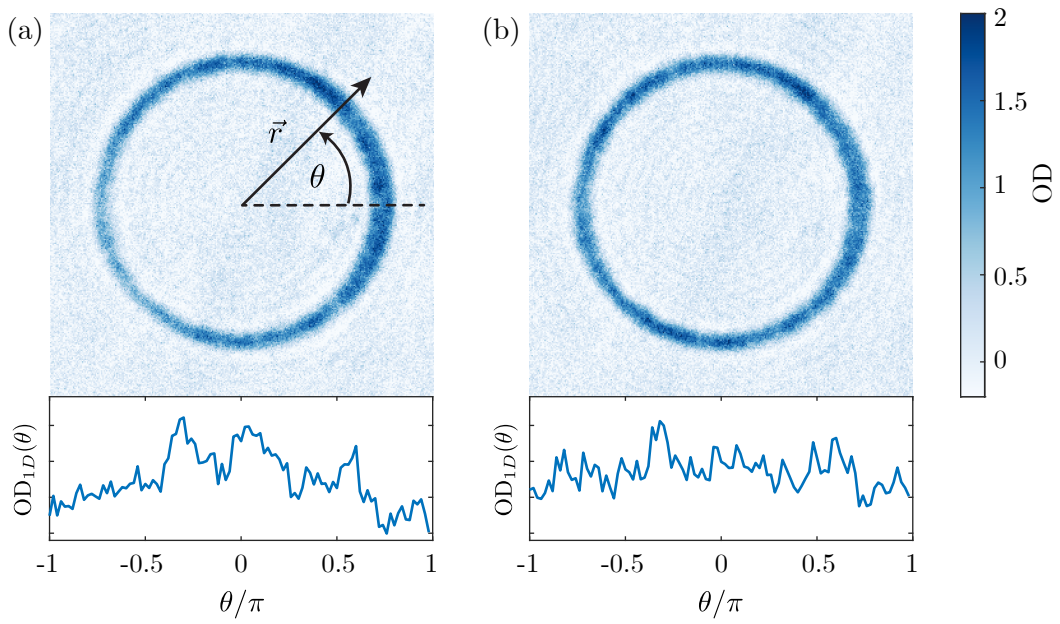

Figure 5.11: Ring azimuthal homogeneity. In-situ images of atoms confined in the toroidal trap and corresponding azimuthal distribution—OD integrated along r—, the images were taken using PTAI. Panels (a) and (b) differ in the focal position of the green-sheet which is the main contribution to density inhomogeneity. The azimuthal $\mathrm{OD}_{1\mathrm{D}}$ is 1.6(5) for (a) and 1.8(2) for (b), the units are arbitrary and scaled equally in both cases.

whereas in (d) we clearly observe the concentric rings that arise from coherent imaging. Panel (e) only shows the blurring effect due to the finite width of the PSF. The case of a more realistic PSF with the main contribution to aberration being spherical aberration would show concentric ring like (d) except the prominence of the ripples would be lesser. Qualitatively, it would look somewhere in between (d) and (e).

The atom density distribution in the toroidal trap is susceptible to inhomogeneities likely the result of optical aberrations of the green-sheet and DMD beams. Based on numerous experimental observations, the green-sheet imperfections are the main cause of inhomogeneous toroidal traps. We minimize some of these imper-

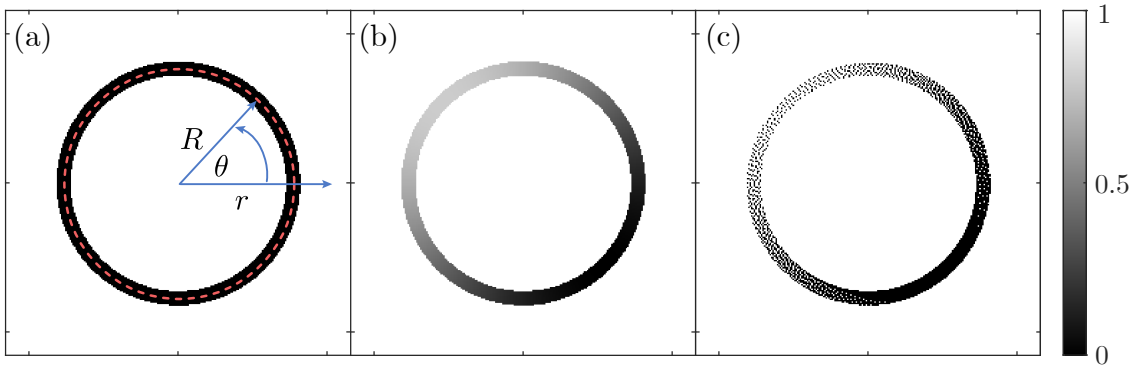

Figure 5.12: DMD Frames to generate azimuthal phonons. White means the DMD mirror is "on" and black means the DMD mirror is "off", only the ROI is shown. (a) DMD frame corresponding to the initial confinement, the ring has a radius of 80 DMD pixels and width of 10 DMD pixels. (b) Grey-scale sinusoidal perturbation with modes $m = 1$. (c) Binary image corresponding to (b) after processing using Jarvis error-diffusion (see text for details).

fections by shifting the focal point of the TEM_{01} beam—this is done by displacing one of the lenses in the optical setup which is mounted on a micrometer translation stage—. Figure 5.11 shows in-situ images of the toroidal BEC, we integrate the optical density (OD) along the radial direction to obtain the azimuthal distribution $\mathrm{OD}_{1\mathrm{D}}(\theta)$. Panel (a) shows a configuration of the green-sheet focus that results in azimuthal density variations of $\approx 30\%$, by shifting the focal point we are able to reduce the variations to $\approx 10\%$ as shown in panel (b).

5.6.1 Generation of Phonon Modes

We excite azimuthal phononic modes in the condensate by applying a repulsive perturbation superimposed on the ring. The ring frame is given by

$$f_{\mathrm{ring}}(\rho) = \begin{cases} 0 & \rho \leq w/2 \\ \\ 1 & \rho \geq w/2 \end{cases}, \tag{5.1}$$

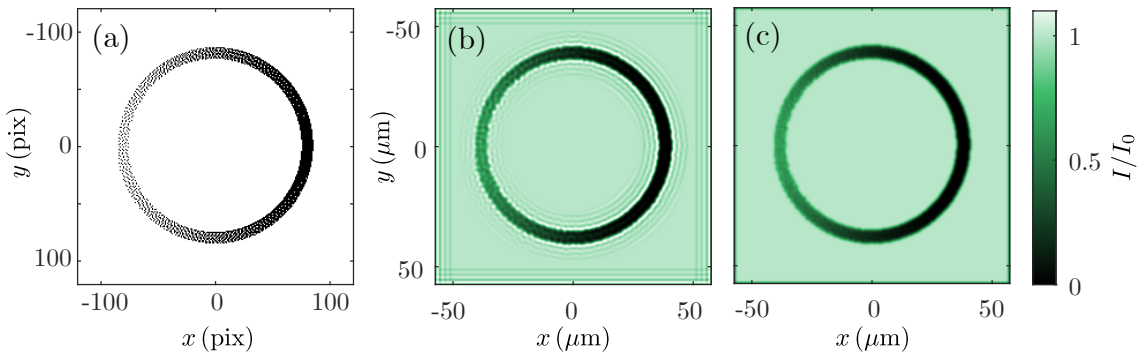

Figure 5.13: Sinusoidal perturbation. (a) DMD Frame with $R = 80$ pixels, $w = 10$ pixels, $m = 1$ and $A = 0.8$. The beam intensity in the atom plane results from the convolution of (a) with the PSF of the system, (b) uses the Airy PSF shown in Fig. 5.10, (c) uses the Gaussian PSF. The intensity is normalized to the intensity I_0 at the center of the ring.

where $\rho = r - R$, R is the radius of the ring, and w the width of the ring. A value of 1 (0) means that the corresponding DMD mirror is in the "on" ("off") position, Fig. 5.12(a) shows the ROI of a frame with $R = 80$ pixels and $w = 10$ pixels. The sinusoidal perturbation with mode m is given by

$$f_m(\rho, \theta) = \begin{cases} A_p \sin(m\theta) & \rho \leq w/2 \\ 1 & \rho \geq w/2 \end{cases}, \tag{5.2}$$

where $A_p \in [0, 1]$ is the amplitude of the perturbation. Figure 5.12(b) shows the grey-scale perturbation for $m = 1$ and $A_p = 0.8$. Since the DMD is a bi-stable device the only alowed values of a mirror are 0 and 1, in order to produce grey-scale images the ideal perturbation shown in (b) is processed using error diffusion to generate a binary image as shown in (c). The technique of error diffusion consists on propagating values from one pixel to the neighboring pixel in order to achieve apparent intermediate values out of a binary pattern; we use the error diffusion

method by Jarvis [76]. Figure 5.13 shows the intensity of the beam in the plane of the atoms resulting from convolving the DMD frame shown in (a) with the PSF of the system, (b) uses an Airy PSF whereas (c) uses a Gaussian PSF. Given the magnification of the system, a DMD mirror side measures ≈ 0.5 μm in the plane of the atoms. Assuming the PSF has a FWHM ≈ 2.5 μm, the convolution of the PSF with the binary frame results in calculating at each pixel position the average of the neighboring pixels within a radius of 2 pixels, effectively producing a smooth transition between the values of 0 and 1.

5.7 Imaging Phonons

A typical sequence to study the evolution of azimuthal phonons in a toroidal condensate follows the procedure described above, after applying the sinusoidal perturbation for 2 ms the BEC is held in the toroid for a variable time t; the BEC is then imaged after a short TOF (≈ 500 μs) using PTAI[7]. Figure 5.14 is a schematic depicting the image processing to extract the density perturbation of the condensate. For each evolution time t_j we average three realizations and calculate the column density of the condensate $n_{2\mathrm{D}}(r, \theta; t_j)$, see panel (a). The background condensate density is calculated by averaging over time

$$n_{2\mathrm{D}}^{(0)}(r, \theta) \approx \langle n_{2D} \rangle = \frac{1}{J} \sum_{j=1}^{J} c_j \, n_{2\mathrm{D}}(r, \theta; t_j), \tag{5.3}$$

[7]Only one PTAI is taken per realization of the BEC.

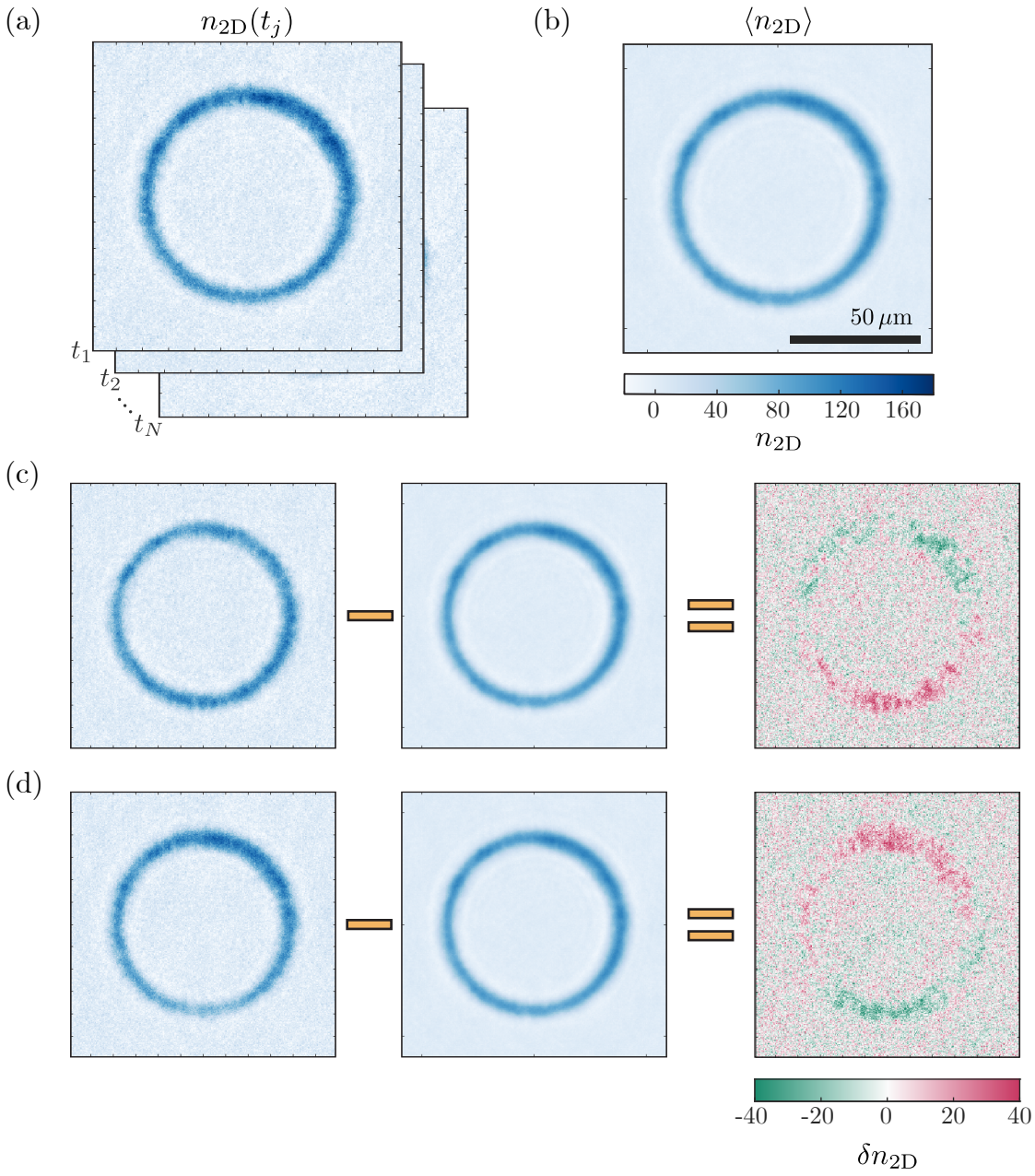

Figure 5.14: Image processing for phonon analysis. (a) Atom density n_{2D} at time t_j averaged over three repetitions. (b) The background condensate density is obtained by averaging n_{2D} over time. (c) and (d) show the density perturbation δn_{2D} calculated by subtracting the background condensate from n_{2D}; (b) and (c) correspond to antinodes in the evolution of the phonon amplitude.

where $c_j = \langle N \rangle / N_j$ is a coefficient that normalizes each realization to the mean atom number in the dataset—typical atom number fluctuations are within 10%—.

In order for this method to properly yield the mean background condensate density the evolution of the phonon must be sampled at least 4 times per period and for enough cycles (on the order of 5) to allow the phonon to fully decay. An alternative method to calculate the background condensate density is to image the toroidal condensate without imprinting a phonon, however, we found that this method created artifacts in the phonon evolution data. A hypothesis to explain the failure of this method is that the condensate is heated by the process of generating a phononic excitation, thus the background condensate when no sinusoidal perturbation is applied differs from the background condensate when the perturbation is applied. The density perturbation is obtained from

$$\delta\tilde{n}_{2\mathrm{D}}(r,\theta;t_j) = \tilde{n}_{2\mathrm{D}}(r,\theta;t_j) - \langle n_{2D}\rangle. \tag{5.4}$$

where the tilde indicates that the quantity has been normalized to constant atom number. The 2D density perturbations are converted to 1D density perturbations by integrating along the radial coordinate (see Fig. 5.15(a))

$$\delta n_{1\mathrm{D}}(\theta,t_j) = \frac{1}{c_j}\int_0^\infty r\,\mathrm{d}r\,\delta\tilde{n}_{2\mathrm{D}}(r,\theta;t_j). \tag{5.5}$$

The quantity $\delta n_{1\mathrm{D}}(\theta,t_j)$ is no longer normalized to constant atom number. Figure 5.15 shows $\delta n_{1\mathrm{D}}(\theta,t_j)$ obtained from sampling the evolution of the phonon 30 times[8] at equal time intervals.

[8]The 30 time samples are obtained from 90 PTAI images since each time sample is the result of averaging over 3 repetitions. The repetition rate of the experimental sequence is ≈ 0.02 Hz, therefore it takes 1.25 hours to produce a plot like Fig.5.15(c).

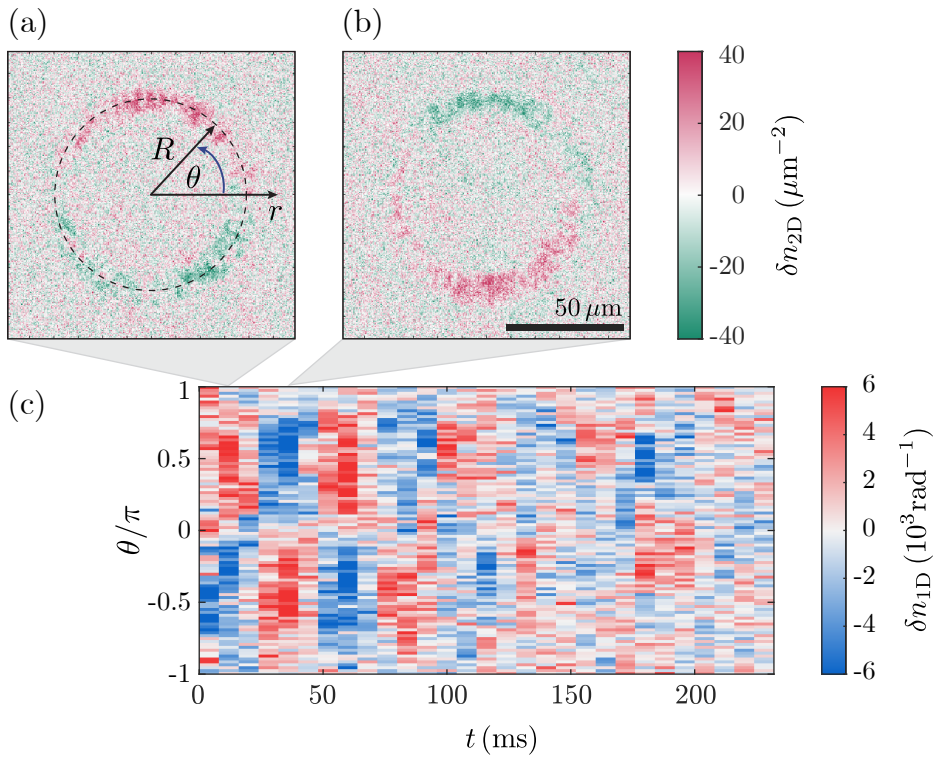

Figure 5.15: Phonon evolution data. (a)-(b) Phonon density perturbation in 2D. (c) 2D plot displaying the 1D phonon density perturbation as a function of azimuthal angle and time. See main text for additional details.

We analyze the phonon evolution by fitting the data to the model

$$\begin{aligned} \delta n_{1\mathrm{D}}^{(m)}(\theta, t) &= A e^{-\gamma t} \sin(\omega_m t - \varphi_0) \sin(m\theta - \theta_0), \\ &= \delta n_m(t) \sin(m\theta - \theta_0), \end{aligned} \tag{5.6}$$

where A is the oscillation amplitude, γ the decay rate, ω_m the frequency and θ_0 and φ_0 are the temporal and azimuthal phases of the phonon. Figure 5.16 shows the data $\delta n_{1\mathrm{D}}(\theta, t_j)$ (top), the fit to the data using the model form Eq. (5.6) (middle) and the fit residual (bottom); (a) and (b) differ by an azimuthal phase rotation of the sinusoidal perturbation by 90 degrees.

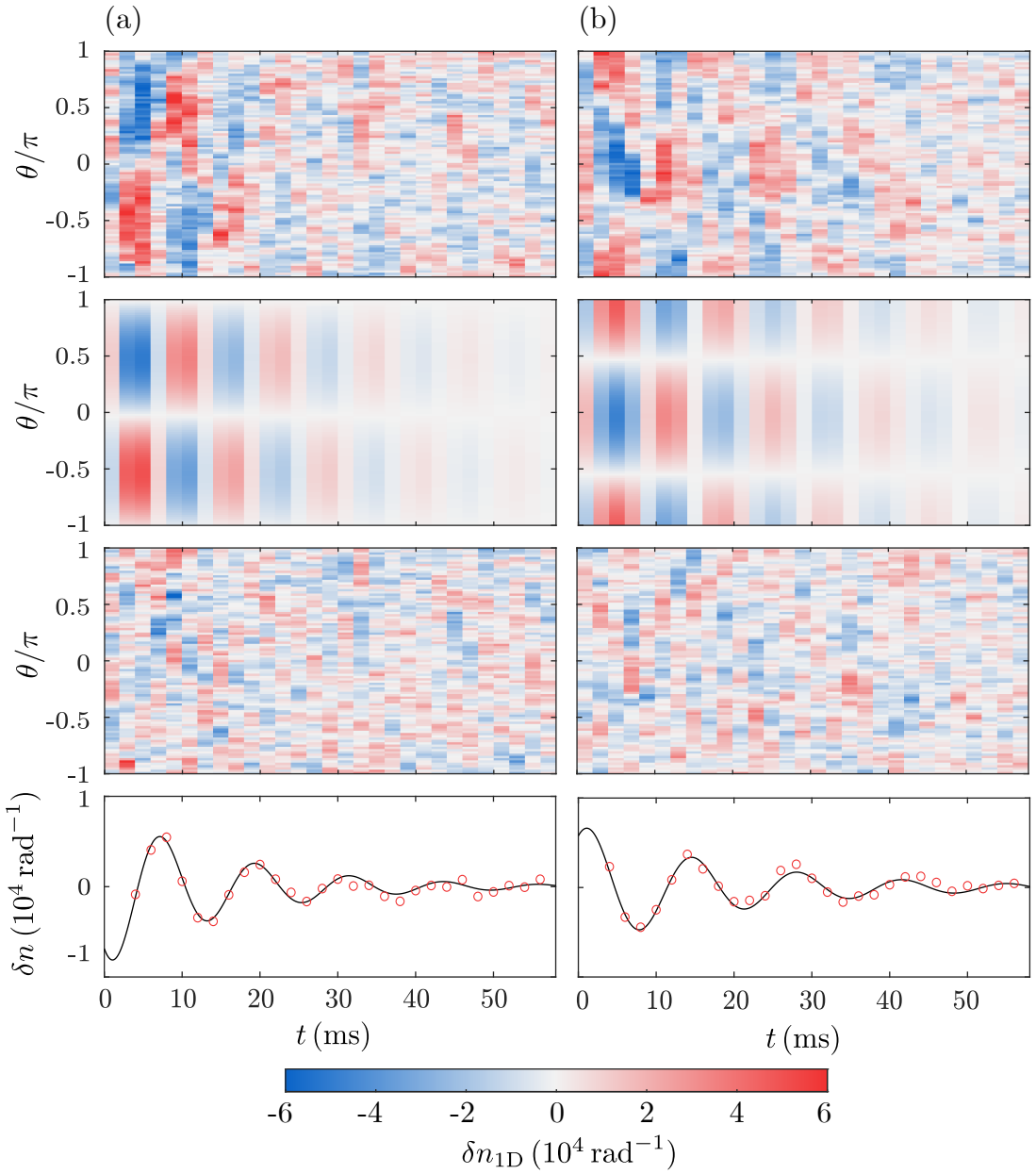

Figure 5.16: Phonon evolution data and fits. Data for m=1 phonons created with $\theta_0 = 0$ in (a) and $\theta_0 = \pi/2$ in (b). The top panels show the data obtained as described in the text, the second row shows the 2D fit to the data, the third row shows the residuals from the fit. The bottom panel shows the phonon amplitude $\delta n(t)$, the symbols are obtained from fitting a time slice of $\delta n_{1D}(\theta, t_j)$ to a sinusoid, the curve is the amplitude found from the 2D fit.

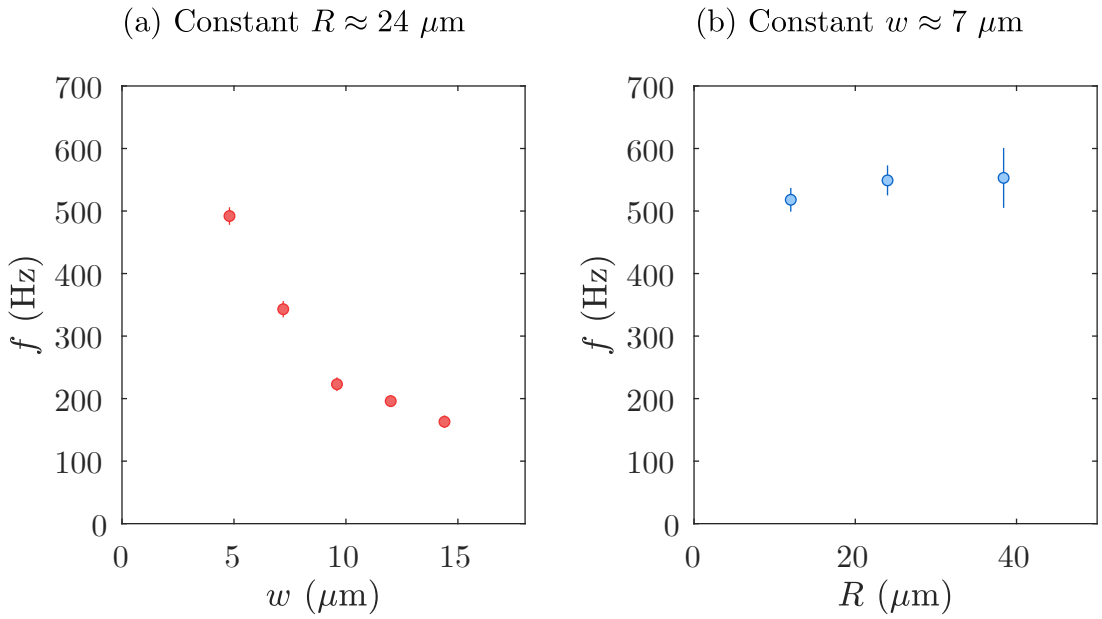

Figure 5.17: Torus radial trapping frequency. (a) Frequency as a function of ring thickness w, the ring radius is kept constant ($R \approx 24$ μm). (b) Frequency as a function of ring radii R, the ring thickness is kept constant ($w \approx 7$ μm). The intensity of the DMD beam differs between (a) and (b).

5.8 Characterization of the Toroidal Trap and Azimuthal Phonons

Here we present relevant characterizations of the toroidal BEC and the azimuthal phonons generated on the BEC. Figure 5.17(a) shows the characterization of the ring trap frequency for rings projected with varying width[9] w, and constant radius R, the power of the beam was also constant; as expected, the radial trap frequency increases as the radial confinement becomes tighter. Figure 5.17(b) shows the characterization of the ring trap frequency for rings projected with varying radius R and constant width w, in addition, the power of the illuminating beam was adjusted to maintain constant intensity in the proximity of the trap (see chapter A.8 for additional details about the DMD illuminating beam).

[9]For reference on coordinates see Fig. 5.12 and Eq. (5.1).

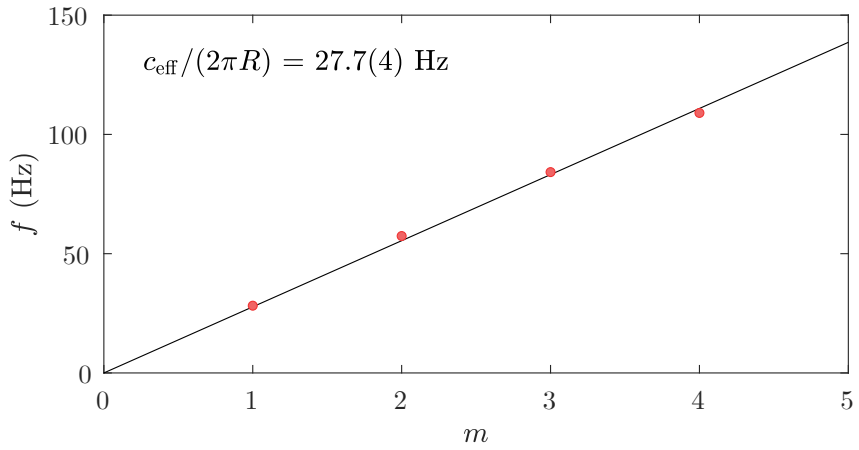

Figure 5.18: Phonon frequency (f) as a function of phonon mode (m). The ring confinement has $R = 19.2(4)$ μm and $w = 4.8(1)$ μm. The linear fit to the frequency yields the effective speed of sound $c_{\text{eff}} = 3.34(8)$ mm/s.

We characterized the phonon frequency as a function of mode number and used the data to estimate the effective speed of sound, $c_{\text{eff}} = (2\pi R)f_m/m = 3.34(8)$mm/s (see Fig 5.18). Additionally, we verified that the quality factor remains roughly constant as a function of mode number (see Fig 5.19). The invariance of Q with m is predicted for Landau damping in a homogeneous gas at temperatures greater than the chemical potential [77].

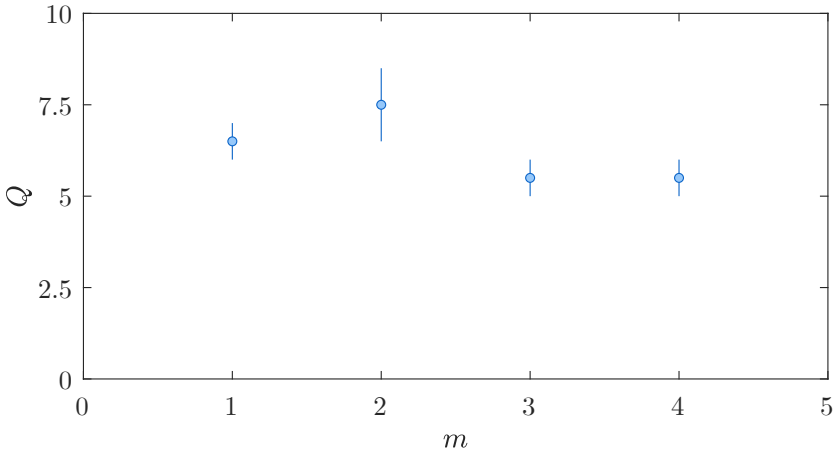

Figure 5.19: Phonon quality factor (Q) as a function of phonon mode (m). The ring confinement has $R = 19.2(4)$ μm and $w = 4.8(1)$ μm.

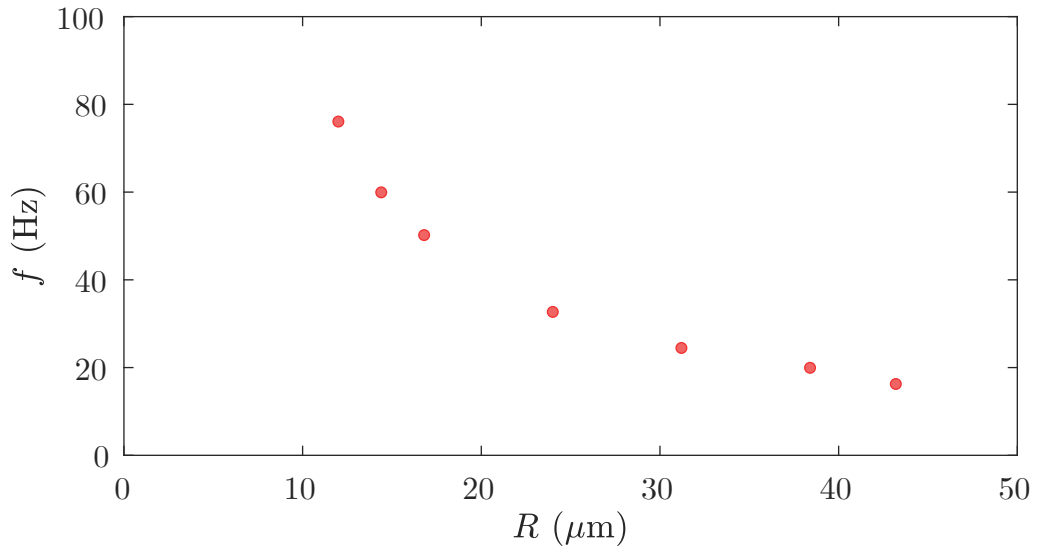

Figure 5.20: Phonon frequency (f) as a function of ring radius (R) for mode $m = 1$. The ring confinement has $w = 4.8(1)$ μm, the atom number in the toroidal trap is $N \approx 10^5$. The uncertainty is smaller than the size of the circles.

Finally, we characterized the frequency (see Fig. 5.20) and quality factor (see Fig. 5.21) of $m = 1$ phonons in rings with constant w and varying radius. The power of the DMD was adjusted to roughly maintain the same trap depth for all radii.

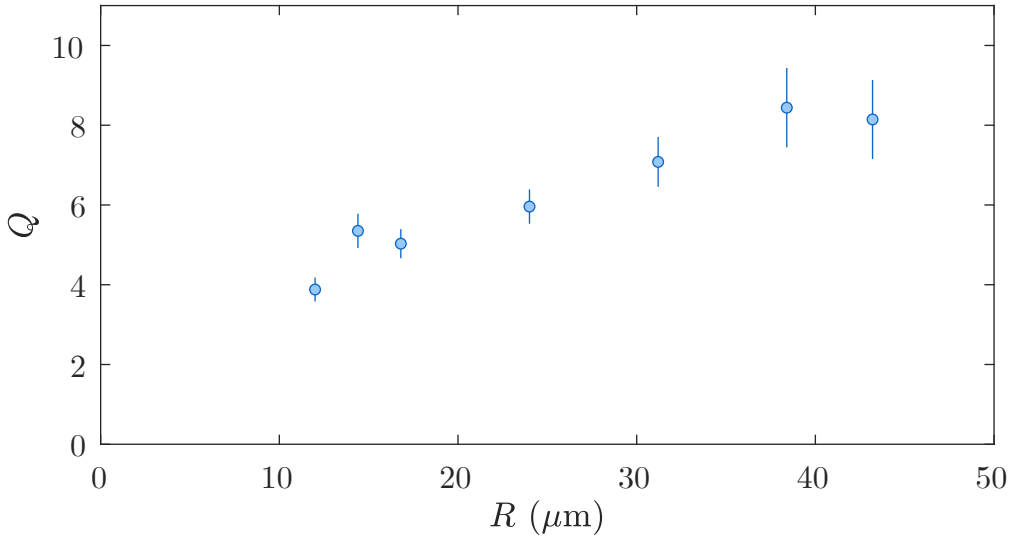

Figure 5.21: Phonon quality factor (Q) as a function of ring radius (R). The ring confinement has $w = 4.8(1)$ μm, the atom number in the toroidal trap is $N \approx 10^5$.

We observed an unexpected linear dependance of the quality factor with the ring radius, we think that this is the result of increased atomic density in the smaller rings which leads to non-linear damping effects [78].

We have reviewed in this chapter all the elements of the experimental sequence that set the stage to study Hubble amplification (attenuation) of phonons in a contracting (expanding) toroidal condensate, which will be the focus of the next chapter.

Chapter 6: Hubble Friction Experiment

Phonons in BECs are scalar fields that evolve approximately according to an effective spacetime metric defined by the background condensate [20]. For toroidally-shaped BECs, expanding or contracting 1D universes [22] can be simulated by dynamically changing the BEC's radius and observing the evolution of azimuthal phonons. Unlike the expansion observed in the photon-dominated epoch of the universe, we explore non-adiabatic expansions and contractions where the rate of the metric change exceeds the oscillation frequency. In this chapter we present the experimental results of expanding or contracting toroidal BECs. An edited version of the submitted ArXiv manuscript [79] is presented in section 6.2. I contributed with the design and characterization of the DMD optics and the imaging optics, as well as with the modeling of the system presented in section 6.1. Swarnav Banik and I collectively acquired all the experimental data presented in section 6.2. The analysis of the data was performed by Swarnav. All authors discussed the results and contributed to the writing and editing of the manuscript.

6.1 Experimental Parameters

In this chapter when the discussion applies indiscriminately to both the ring expansion and the ring contraction, we will refer to them in the general form *the ring dynamics*; when needed, the specific case will be noted.

The ring radius is varied from an initial radius R_i to a final radius R_f according to the function

$$R(t) = \begin{cases} R_i & \text{if } x \leq -5/2, \\ R_i + \frac{1}{2}(R_f - R_i)\left\{1 + \text{erf}[x(t)]\right\} & \text{if } |x| < 5/2, \\ R_f & \text{if } x \geq 5/2, \end{cases} \tag{6.1}$$

where $x(t) = (t - t_0)/\beta$, t_0 is the time at which $\left|\dot{R}(t)\right|$ is maximized and β is a parameter that determines how fast the ring radius is varied. The factor 5/2 was chosen to minimize the discontinuity of $R(t)$ and $\dot{R}(t)$ when switching from the stationary radius R_i and to the stationary radius R_f. The rate of change of the radius is given by

$$\dot{R}(t) = \frac{R_f - R_i}{\sqrt{\pi}\beta} \exp\left[-x(t)^2\right], \tag{6.2}$$

for $|x| < 5/2$, and it is zero at any other time. The total time during which the ring radius is varied is $t_x = 5\beta$ and the 10 %-90 % rise time is 1.8β.

The term in Eq. (2.43) analogous to the Hubble friction term in cosmology [44] is $f_\alpha = \alpha(\dot{R}/R)\partial_t\chi$. The strength of this non-dissipative friction term[1] depends on

[1] As discussed in Chapter 2.3 this term acts as a friction term when the ring is expanded,

the parameter α, the initial (R_i) and final (R_f) radii of the trap as well as the rate of change of the trap radius which is parametrized by β, and the amplitude of $\partial_t\chi$—which is proportional to the amplitude of the phonon perturbation ($\delta n(t)$)—during the ring dynamics. Consequently, the strength of f_α can be experimentally tuned by varying the values of R_i, R_f and β. In addition to these values, we can effectively tune the amplitude of $\partial_t\chi$ by delaying the onset of the ring dynamics with respect to the phase of the initial phonon oscillation.

We simulated the solution to the differential equation governing the evolution of χ, Eq. (2.43), in order to understand the response of the system to some of the experimentally tunable parameters. Let us introduce two variables to simplify the description of the analysis; the first one is the time at which the radius stops changing, t_f, defined through $R(t \geq t_f) = R_f$ and the second one is the time at which the value of $\left|\dot{R}/R\right|$ is maximized, t_{peak}. We fit $\partial_t\chi$ at $t \geq t_f$ to $A\exp(-\gamma_f\, t)\sin(\omega_f t + \varphi_f)$, and extract the value of the envelope amplitude (A) for two cases: one with $\alpha = 0$ which returns the envelope amplitude A_0, and one with $\alpha \neq 0$ from which we obtain the envelope amplitude A_α.

Figures 6.1 and 6.2 show the evolution of $\partial_t\chi$ in the case of a contracting ring and an expanding ring, respectively. We have chosen to plot $\partial_t\chi$ for simplicity, understanding that it is related to the amplitude of the phonon through $\delta n(t) = \partial_t\chi(t)/(R_f)^\alpha$. The non-zero value of alpha was chosen as $\alpha = 1/2$ since it is the smallest value expected for our system[2] and larger values of α will result in an

damping the phonon amplitude; however, if the ring is contracted the term amplifies the phonon amplitude.

[2]Assuming that the trapping potential along z and ρ are harmonic.

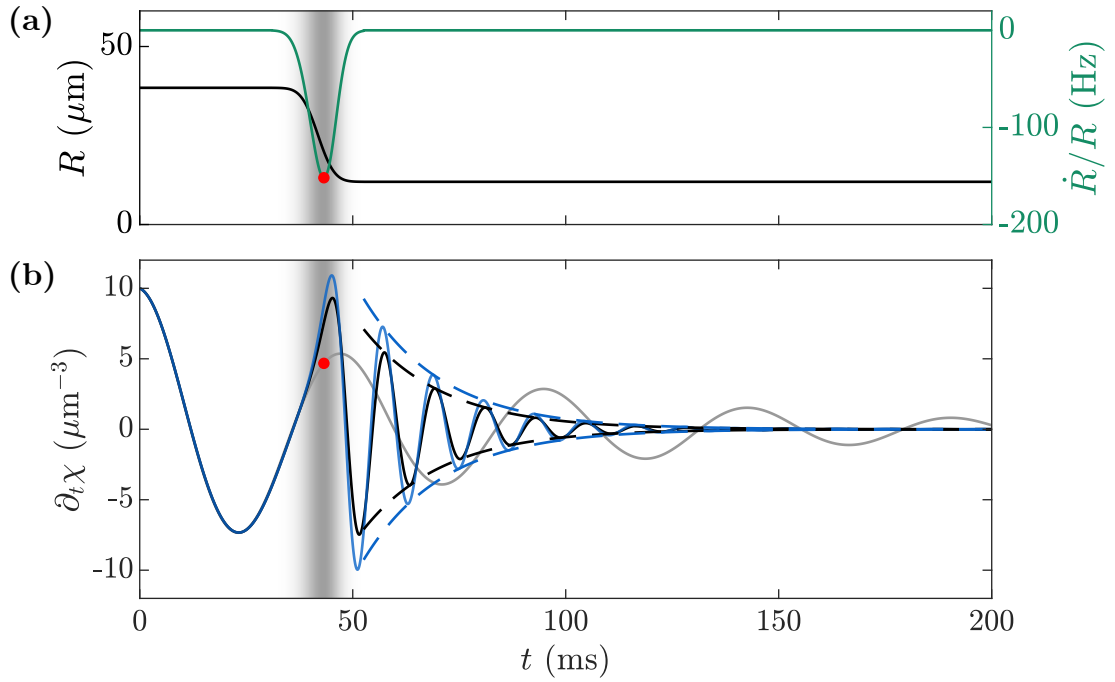

Figure 6.1: Time evolution of $\partial_t\chi$ in a contracting ring. (a) Ring radius (R) as a function of time (black) and value of $\dot{R}/R$ (green). (b) Evolution of $\partial_t\chi$ as a function of time, the gray curve follows the evolution of the initial amplitude in the absence of contraction, the solid black (blue) curve is the solution to the ODE for $\alpha = 0$ ($\alpha = 0.5$) and the dashed black (blue) curves are the envelope fit to the solid black (blue) curve after contraction.

increase on the strength of f_α. The figure of merit in our analysis is the contrast defined by

$$S_\alpha = \left|1 - \frac{A_\alpha}{A_0}\right|. \tag{6.3}$$

The minimum contrast, $S_\alpha = 0$, means that after contraction or after expansion the phonon amplitude when $\alpha \neq 0$ is indistinguishable from the phonon amplitude when $\alpha = 0$. In the case of a ring expansion the contrast's upper limit is one since, in principle, the phonon amplitude can be fully attenuated ($A_\alpha \to 0 \Rightarrow S_\alpha \to 1$). However, in the case of a ring contraction the contrast can be larger than one, since the phonon amplitude can be amplified such that $A_\alpha \gg A_0$ ($A_\alpha > 2A_0 \Rightarrow S_\alpha > 1$).

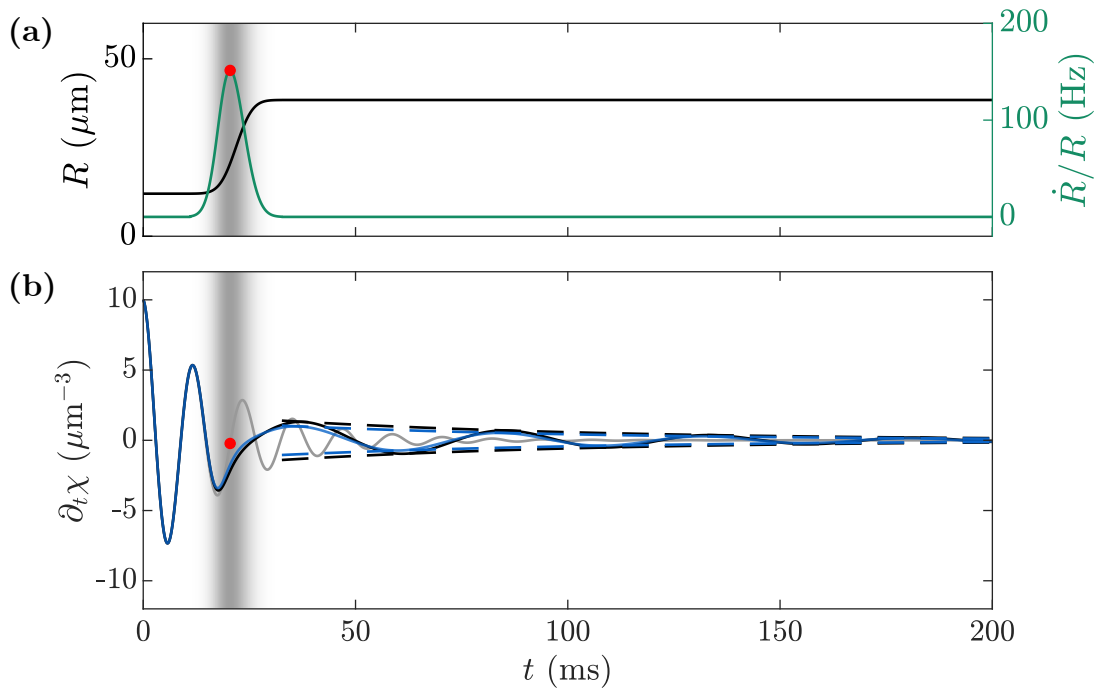

Figure 6.2: Time evolution of $\partial_t\chi$ in an expanding ring. (a) Ring radius (R) as a function of time (black) and value of $\dot{R}/R$ (green). (b) Evolution of $\partial_t\chi$ as a function of time, the gray curve follows the evolution of the initial amplitude in the absence of expansion, the solid black (blue) curve is the solution to the ODE for $\alpha = 0$ ($\alpha = 0.5$) and the dashed black (blue) curves are the envelope fit to the solid black (blue) curve after expansion.

For our experiments we looked for a combination of experimental parameters that could be realized in our setup and that would maximize the contrast S_α. The analysis was performed for the particular value of $\alpha = 0.5$ since this is the smallest (theoretical) value that the parameter can take, a larger value of α will result in an overall increase in contrast in the form of a multiplicative factor.

Figure 6.3 shows the result of the contrast analysis for varying ring radii, in both cases the minimum radius is $R = 12$ μm and the maximum radius is $R = 40$ μm and the value of β was chosen as a fraction of the initial oscillation period ($T_i = 2\pi/\omega_i$), $\beta = T_i/5$. In both the contraction (a) and the expansion (b) cases

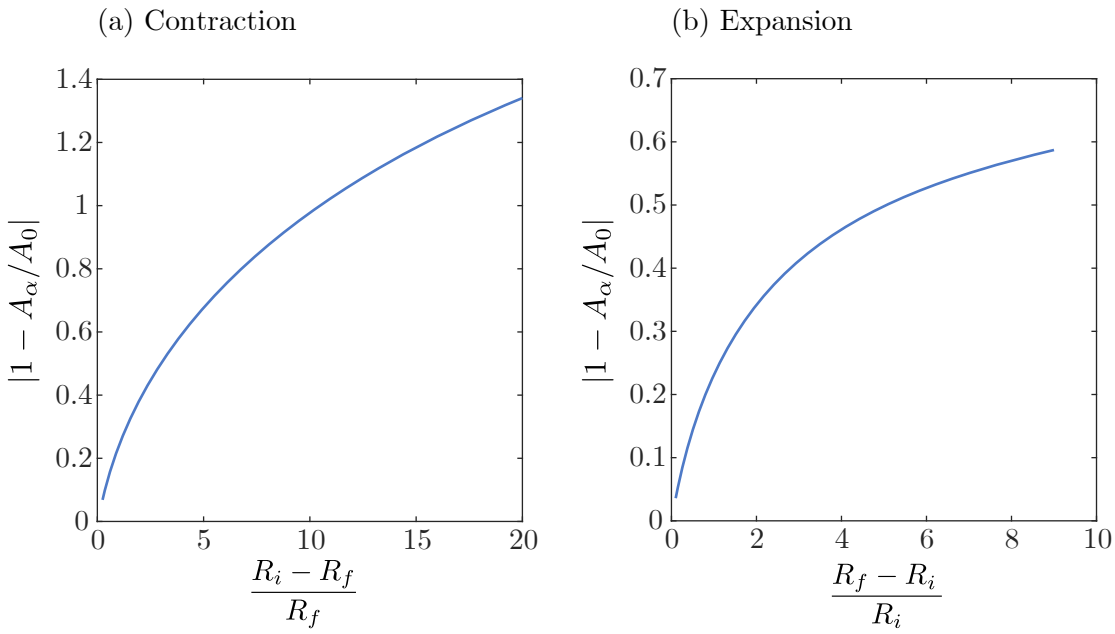

Figure 6.3: Contrast as a function of the initial and final ring radii.

the contrast increases as the difference between the initial and final radii increases. We note that, experimentally, there are limitations on both ends of the realizable ring size; for $R \gtrapprox 40$ μm the density distribution becomes discontinuous and for $R \lessapprox 12$ μm detection of the phonon amplitude is unreliable. The latter is the result of an increase in the atom density that leads to an increase in the optical density (OD) of the cloud[3]; a potential work around is to perform PTAI on an even smaller fraction of the population. However, the signal to noise ratio of the images decreases as the population transfer fraction is reduced.

Understanding the effect of delaying the onset of the contraction or expansion is more subtle than understanding the effect of changing the initial and final radii. We define the variable φ_p as the phase of the initial phonon at time t_{peak}—the time that maximizes $\left|\dot{R}/R\right|$—, we simultaneously vary φ_p by delaying the onset of the

[3]We empirically determined that the range of ODs that allow us to reliably detect atomic density variations is in the order of one.

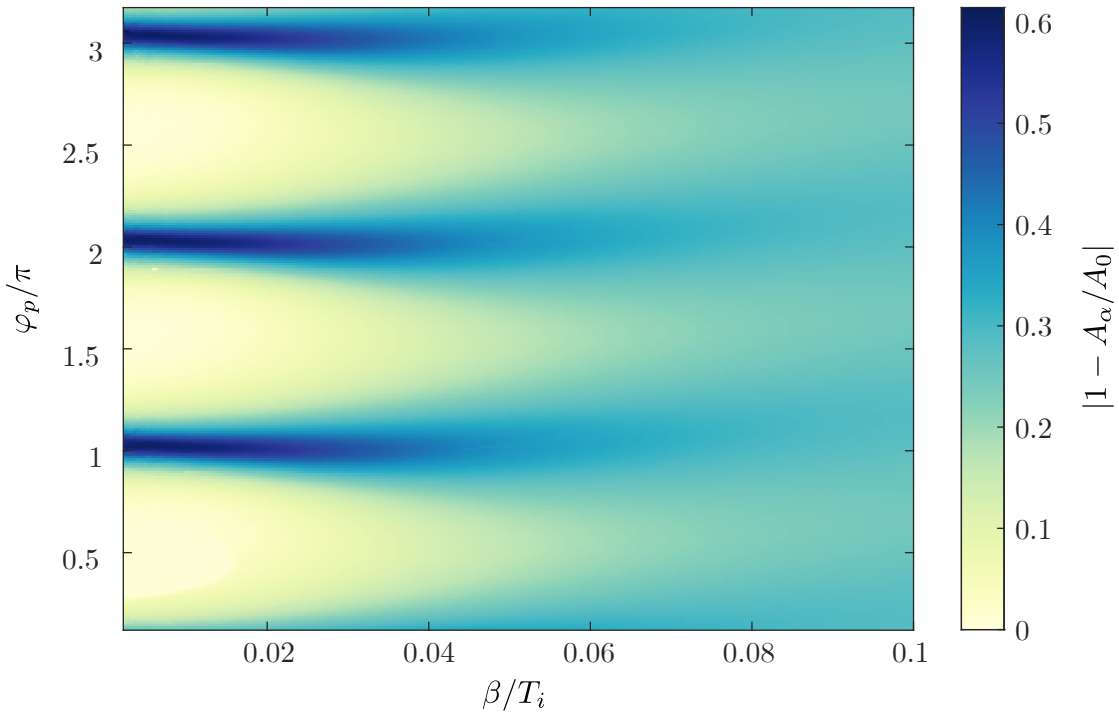

Figure 6.4: Contrast as a function of β and φ_p for a ring contraction going from $R_i = 40$ μm to $R_f = 12$ μm.

contraction (or expansion) and the parameter β. Figure 6.4 shows the result of this analysis for the case of a ring contraction while Fig. 6.5 shows the analysis for the case of a ring expansion, in both cases the contrast is plotted as a function of φ_p/π and β/T_i, where $T_i = 2\pi/\omega_i$ is the period of an oscillation in the initial ring confinement. The contrast has a periodic behavior as a function of φ_p/π, this contrast is larger for small values of β/T_i, as β increases the periodic contrast vanishes. Recalling that the Hubble attenuation or amplification corresponds to the term $f_\alpha = \alpha(\dot{R}/R)\partial_t\chi$ in Eq. (2.43), we see that for small values of β (fast, non-adiabatic process) the ring radius changes in a fraction of the phonon oscillation period, consequently the instantaneous amplitude of the phonon—which is proportional to $\partial_t\chi$—strongly determines the strength of f_α. On the other hand, for large values of β (slow,

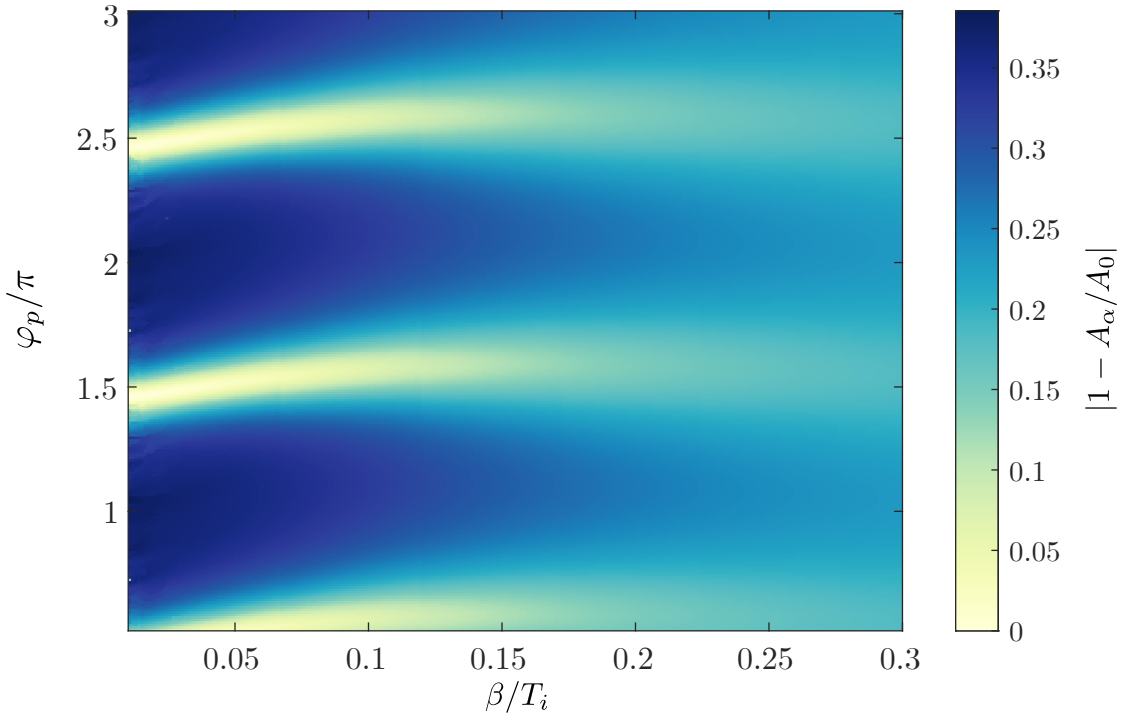

Figure 6.5: Contrast as a function of β and φ_p for a ring expansion going from $R_i = 12$ μm to $R_f = 40$ μm.

adiabatic process) the term f_α affects the evolution of the phonon over multiple oscillations, thus the effect of the instantaneous amplitude of the phonon is averaged out.

We chose to work with rings with $R_i \approx 38$ μm and $R_f \approx 12$ μm in the case of ring contractions and the initial and final radii were reversed in the case of ring expansions. The ring width that best worked was $w \approx 5$ μm in experimental trials [4]. We explored, experimentally, the values of β for which we observe phonon oscillations after the ring is contracted or expanded. Given the chosen ring size, the minimum value of β that allows us to reliably detect phonon oscillations after dynamics was $\beta = 2$ ms.

[4]The ring trap was projected with the DMD using frames with $R_i = 80$ pix and $R_f = 25$ pix, while the width of the ring was $w = 10$ pix. We recall that a DMD mirror is projected in the plane of the atoms to a feature measuring $l \approx 0.48$ μm by side.

6.2 Experimental Results

The experiment begins with the quasi-2D BEC described in Chapter 5, the typical atom number in the toroidal trap is $N \approx 1 \times 10^5$ and the chemical potential is $\mu \approx h \times 2.7$ kHz. The frequency of the harmonic vertical confinement is $\omega_z/2\pi \approx 1.2$ kHz while the dipole mode of the radial trap—assuming it is harmonic to first approximation— has frequency $\omega_r/2\pi \approx 500$ Hz. Based on the considerations discussed in section 6.1 we create toroidal traps with radius R ranging from 12 μm to 38 μm and radial width 5 μm. We generate an azimuthal phonon excitation with mode number $m = 1$ as described in section 5.6.1, the perturbation amplitude is set to 0.8 times the overall potential depth and is applied for 2 ms. After imprinting, the phonon evolves for an initial time t_i from 5 ms to 70 ms, at which point the torus is expanded or contracted using the error function profile given by Eq. (6.1) with $\beta = 2$ ms—which corresponds to a 10 %-90 % rise time of 3.6 ms—, and continues to evolve for up to $\approx$ 150 ms. For expansion, the initial and final radii are $R_\mathrm{i} = 11.9(2)$ μm and $R_\mathrm{f} = 38.4(6)$ μm; these are reversed for contraction. We detect the phonon at various points during the complete evolution using partial transfer absorption imaging (see chapter 3.6.1) after a short 500 μs time of flight. We fit the 2D density $n_\mathrm{2D}(r, \theta)$ from which we obtain the one dimensional phonon density perturbation δn_1D, see section 5.7 for additional details.

In our system, the phenomenological damping (γ) is observed to depend on radius, and we parameterize γ in terms of the quality factor $Q = \omega/2\gamma = c_\theta/2R\gamma$, which eliminates most of the radial dependence present in γ, see Refs. [77] and [80].

Because the 3.6 ms expansion or contraction is a small fraction of the phonon oscillation period, the overall fit is insensitive to how Q interpolates between Q_i and Q_f; thus, we assume a simple linear dependence of Q on R. As shown in Fig. 6.6, our data typically has less than one oscillation before R changes; to reduce the uncertainty in Q_i and $\omega(R_\mathrm{i})$, we include in the simultaneous fit 7 datasets corresponding to the phonon evolution in stationary rings with radii in the range of the expansion or contraction. These fits include as free parameters γ_H, Q_i, Q_f, α as well as the initial amplitude δn_i, temporal phase φ_0, and speed of sound $c_{\theta,\mathrm{i}}$. We assume that, to first order, the effective speed of sound follows the scaling derived from the theoretical model $c_\theta(t) = c_{\theta,\mathrm{i}}\ (R(t)/R_\mathrm{i})^{-\alpha/2}$.

Figure 6.6 shows a number of experimental data-sets for the case of expansion (a) and contraction (b). The solid curve is the time-dependent density perturbation δn obtained from the full simultaneous fit, while the circles plot δn from independent fits to $\delta n \sin(\theta)$ at each sampled time (see section 5.7 for additional details). The gray bar encodes the value of $\left|\dot{R}/R\right|$, with the darkest grey value corresponding to the maximum value, occurring at t_peak, $\dot{R}/R \approx 1.53 \times \omega$.

We study the hypothesized impact of the phonon phase on the Hubble friction strength during expansion and contraction by changing t_i, thereby phase-shifting the phonon by $(c_{\theta,\mathrm{i}}/R_\mathrm{i})t_\mathrm{i}$. The phase of the phonon at t_peak is $\varphi_\mathrm{peak} \equiv \int_0^{t_\mathrm{peak}} dt\ \omega(t) + \varphi_0$. Figure 6.6 shows of the time-traces with multiple t_i for both expansion and contraction, providing a complete picture to investigate the strength of Hubble friction.

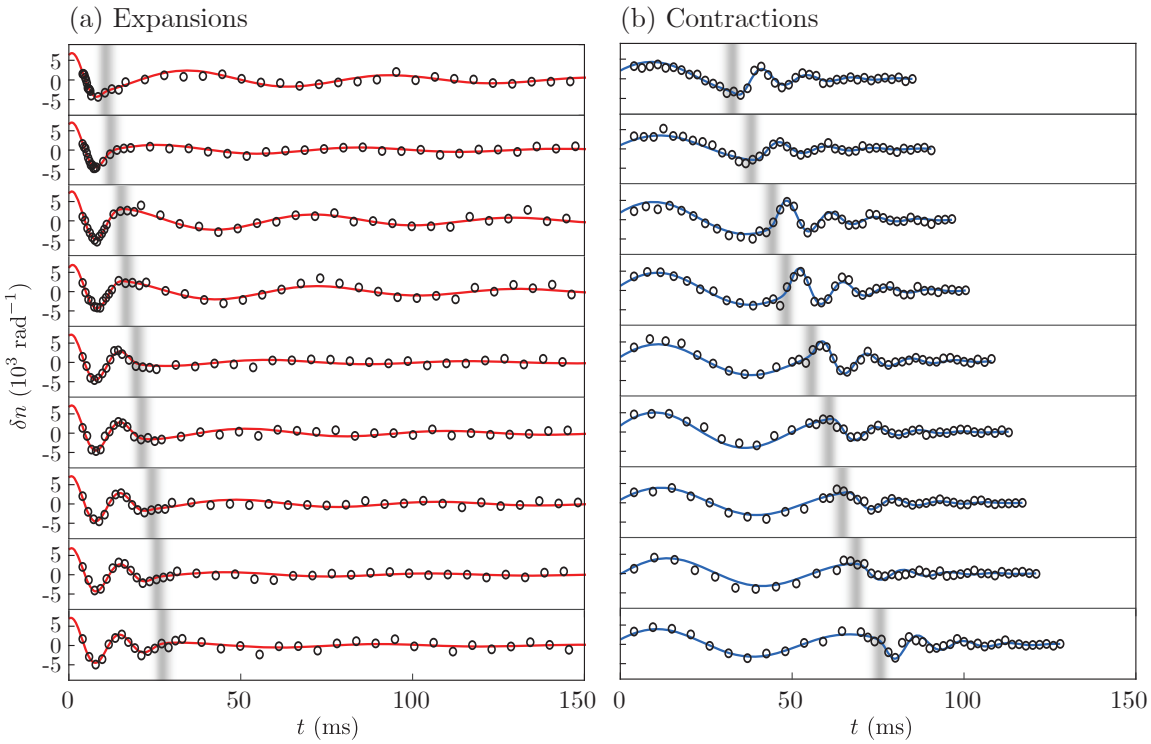

Figure 6.6: Phonon amplitude δn as a function of time t for (a) expanding and (b) contracting tori. The grey bars encode the value of $\left|\dot{R}/R\right|$. The symbols are obtained from fitting a sinusoid to each time-slice of δn_{1D} The expansion data (a) used $R_{\mathrm{i}} = 11.9(2)$ μm and $R_{\mathrm{f}} = 38.4(6)$ μm, and vice versa for contraction (b), here $\beta = 2$ ms. t_{i} is varied from 6.5 ms to 23 ms for expansion and from 27 ms to 70 ms for contraction. The red (blue) curves show the phonon amplitude obtained from a simultaneous fit to the expansion (contraction) dataset, as discussed in the text.

The model used to fit the data consists on the equation of motion

$$\frac{\partial^2}{\partial t^2}\chi + \left[2\gamma_m(t) + \gamma_H \frac{\dot{R}(t)}{R(t)}\right]\frac{\partial}{\partial t}\chi + \left[\frac{mc_\theta(t)}{R(t)}\right]^2 \chi = 0, \tag{6.4}$$

which is Eq. (2.43) with the explicit instance of α replaced by γ_H, this was done in order to not assume, a priori, that the theoretical prediction $\gamma_H = \alpha$ was correct. Nonetheless, we assume that all other quantities scale with α as described by the theoretical model in the thin ring regime [44]. The red curves in Fig. 6.6(a) show the results of a global fit of Eq. (6.4) to the full expansion dataset comprising 11

expansion traces and 7 stationary-ring traces, the blue curves in Fig. 6.6(b) show the results of a global fit of Eq. (6.4) to the full contraction dataset comprising 17 contraction traces and the aforementioned 7 stationary-ring traces. The black circles in both cases represent the instantaneous amplitude obtained from fitting a time slice of $\delta n_{1\mathrm{D}}(\theta, t)$ to an azimuthal sinusoid.

The parameters γ_{H}, α, Q_{i}, Q_{f}, $c_{\theta,\mathrm{i}}$ and δn_{i} are global, i.e., they are shared across all time traces. For each time trace, δn_{i} is scaled by the atom number $N(t)$ for that trace, and $c_{\theta,\mathrm{i}}$ is correspondingly scaled by [5] $\propto N(t)^{\alpha/2}$; this accounts for both atom loss during and after expansion or contraction and for overall drifts in atom number during data acquisition. Each global fit includes 7 additional time-traces, each with constant R, roughly from R_{i} to R_{f}. Because $c_\theta(R) \propto R^{\alpha/2}$ in stationary rings, these additional datasets further constrain α. We performed separate global fits for expansion and contraction data, giving an independent measure of their Hubble friction coefficients. Finally, we perform these global fits in eight different ways, with the number of fit parameters varying between 32 and 117. Each fit yields different best-fit values, but generally they agree within 2-σ. These fitting methods differ on whether the temporal and azimuthal phases are shared across the time traces and if atom number varies within each time trace. Due to the large number of data points, the degrees of freedom, in excess of 1×10^4, do not vary significantly between the different methods. We take the mean of the values obtained from the eight methods as the best fit value. Their standard deviation is added in quadrature to the average 1-σ uncertainty from the fit to obtain the final uncertainty in the measurement.

[5] This can be derived from Eq.(4.8) and Eq.(4.20) in reference [44].

	α	$\gamma_{\rm H}$	$Q_{\rm i}$	$Q_{\rm f}$	$c_{\theta,{\rm i}}$	$\delta n_{\rm i}$
Expansion	0.47(1)	0.28(4)	3.5(1)	4.4(2)	5.42(2)	7.47(13)
Contraction	0.52(3)	0.36(3)	7.8(3)	3.5(1)	4.36(4)	4.50(5)

Table 6.1: Best fit global parameters.

Table 6.1 lists the best-fit values, with $\gamma_{\rm H}$ different for contraction and expansion. The values of α are in agreement with each other and are about 1/2. For our power-law potential model [44], α ranges from 1/2 (for a harmonic potential) to 1 (for a hard-wall potential). Our average value of $\alpha \approx 0.495$ suggests that we have a harmonic potential in both z and r. The discrepancy between the values obtained for α and those for γ_H further indicates a departure from the thin-ring model assumed in the fitting process.

Lastly, we confirm our expectation that the phonon phase $\varphi_{\rm peak}$ has a marked impact on the amplitude following expansion or contraction in the non-adiabatic limit. Our experiments probe $1.3 \lesssim \varphi_{\rm peak}/\pi \lesssim 2.9$. Fig. 6.7(a) illustrates our process for obtaining the final amplitudes $A_{\rm f}$ where we fit the oscillatory behavior to an exponentially decaying sinusoid with the amplitude and temporal phase as free parameters (the remaining parameters are drawn from the global fits). By contrast, the initial amplitude $A_{\rm i}$ is obtained from our global fit, from the envelope of the decaying sinusoid evaluated at $t_{\rm peak}$. Figure 6.7(b) plots the fractional change in amplitude $A_{\rm f}/A_{\rm i}$ versus $\varphi_{\rm peak}$ with blue circles, and the solid blue curve depicts $A_{\rm f}$ obtained from our global fits [6]. Our simulations (black and grey curves) show that the significant oscillations for $\gamma_{\rm H} = 0$, give way to more uniform gain with increasing

[6]The phenomenological damping term in Eq. (6.4) leads both $A_{\rm i}$ and $A_{\rm f}$ to decrease in a common-mode manner with increasing $\varphi_{\rm peak}$, but that decrease is absent in the ratio $A_{\rm f}/A_{\rm i}$.

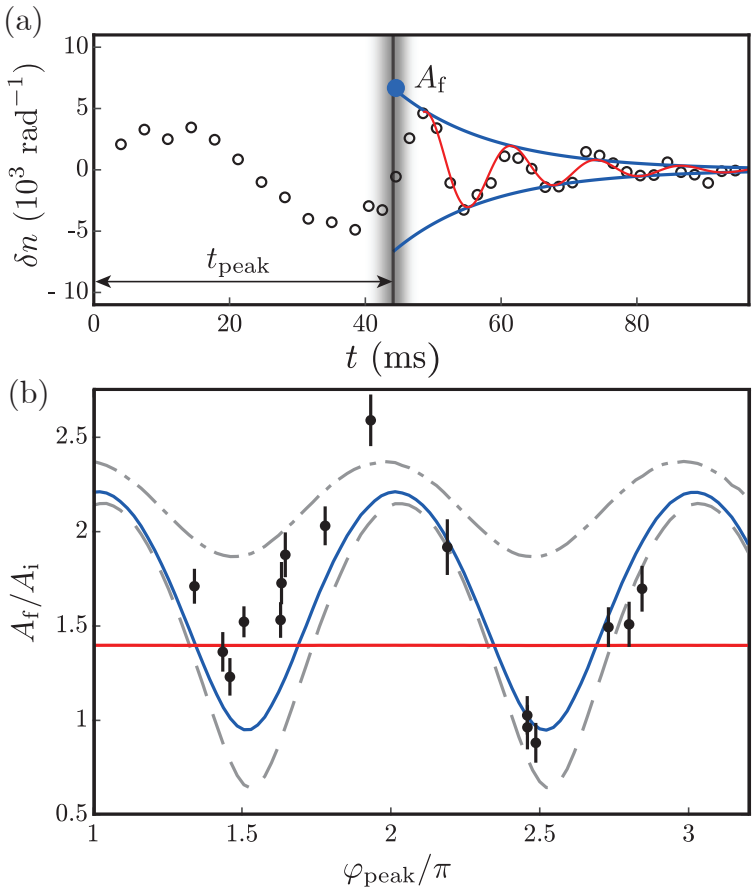

Figure 6.7: Phonon amplitude vs. phase. (a) Data (black circles), fit (red curve), and oscillation envelope (blue curve) used to extract the amplitude A_f at t_peak. The grayscale bar encodes the value of $|\dot{R}/R|$, with a maximum of 328(11) s^{-1} at t_peak. (b) Ratio of amplitudes $A_\mathrm{f}/A_\mathrm{i}$ vs. φ_peak, the oscillation's phase at t_peak. The black circles plot the data. The gray dashed, blue solid, and gray dashed-dot curves show the prediction of Eq. (6.4) for $\gamma_H = 0$, 0.36, and 1, respectively, with $\alpha = 0.52$. The red line indicates the prediction for an adiabatic contraction.

γ_H. The measured values of $A_\mathrm{f}/A_\mathrm{i}$ are generally larger than would be expected for $\gamma_\mathrm{H} = 0$, showing Hubble amplification due to contraction. Unlike Ref. [22], which probed $1.8 \lesssim \varphi_\mathrm{peak}/\pi \lesssim 2.1$, where $A_\mathrm{f}/A_\mathrm{i}$ has little dependence on Hubble friction, our greater range of φ_peak allows us to better constrain γ_H.

The observed oscillatory dependence of A_f on φ_peak results from the rapid non-adiabatic, i.e. superluminal, contraction in this experiment. The solid red

curve emphasizes this point by plotting the simulated behavior for a slow adiabatic contraction, computed with $\gamma = 0$. No dependence on φ_{peak} is present in this limit, as the phonon would undergo many oscillations during expansion and therefore lose any dependence on initial phase. The deviation from the adiabatic curve is associated with "classical" stimulated emission or absorption into or out of the phonon field, in much the same way that these processes have been observed in acoustic black holes [16]. Direct observation of spontaneous processes, i.e. pair production [81], would require an increase in our detection threshold. While here we averaged three images per time point, the observation of spontaneous Hawking radiation in Ref. [18] required a $\approx 10^4$ image dataset.

Our data qualitatively agrees with the theoretical predictions [44, 82], we do observe phonon red- (blue-) shifting as well as attenuation (amplification) in the case of ring expansion (contraction), as well as a periodic modulation of the amplitude after contraction. However, the numerical values obtained from fitting our experimental data indicate that the theory model needs refinement to be applicable to our system. Because we create large-amplitude phonons to maximize our detection signal, it is possible that this leads to non-linear damping effects [78], compromising our measurement of γ_{H}, and potentially causing the additional dependence on ϕ_{peak} seen in Fig. 6.7(b). Likewise, the simple scaling of c_θ with R holds only in the thin-ring approximation, and our smallest rings have thickness to mean radius ratio of 0.45.

Chapter 7: Conclusions and Outlook

This thesis presented the design and construction of an ultra-cold atom apparatus to produce sodium BECs in arbitrary potentials, particularly, in toroidal traps. The flexibility necessary for those traps required the careful design, characterization and implementation of optical systems that could work close to the diffraction limit. Furthermore, in order to generate arbitrary potentials we worked with an interesting piece of equipment, the DMD, and applied knowledge of wave and Fourier optics to design the projection optics.

One of the main challenges in building our experimental apparatus—besides vacuum leaks, unexpected power outages, a pandemic lockdown and equipment continuously dying[1]—, was to find the correct configuration of the multiple optical dipole traps that would allow us to produce reproducible results.

We used this tabletop system to realize an analogue model of cosmology, namely, to observe Hubble friction in an expanding universe. Our experimental results show signatures of red-shifting and attenuation of phonons in expanding toroidal traps, analogous to the red-shifting and attenuation of scalar fields in the

[1] I would like to acknowledge the unintentional growth of sodium hydroxide crystals in our "vacuum" chamber (also known as the collapse of the production chamber), the many IPG lasers that stopped working when we needed them the most, the dye laser that (luckily) did not form part of the final configuration of the apparatus and the assortment of water pumps that gave up along the way.

early universe, as it is currently understood in cosmology models. We also studied the inverse process in which the toroidal trap is contracted, leading to blue-shifting and amplification of phonons. Our results agree qualitatively with the theory, however quantitative agreement requires further development of the theoretical model, in particular, understanding the validity of the "thin-ring approximation" as it relates to our experimental parameters and understanding the corrections to the model when experimental variables, like atom number, are not kept constant.

Our group looks forward to continuing this line of research, among the cosmological models that are potential candidates for future experiments are the study of excitation pair production [20, 21, 83, 84, 85, 86] in expanding toroidal BECs in direct analogy with pair production in the expanding universe; and the study of the acoustic metric of vortices [7, 87, 88] in analogy to black-hole event horizons.

Appendix A: Imaging and DMD Projection Optics

In this chapter we review the design and construction of the imaging and projection optics as well as relevant characterizations.

A.1 Design of the Objective

One of the relevant length scales in BEC systems is the healing length, $\xi = (8\pi na)^{-1/2}$ [30], where n is the density and a is the scattering length. This is the characteristic length at which superfluid phenomena and density variations occur. Typical healing lengths in sodium condensates are around half a micrometer [60]. Although it would be desirable to resolve features comparable with the healing length, in practice achieving sub-micron resolution in cold atom experiments can be challenging because of the physical constraints set by the geometry of the vacuum chamber.

The main limitations to consider when designing an objective to image ultracold atoms are:

- Long working distances. For objectives outside vacuum, typical working distances are between 10 and 50 mm. In our chamber (see Fig. A.1) the distance from the center of the chamber to the window is 20.32 mm.

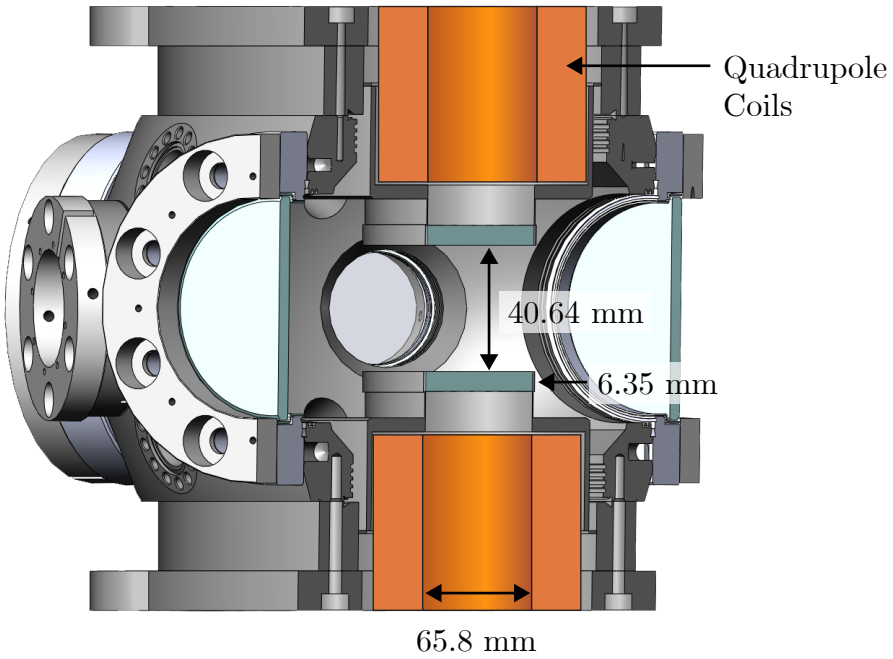

Figure A.1: Cross section of main body of the science chamber. The distance from the center of the chamber to the inner surface of the top viewport is 20.32 mm.

- Imaging is performed through a thick flat which introduces large aberrations, especially spherical aberrations when imaging is performed at high NA. Typical window thicknesses range from 1.5 mm to 8 mm. The window through which we image has a thickness of 6.35 mm.

- In stainless-steel chambers, the maximum optical aperture may be restricted by the size of the window through which the atoms are imaged. The optical aperture in our system is restricted to 65.8 mm in diameter.

In addition to the physical constraints imposed by the chamber, since the wavelength at which atoms are imaged is comparable to the desired resolution, aberrations limit the performance of the optical system. The resolution of an ideal imaging system is limited by diffraction, with the smallest separation between re-

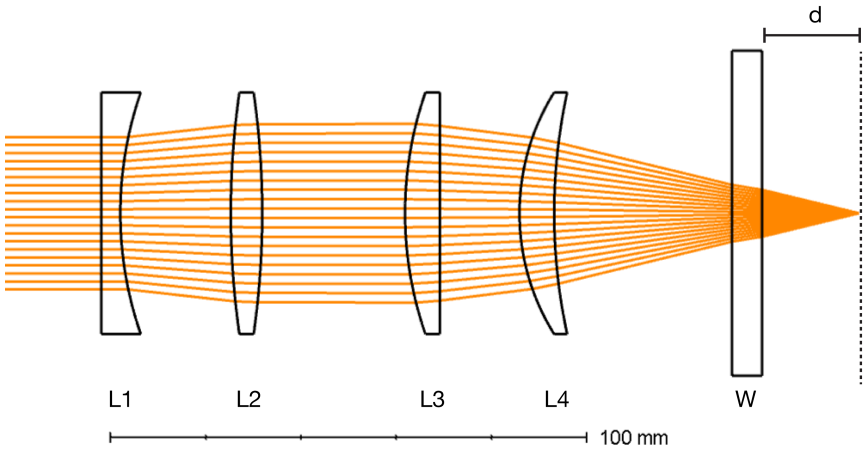

Figure A.2: Objective cross section. The objective was designed using four commercial singlets (L1-L4) and included the window (W) as an element in the optimization. The constraints set by the vacuum chamber geometry give a maximum clearance for 2 inch diameter optics, the window thickness is 6.35 mm and the distance from the window to the atoms, $d = 20.32$ mm.

solvable features given by[1]

$$R = \frac{0.61\lambda}{\mathrm{NA}}, \tag{A.1}$$

where R is the minimum separation between two point-like sources that can be distinguished from each other, λ is the light wavelength, and NA is the objective numerical aperture.

A work around for some of the limitations imposed by the vacuum chamber is to use in-vacuo optics [89, 90]; however, this approach presents some drawbacks including the need to work with only vacuum compatible materials, not being able to realign the system once the vacuum chamber is sealed, and potentially restricting optical access to the atoms. Another solution that has gained popularity in the ultra-cold atom community [91, 92, 93] is the design of a multi-element lens that balances positive spherical aberrations introduced by convex surfaces with negative

[1]This is also known as the Rayleigh resolution criterion [68]

Surface	Curvature (mm)	Thickness (mm)	Material	PN
1	∞	∞	Air	
2	∞	4.00	BK7	LC1611
3	77.2	23.20	Air	
4	179.1	6.60	BK7	LB1607
5	-179.1	30.00	Air	
6	77.3	7.30	BK7	LA1417
7	∞	16.74	Air	
8	47.87	7.29	BK7	LE1418
9	119.32	37.36	Air	
10	∞	6.35	Silica	Window
11	∞	20.32	Vacuum	

Table A.1: Objective Prescription. All lenses are catalogue singlets from Thorlabs with anti-reflective coating for visible light (A-coating).

spherical aberrations introduced by concave surfaces. This approach includes the vacuum window in the design so that the spherical aberrations introduced by the optical flat can be compensated.

We followed the outside vacuum approach to design an infinity-corrected objective[2]. To design the objective we used Zemax Optic Studio, a commercial ray-tracing software, to simulate and optimize the design. The goal was to achieve diffraction limited performance with NA$\geq$ 0.3 at multiple wavelengths: 589 nm used for absorption imaging and 532 nm used to project arbitrary potentials onto the atoms (refer to section 4.4.2 for a detailed description of the 532 nm optical setup).

[2]An infinity-corrected objective is an objective that focuses at infinity. It offers the flexibility of placing optical components, like dichroic mirrors, along the optical path. An eyepiece lens is then selected to focus the collected light onto a sensor for imaging purposes.

A.1.1 Objective Prescription

The optimization routine in Zemax minimized the squared sum of all wavefront aberrations up to 6th order using the default merit function. Once the lenses were selected, only the spacing between the surfaces was kept variable. We then simulated performance with different achromatic doublets to focus the image onto the camera and selected the lens for which the Modulation Transfer Function (MTF) was as close a possible to the diffraction limited MTF, this maximizes image contrast at all spatial frequencies up to the cut-off frequency given by $\xi_c = \mathrm{NA}/\lambda$ [92]. The objective prescription is presented in Table A.1 and a cross section of the final design is shown in Fig. A.2.

The final design has a NA of 0.28 and a corresponding resolution of 1.3 μm at 589 nm. It has an effective focal length of 68 mm and a back focal length of 20 mm. The resolution at 532 nm is 1.2 μm.

A.1.2 Objective Construction

The objective was designed using stock lenses from Thorlabs, the housing of the objective consists on two lens tubes from Thorlabs (SM2L03 and SML02). The lenses are separated using home made brass spacers[3]. The end of the spacers that meets flat lens surfaces was machined at 60° angle to guarantee that the lens position is defined by the distance set by the inner radius of the spacer, the appropriate SAG was calculated in each case. Figure A.3(a) shows the dimensions of the brass spacers,

[3]Thanks to Lester Putnam for letting me use the lathe in the IPST machine shop.

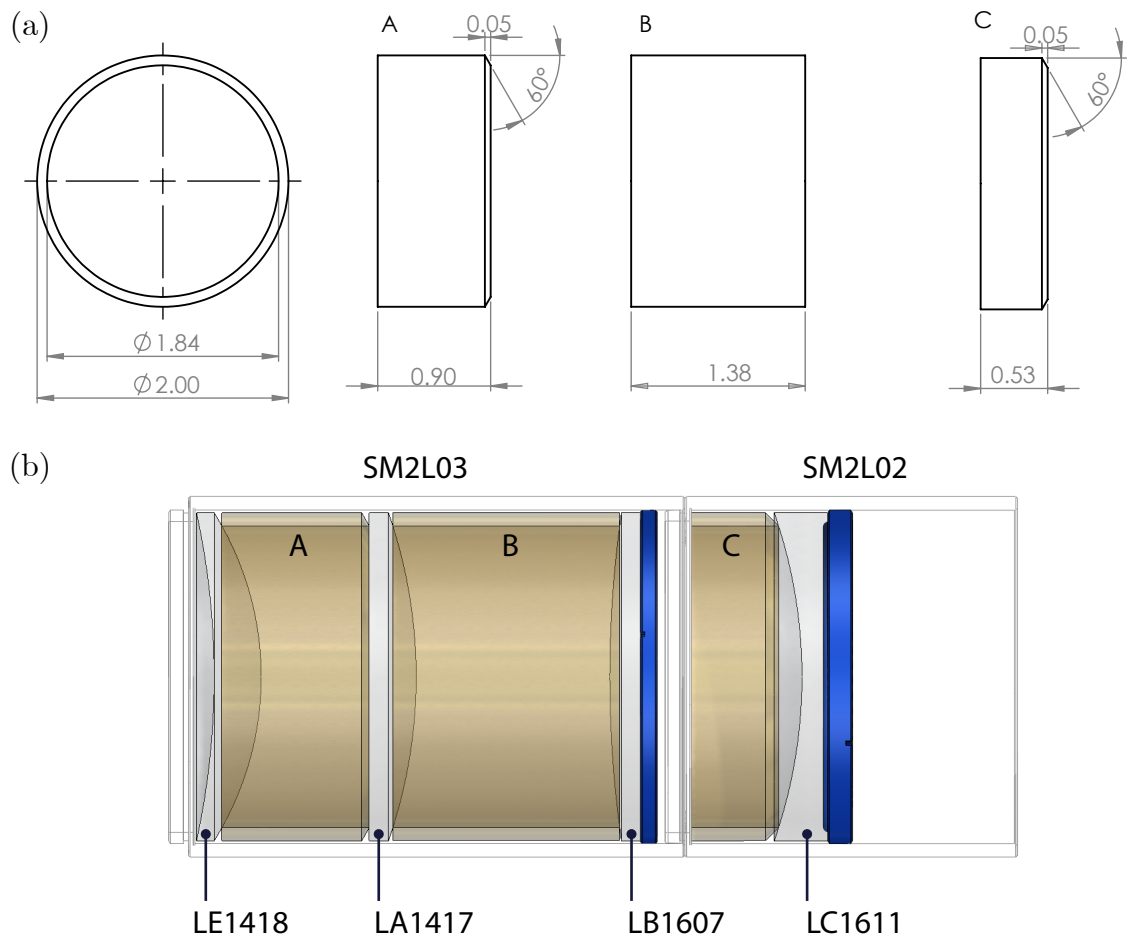

Figure A.3: Objective assembly. (a) Measurement of brass spacers. (b) Lenses and spacers in their housing made of stock Thorlabs lens tubes.

Fig. A.3(b) shows the objective assembly. In order to avoid Eddie currents in both the lens tubes and the spacers we made longitudinal cuts of 1 mm in thickness along the spacers and lens tubes, the gap was filled by 1 mm thick teflon to preserve the cylindrical shape of the elements.

The objective assembly is mounted on the top of the vacuum chamber as shown in Fig. A.4. We cut a 1/2 in thick Thorlabs breadboard[4] to the size of the top chamber coil form [Fig. A.4(a)]. The lens tube is held by two Thorlabs cage

[4]Thanks to Alessandro Restelli for letting me experiment with cutting thick materials using the CNC in the electronics room.

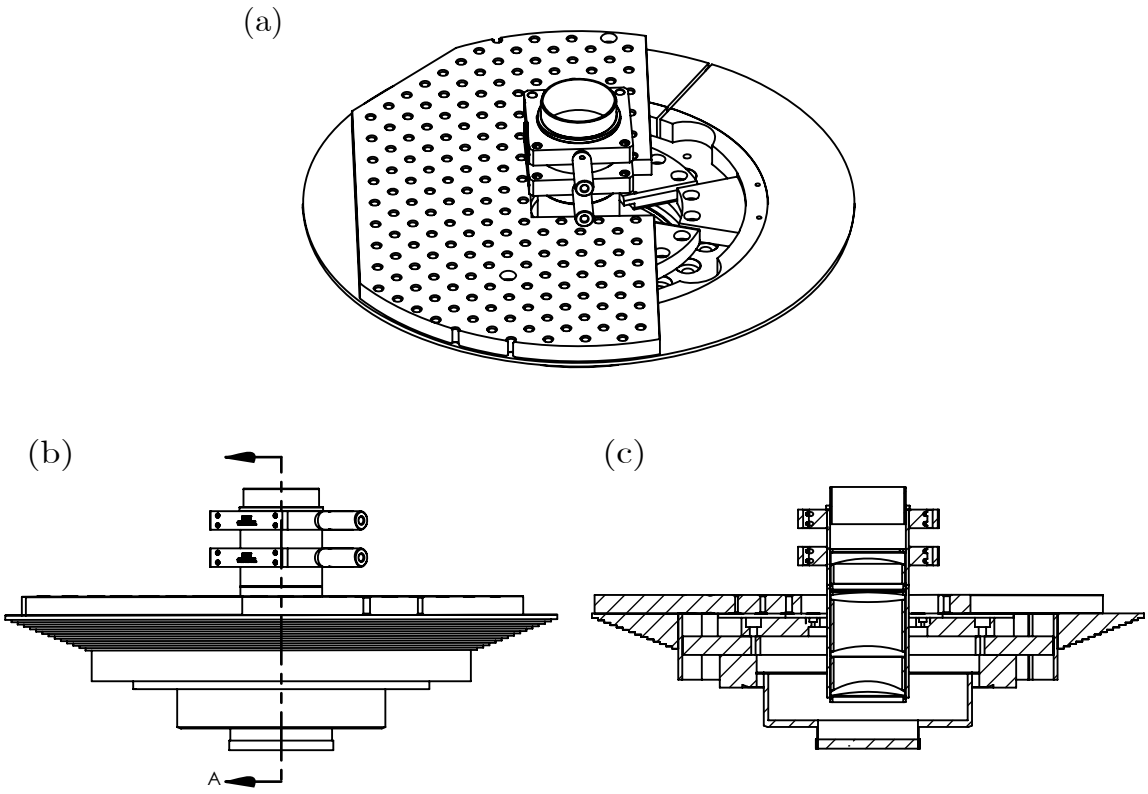

Figure A.4: Mount for the objective. (a) Isometric view of the objective, top coil mount and custom breadboard. (b) Side view of objective mounting assembly. (c) Cross section of (b) showing the lens tube housing the imaging objective mounted on the science chamber.

plates (LCP09) attached to a 3-axis translation stage (the translation stage is not shown in the figure). Figure A.4(b) and (c) show the position of the lens tube as it is lowered into the recessed bucket windows.

A.2 Integration of Imaging, DMD and MOT Paths

There are three different beam paths that go through the objective:

MOT beams. One of the 3D MOT cooling beams travels through the objective before reaching the atoms. In order to produce a collimated beam on the

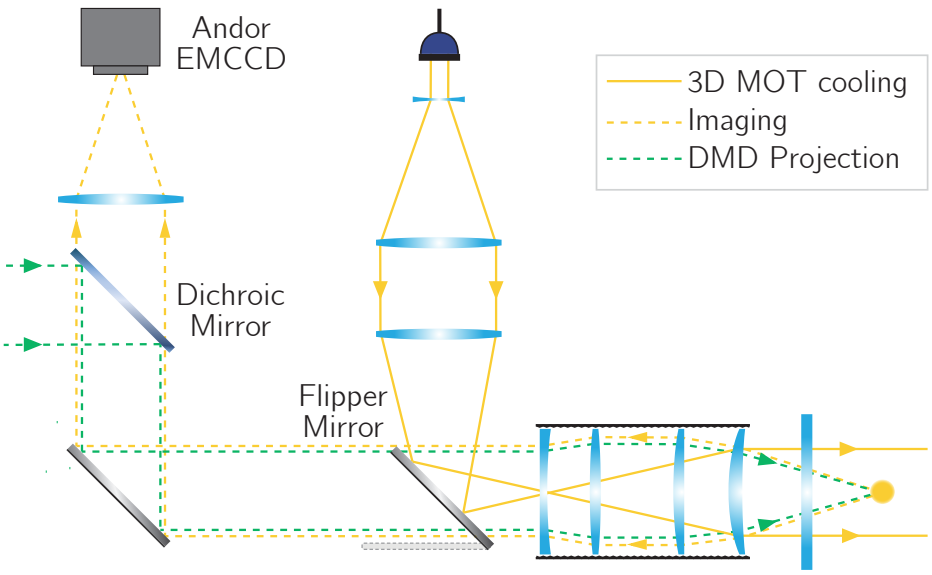

Figure A.5: Optical Setup for Imaging. The solid yellow lines correspond to the top 3D MOT cooling beam with optics that generate a collimated beam at the atom position. The dashed yellow lines trace the imaging path. The dashed green lines trace the DMD projection path (see figure 4.14 for complete projection optics). To switch between the solid path and the dashed paths a motorized mirror (New Focus 8892-K) is flipped between the two position depicted in the diagram.

MOT capture region we tested lenses with focal length between 100 mm and 250 mm from which we chose a Plano-Convex lens with focal length $f = 150$ mm.

Imaging path. The imaging path uses an achromat (Thorlabs AC508-400-A) to form an intermediate image with magnification $M \approx 5.9$. An additional commercial zoom lens is used to relay the image formed by the objective and achromat onto the camera.

DMD Projection. The lenses used in the DMD projection path are listed in table A.2. The DMD is positioned in the focal plane of L1, L1 and L2 are separated by a distance equal to the sum of their focal length ($d_{12} = f_1 + f_2$) with an iris positioned in the Fourier plane of L1, the iris is used to block undesired diffraction orders from the DMD. Lenses L1 and L2 form an intermediate image

Lens	Focal Lenght (mm)	Part Number
L1	500	AC508-500-A
L2	150	AC508-150-A
L3	500	AC508-500-A
L4	6.8	Objective

Table A.2: Lenses used in the DMD imaging path. L1 is the closest lens to the DMD.

that is re-imaged into the atom plane by the lenses L3 and L4 (in this case L4 is the objective).

The imaging path and DMD path beams are split by a dichroic beamsplitter (Semrock Di03-R532-t1-25x36) with cut-off wavelength $\lambda_c = 532$ nm—the DMD light ($\lambda = 532$ nm) is reflected off the dichroic while the probe used for imaging ($\lambda = 589$ nm) is transmitted.

A.3 Characterization of Resolution

We characterized the resolution of the imaging objective on a bench setup using a 1951 USAF Resolution Test Target. The PSF of the imaging system can be approximated with a Gaussian with $1/e^2$ width w [94], and by considering the response of the system when we image a square (defined by a Heaviside function in the object plane), the image of the square is the convolution of the PSF with the Heaviside function, which yields an error function profile with width w, $A \propto \mathrm{erf}\,(x/w)$. We use the square in the Test Target between groups 6 and 7 and fit each side to an error function from which we calculate w (see Fig. A.6), the discrepancy

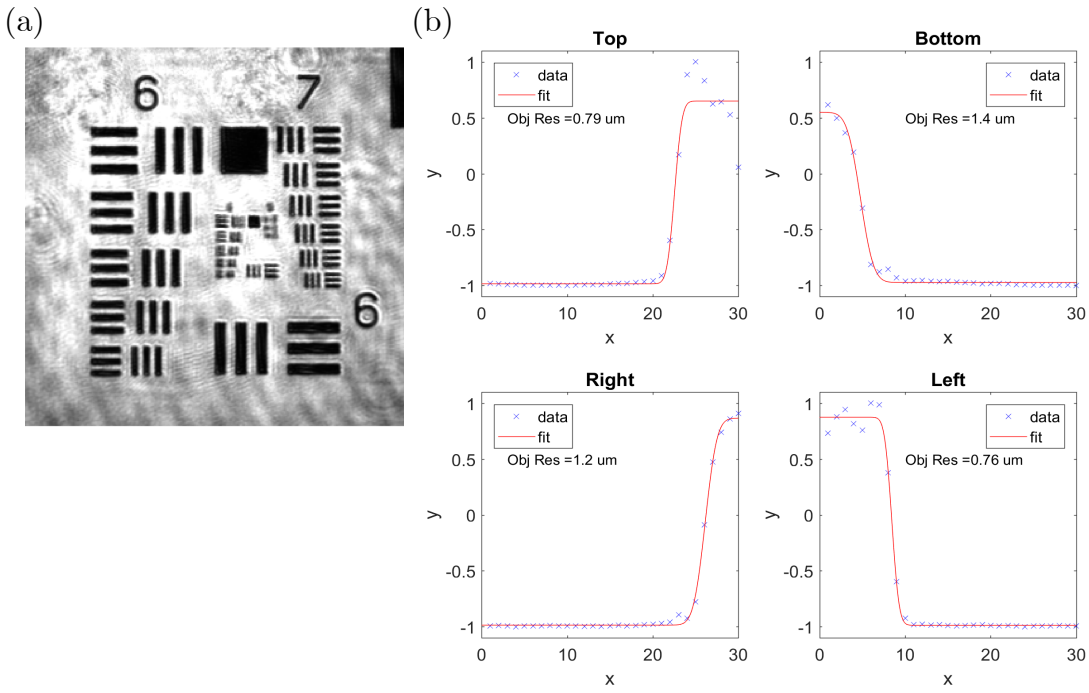

Figure A.6: Caracterization of the objective resolution using a USAF 1951 test target

between the values can be attributed to a tilt of the target with respect to the imaging axis. The resolution can be calculated by considering an Airy PSF with comparable FWHM to the gaussian associated with the error function used for fitting, the resolution can be calculated using[94]

$$D = 0.589 \times 3.83 \times w \tag{A.2}$$

We calculate w as the geometric mean of the values found by fitting each side of the square, then

$$D = 0.589 \times 3.83 \times 0.8 = 1.8\ \mu\text{m} \tag{A.3}$$

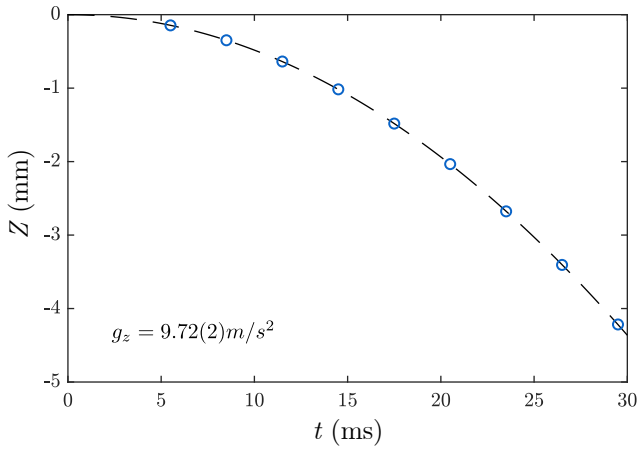

Figure A.7: Calibration of the horizontal imaging path which uses the camera FleaH1, found by fitting the BEC center of mass displacement in free fall.

A.4 Characterization of the Magnification

Here is the calibration of the magnification of the multiple imaging systems in our experiment starting with the imaging system with lowest magnification. The calibrations were performed in the final configuration of the system, meaning, not bench tests. Table A.3 sumarizes the value of the magnification for each path.

The characterization of the magnification of the horizontal imaging systems is performed by imaging a BEC in free fall and fitting the trajectory of the BEC's center of mass (COM) as a function of time of flight (TOF) according to

$$y(t) = M\left(y_0 + v_0\, t + \frac{1}{2} g\, t^2\right), \tag{A.4}$$

where $g = 9.806\,\mathrm{m/s^2}$ is the acceleration of gravity. Figure A.7 shows the characterization of the magnification of the horizontal imaging path that uses the camera FleaH1 (see Fig. 4.10 for reference). The expected magnification of the system based

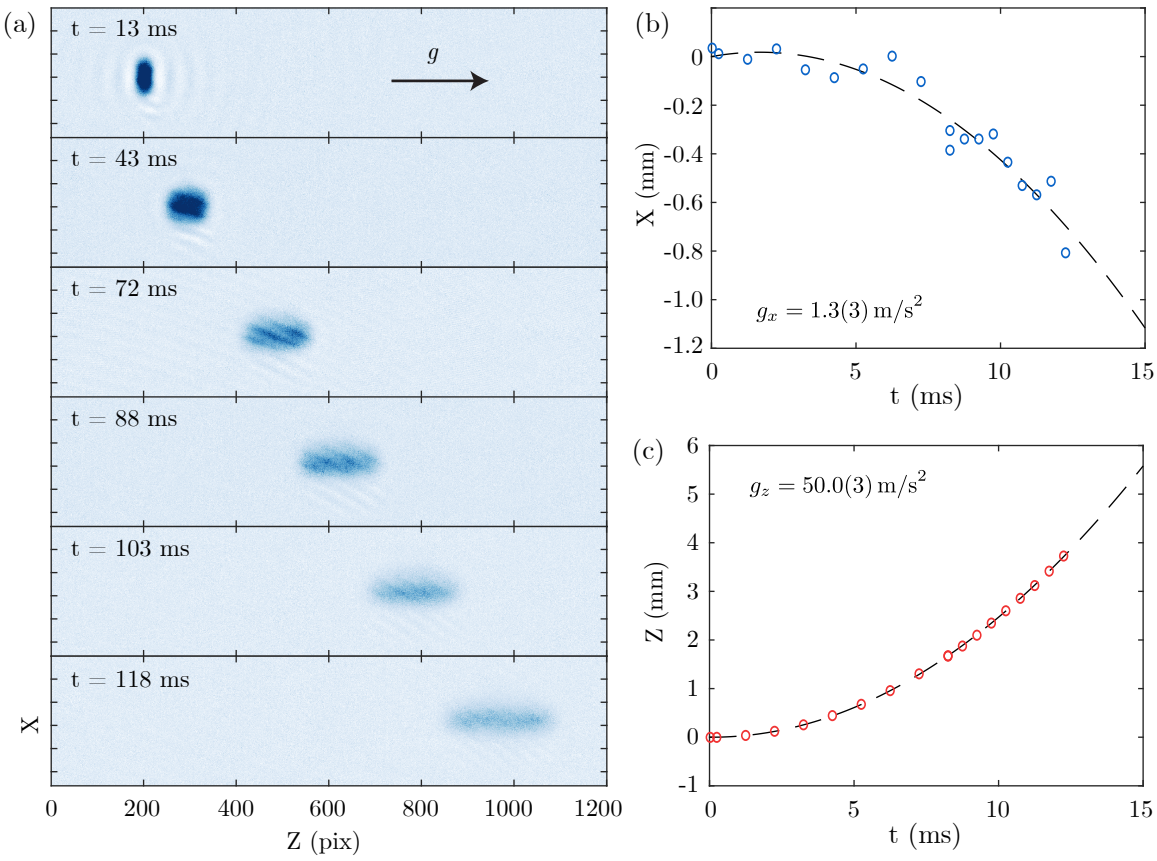

Figure A.8: Calibration of the horizontal imaging path which uses the camera FleaH4. (a) Displacement of the BEC for various TOF. (b) and (c) show the displacement of the BEC's COM along the camera x-axis and z-axis, respectively.

on the focal length of the lenses is $M_1' = 200/200 = 1$, the measured magnification is $M_1 = 9.72/9.806 = 0.99(1)$.

Figure A.8 shows the characterization of the magnification of the horizontal imaging path that uses the camera FleaH4 (see Fig. 4.10 for reference). In this case the camera presents a slight tilt with respect to the axis defined by gravity, as a result, the BEC's COM appears to be accelerated in two directions. The angle by which the camera is tilted can be found from $\theta = \mathrm{atan}(g_x/g_z) = 1.1°$. The expected magnification of the system based on the focal length of the lenses is $M_2' = (200/200)(500/100) = 5$, the measured magnification is

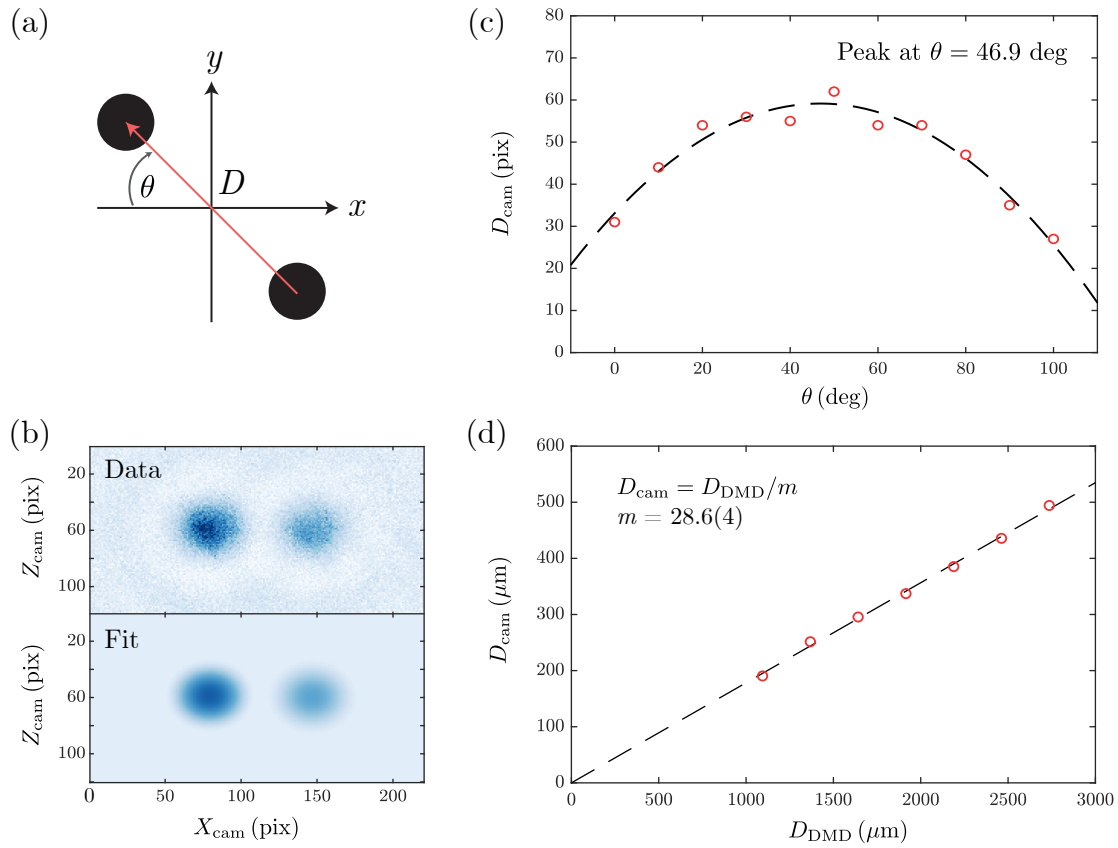

Figure A.9: Calibration of DMD path magnification. (a) DMD mask used to confine the BEC in two separate disk-shaped traps, the separation of the disks from center to center is given by **D**, θ is the angle that **D** forms with the DMD x-axis. (b) Horizontal image of the BECs and the fit to the data. (c) Determination of the angle θ that maximizes the separation of the BECs as seen on the horizontal camera FleaH4. (d) Separation between the disks on the camera vs. separation of the disks on the DMD.

$$M_2 \;=\; \sqrt{(50/9.806)^2 + (1.3)^2} \;=\; 5.10(3).$$

Calibrating the magnification of the vertical imaging path and the DMD projection path relies on the initial calibration of the horizontal path with large magnification (FleaH4). First, we calibrate the magnification of the DMD projection path by confining the BEC in the blue-detuned ODT with an in plane confinement given by two separate disks, Fig. A.9(a) shows the ROI of the DMD mask used for this purpose, the disk radius is 15 DMD micromirrors and the initial separation from

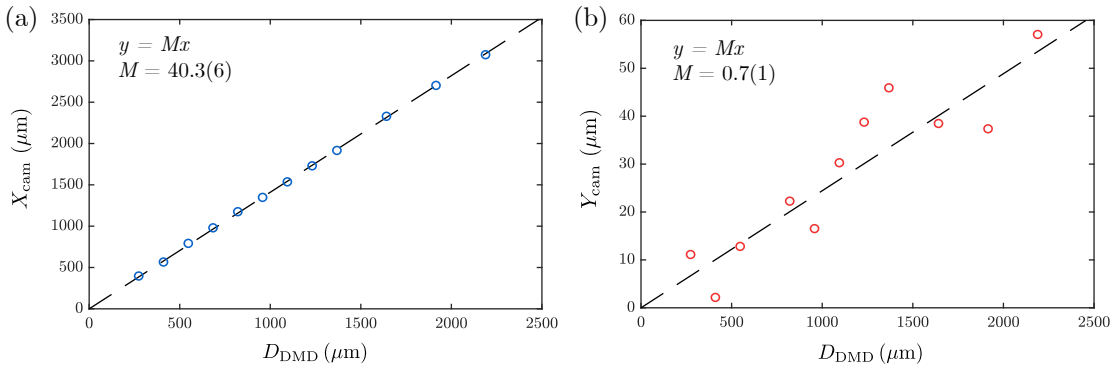

Figure A.10: Calibration of Andor path magnification by varying the separation between to disk-shaped BECs.

center to center is $|\mathbf{D}| = 20$ DMD micromirrors, the angle that $\mathbf{D}$ makes with what we define as the DMD x-axis is θ. The disk size and initial separation was chosen so that the BECs can be separately distinguished on the FleaH4 camera, as shown in Fig. A.9(b), we fit the two separate clouds to determine the separation between them. Figure Fig. A.9(c) shows the first part of this calibration in which the angle θ is varied in order to determine the orientation of the DMD mask for which $\mathbf{D} \perp \hat{e}_{\text{cam}}$ where $\hat{e}_{\text{cam}}$ is a unitary vector normal to the surface of the CCD of the camera, the value of the angle that maximizes the separation of the disks as seen on the camera is $\theta = 46.9°$.

The second step in the calibration of the DMD path magnification consists on varying the separation of the disks and plotting the separation of the disks in the image plane (D_{cam}) against the separation of the disks in the object plane (D_{DMD}). Although, in principle, measuring the separation of the disks for a single value D_{DMD} suffices to characterize the magnification, we repeated the measurement for 7 different values and fitted the points to $D_{\text{cam}} = D_{\text{DMD}}/m = M_{\text{DMD}} D_{\text{DMD}}$ in order to increase the calibration precision. The magnification expected from the focal length

Path	M	$p\,(\mu\text{m})$	$p'\,(\mu\text{m})$
FleaH1	0.99(1)	4.4	4.444(5)
FleaH4	5.10(3)	4.4	0.863(5)
Andor	40.3(6)	16	0.397(6)
DMD	$[28.6(4)]^{-1}$	13.68	0.479(7)

Table A.3: Summary of magnification. M is the magnification of the path, p is the physical size of an array element—a pixel in the case of the cameras and a micromirror in the case of the DMD—and p' is the size of an array element on the atom plane. The value in parenthesis represents one standard deviation combination of statistical and systematic errors.

of the elements in the projection path is $M'_{\text{DMD}} = (150/500)(68/500) = 0.041$, the magnification obtained from the fit is $M'_{\text{DMD}} = 0.035(1)$.

After determining the magnification of the DMD path we can calibrate the magnification of the vertical imaging path (Andor camera) using the method of creating two disk-shaped BECs and varying the separation between them. Figure A.10 shows the result of this calibration, we measure the separation of the disks along the x and y axis of the Andor camera, the magnification of the vertical imaging path, including the zoom lens, is $M = 40.3(6)$.

A.5 Vertical Probe Intensity Calibration

We reviewed in Chapter 3.6 Beer-Lambert's law (Eqn. 3.52) to calculate the atom number in the atomic cloud (N) from the imaged column density ($\tilde{n}$)

$$N = \tilde{n}(x,y)\sigma_0 = -\ln\frac{I_{\text{a}} - I_{\text{b}}}{I_{\text{p}} - I_{\text{b}}} + \frac{I_{\text{p}} - I_{\text{a}}}{I_{\text{sat}}}\ .$$

At low probe intensities, $I_p \ll I_{\text{sat}}$, the second term in Eq. (3.52) can be neglected; however, when the probe intensity is comparable to the saturation intensity (I_{sat})

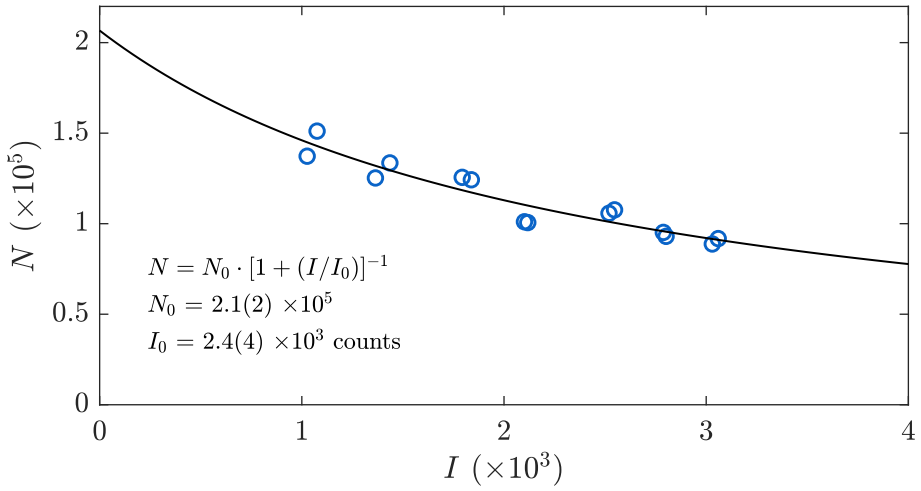

Figure A.11: Calibration of I_{sat} in camera counts for the vertical imaging path. The horizontal axis corresponds to the mean count per pixel for probe images. The vertical axis represents the atom number as calculated using only the logarithmic term in Eqn. (A.5).

the second term in Eq. (3.52) must be taken into account to correctly measure the atom number [57, 95]. Let N_0 be the atom number calculated at $I_p \ll I_{\text{sat}}$ and $\tilde{N}$ the atom number calculated just from the logarithmic term, without intensity corrections, then

$$\tilde{N} = N_0 \left[1 + \frac{I}{I_0}\right]^{-1}, \tag{A.5}$$

where I is the mean probe intensity. Figure A.11 shows the calibration of the saturation intensity in term of camera counts (I_0) for the vertical imaging path. We varied the intensity of the vertical probe beam and recorded the mean number of counts for the probe beam in the region where the atoms are located (I) and the atom number calculated from $\tilde{N} = -\ln[(I_{\text{a}} - I_{\text{b}})(I_{\text{p}} - I_{\text{b}})]$. The values were fitted to Eqn. (A.5) from which we obtained that $I_0 = 2.4(4) \times 10^3$ counts.

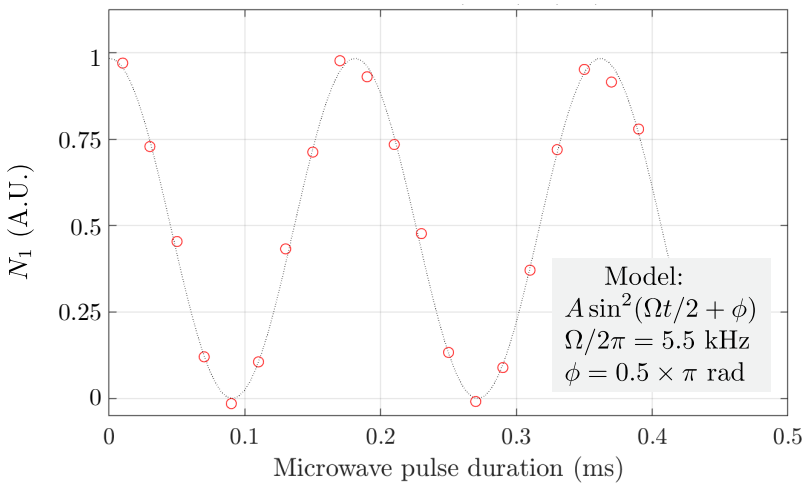

Figure A.12: Calibration of the microwave pulse duration for PTAI. The figure plots atom number in the ground state as a function of the microwave pulse duration.

A.6 PTAI Rabi Frequency Characterization

The procedure to calibrate the microwave pulse used for PTAI consists on confining the BEC in a disk-shaped blue ODT, applying a variable duration microwave pulse followed by a "Stern-Gerlach kick" with a magnetic gradient `HSG` (see table 5.1). Then, we image the atoms in the $F = 1$ and count atom number as a function of microwave pulse duration, see Fig. A.12, the corresponding Rabi frequency is $\Omega_{\mu W} = 2\pi \times 5.5$ kHz.

A.7 Probe Reconstruction

All the ring images taken with the vertical camera—this includes all images of rings—are taken using PTAI (chapter 3.6) which, similar to absorption imaging, uses 3 images to calculate the optical density (OD) of the atomic cloud: an image of the probe and atoms (I_a), and image of the probe without atoms (I_p) and an image of

the background (I_b), that is, no probe is shone. A typical imaging sequence takes the three images consecutively—on the order in which the images where listed above—, the time interval between each image is in the order of 300 ms and limited by the readout time of the camera. There are two practical issues that arise from taking images in this fashion: the intensity of the probe beam, although intensity stabilized, fluctuates from shot to shot; and far more problematic are pointing instabilities that result in shifts between the probe in the image with atoms (I_a) and the probe in the image without atoms (I_p) which result in fringing effects when the OD is calculated (see Fig. A.13).

The solution [95, 96, 97] to both of these problems consists in reconstructing the probe present in the image with atoms I_a using a basis of probes that is representative of the main variations of the probes taken over the course of a day. This process is analogous to the eigenface problem well documented in data science [98] in which single value decomposition (SVD) is used to efficiently calculate the principal components (PC), read eigenvalues, of a given matrix. Figure A.13 shows two cases[5] of ODs calculated with and without probe reconstruction, since the work presented in this dissertation has a particular focus on toroidal BECs the figure of merit for comparison is the signal to noise ratio (SNR) defined, in terms of the mean and the standard deviation (stdv) of the radially integrated OD (OD_{1D}), as

$$\mathrm{SNR} = \frac{\mathrm{stdv}[OD_{1D}]}{\mathrm{mean}[OD_{1D}]}. \tag{A.6}$$

[5]The images were selected to show the worst case scenario.

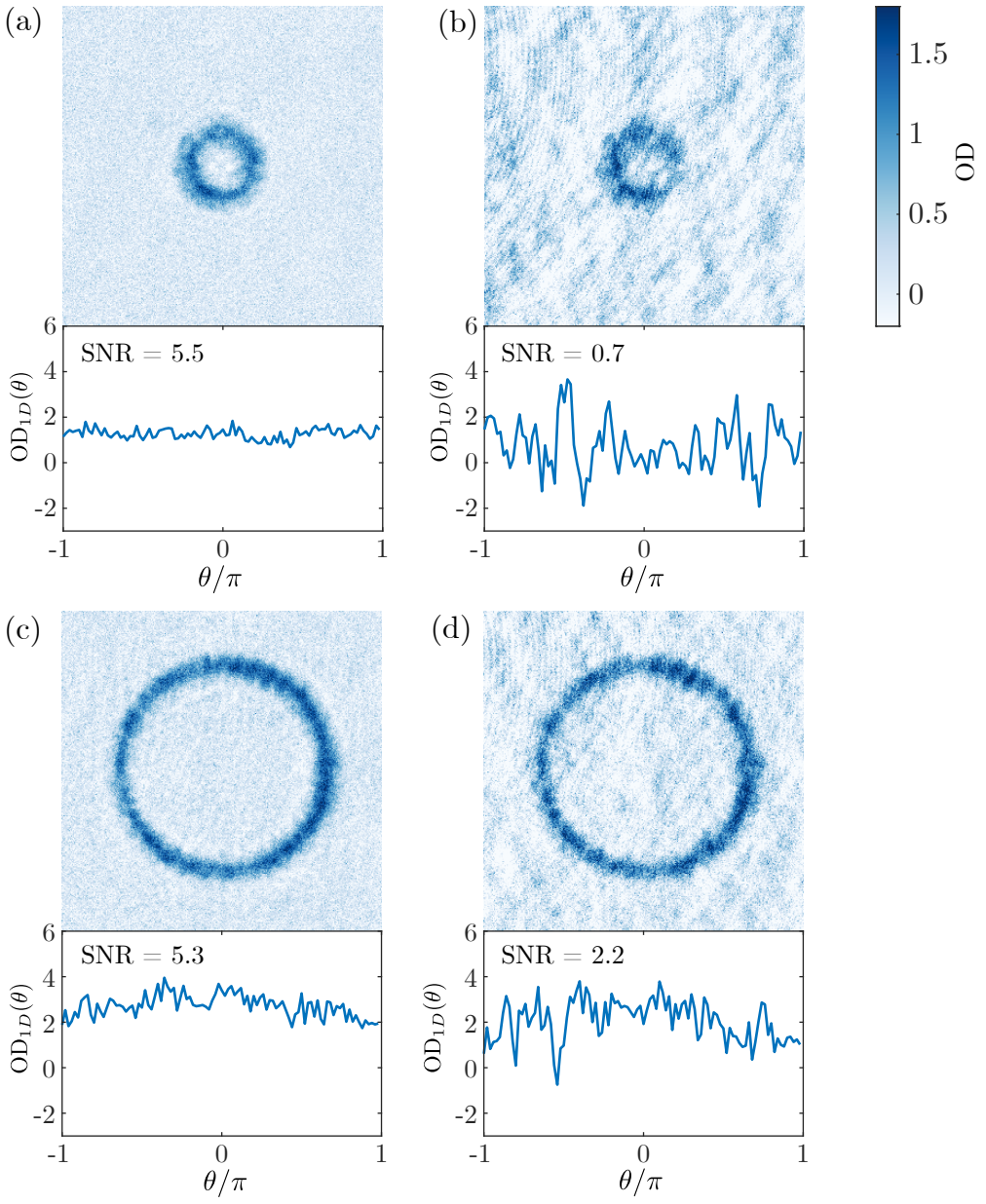

Figure A.13: Probe Reconstruction. (a) and (b) correspond to the same absorption image of a ring with radius $R \approx 12$ μm, (a) is calculated with a reconstructed probe image, (b) is calculated with the probe image taken right after the absorption image. (c) and (d) same as (a) and (b) for a ring with radius $R \approx 38$ μm. See text for additional details.

We typically confine $N \approx 1.2 \times 10^5$ atoms in the toroidal trap, for rings with smaller radius this results in higher densities; consequently, to maintain ODs in in the order of 1.5 the transfer fraction for PTAI is adjusted so that less atoms are imaged for smaller rings than for larger rings, a drawback of working with small transfer fractions is an increase in "raw" SNR, compare Fig. A.13 (b) and (d). However, once probe reconstruction is implemented, small and large rings show similar SNR values, Fig. A.13 (a) and (c).

A.8 Characterization of the DMD Beam

Section 4.4.2 discussed the diffraction considerations when working with a DMD, given the wavelength of the light ($\lambda = 532$ nm), the tilt ($\gamma = 12°$) and the pitch ($d = 13.68$ μm) of the micromirrors, from Eq. (4.5) we find that there are 4 bright diffraction orders when the DMD is illuminated at the Blaze angle $\theta = 2\gamma = 24°$. Figure A.14 shows the simulation of the diffraction orders (a) which are off-centered with respect to the optical axis marked by the cross; (b) shows the observed diffraction orders on a bench test, (a) and (b) qualitatively agree with one another; (c) shows the measured power in each of the four brightest beams shown in (b) normalized to the combined power of the four beams. Consequently, for the alignment of the deployed projection optics we steered the illuminating beam so that the brightest of the 4 beams would propagate along the optical axis, this had the undesired outcome of displacing the illuminating beam away from the center of the DMD, which was the ideal configuration.

(a) (b) (c)

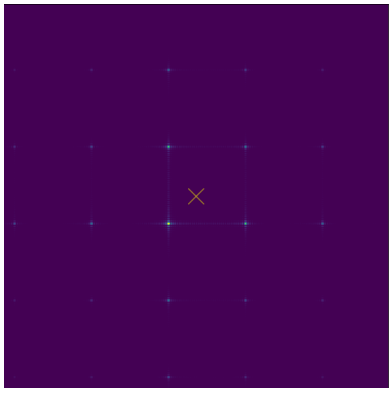

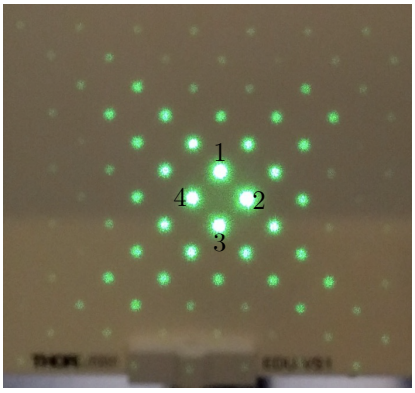

Beam	P/P_c
1	0.28
2	0.30
3	0.26
4	0.17

Figure A.14: DMD Diffraction Orders. (a) Simulated diffraction orders for light incident at 24°, the cross marks the direction normal to the surface of the DMD. (b) Diffraction orders from bench test and (c) powers of the four brightest diffraction orders normalized to the sum of the power of the four beams (P_c).

We characterized the final intensity of the illuminating beam on the surface of the DMD in order to project ring potentials with approximately radially symmetric intensity. The method to characterize the beam consisted on projecting a beam with the DMD using a small disk with radius $R = 30$ micromirrors and measuring the power as a function of the disk center, Fig. A.15(a) shows the position of the illuminating beam on the DMD, the open circles mark the positions where disks were projected, their radius is proportional to the reflected power measured for a disk centered at that position, the red circle marks the position of the disk for which the reflected power was maximum.

Once the center of the beam was identified, we assumed[6] the intensity profile

[6]Let us assume that the illuminating beam is an ideal Gaussian beam with $1/e^2$ radius w, given that the beam is incident on the surface of the DMD at an angle θ the intensity profile on the surface of the DMD will be elliptical with minor and major $1/e^2$ radius given by $w_{\min} = w$ and $w_{\max} = w/\cos\theta$. We assumed $1/\cos(24°) = 1.1 \approx 1$, then $w_{\max} \approx w_{\min} = w$.

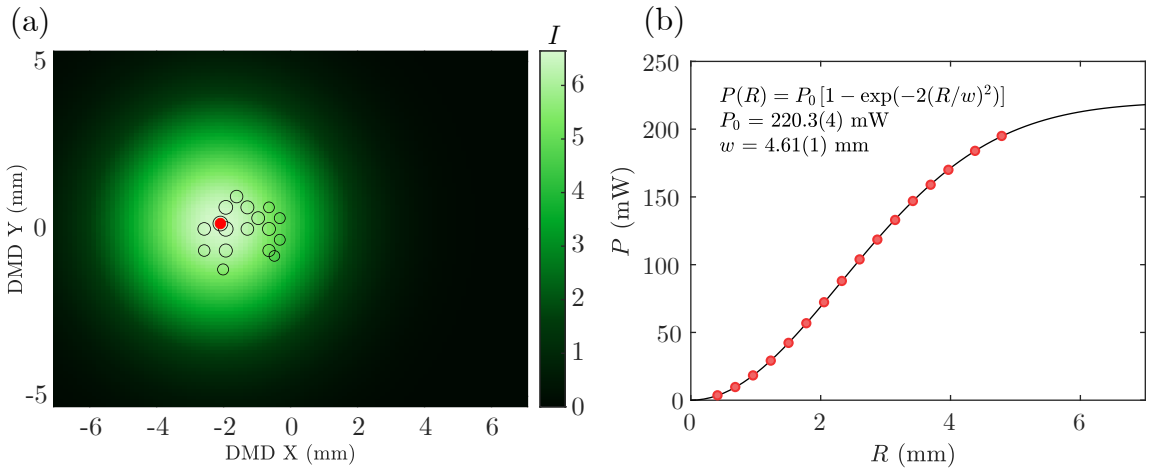

Figure A.15: Characterization of DMD beam. (a) Reconstructed beam intensity on the surface of the DMD, the red circle marks the center of the beam. The open circles mark the positions where disks were projected, their radius is proportional to the reflected power measured for a disk centered at that position (see text for additional details). (b) Beam $1/e^2$-radius w measurement. See text for additional details.

on the surface of the DMD was

$$I(r) = I_0 \exp\left[\frac{-2r^2}{w^2}\right], \tag{A.7}$$

where r is the radial coordinate centered at the beam peak intensity I_0 and w is the beam $1/e^2$-radius. Then, the power within a radius R is found from integrating Eq. (A.7) from zero to R yielding

$$P(R) = P_T\left[1 - \exp\left(\frac{-2R^2}{w^2}\right)\right], \tag{A.8}$$

with P_T the total power in the beam. We projected beams using DMD disk masks with increasing radius and fitted the measured power to Eq. (A.7), see Fig. A.15(b), from which we found the beam $1/e^2$-radius $w = 4.61(1)$ mm, Fig. A.15(a) shows the

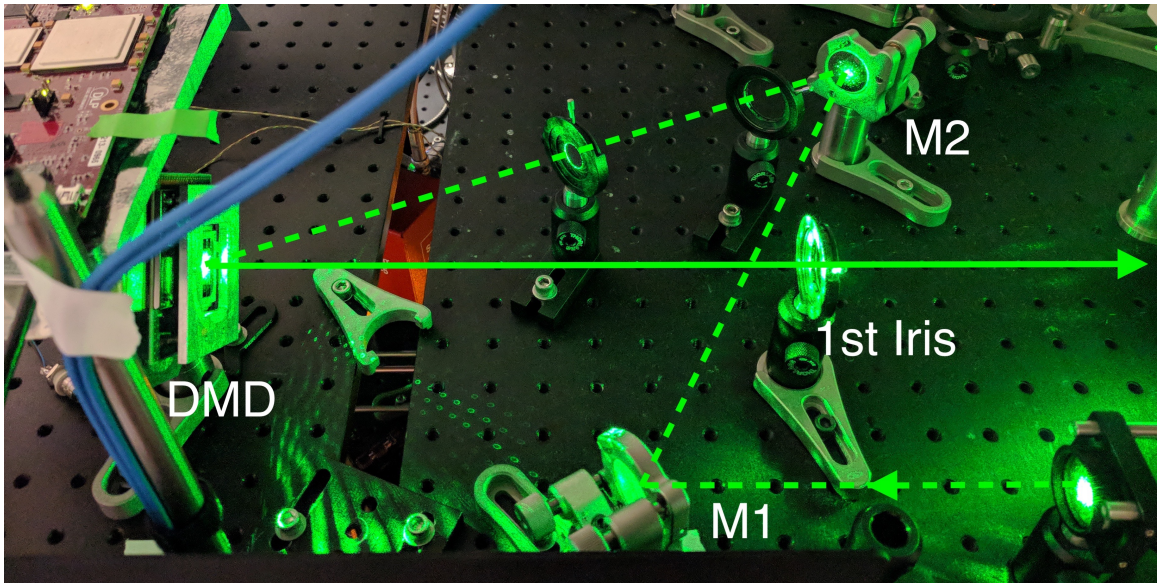

Figure A.16: Alignment of the DMD path (I). The figure shows mirrors M1 and M2 that are used to align the illuminating beam represented by the dashed green line, the solid green line represents the beam diffracted off the DMD as it goes through the first alignment iris.

resulting reconstructed beam intensity on the surface of the DMD.

This measurement is an approximation since, as mentioned previously, the beam is expected to have an elliptical profile about a coordinate axis rotated[7] 45° with respect to the DMD $x - y$ coordinate axis described in Fig. A.15(a). The measurement could be improved by automating the measurement of the power reflected by individual mirrors—for the characterization presented in this section we measured the power using a power meter and recorded the values manually—.

A.9 Alignment of the DMD Path

This section details the procedure used to align the DMD trap if, for some reason, it is misaligned. The procedure is divided into two stages, a rough alignment

[7]this is the result of mounting the DMD at 45° since it is designed for corner illumination.

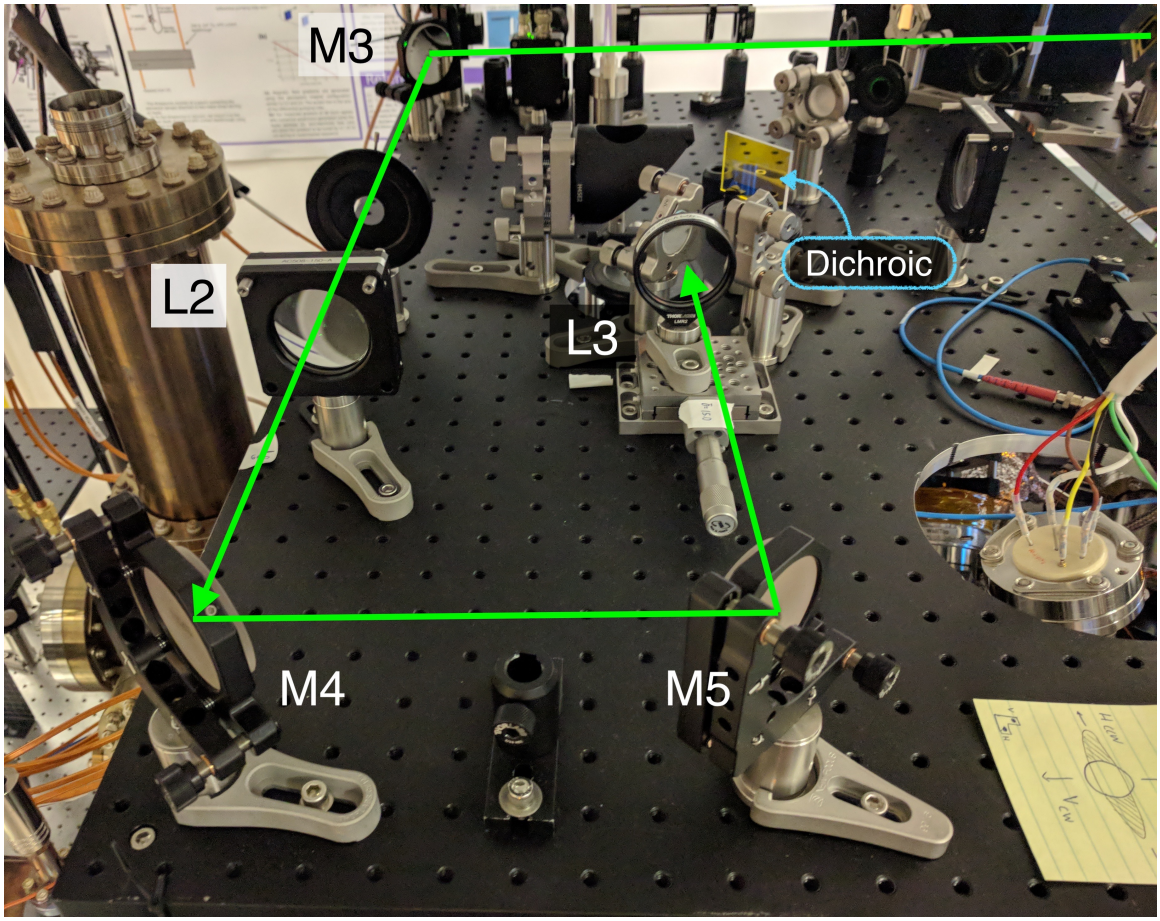

Figure A.17: Alignment of DMD path (II). The figure shows the mirror (M3) used to align the beam as it goes through the Fourier plane iris and the second lens (L2). The mirrors M4 and M5 are used to center the beam on the third lens of the array (L3) which is mounted on a z-axis translation stage. The dichroic reflects the DMD beam ($\lambda = 532$ nm) and transmits the vertical imaging probe ($\lambda = 589$ nm).

that brings the DMD beam close to the position of the atoms, and a fine alignment for precise overlap of the DMD trap and the hybrid trap.

Rough alignment procedure:

- Program the DMD to display continuously[8] a (bright) small disk, a disk with radius of 20 DMD mirrors was used here. It is worth mentioning that the beam reflected by the DMD exhibits concentric rings right after the DMD without

[8]To do this stop SetList and control the DMD with the proprietary software ALP.

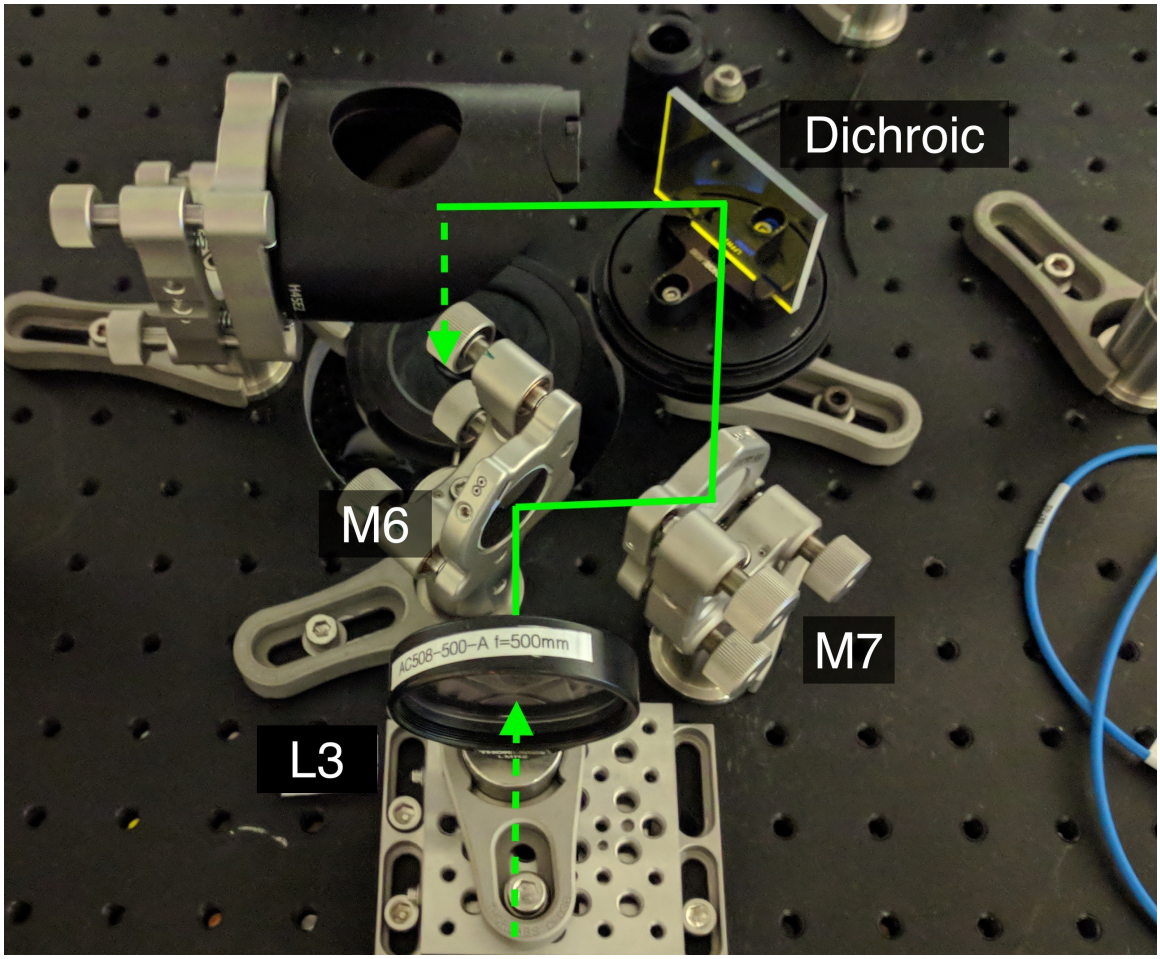

Figure A.18: Alignment of DMD path (III). The figure shows lens L3 and the folding mirrors that align the beam with respect to the hybrid trap. The solid line represents the beam as it travels on the horizontal plane before being reflected downwards (dashed line pointing down) by the periscope mirror and towards the imaging objective.

being restricted by any aperture, presumably as a result of diffraction effects.

- Use the two mirrors that steer the illuminating beam (M1,M2) to center it on the first iris and the lens right after the iris, see Fig. A.16.

- Proceeded to center the beam on the second lens (L2) and iris using mirror M3, see Fig. A.17.

- Using the 2 folding mirrors (M4, M5) before the lens on the translation stage

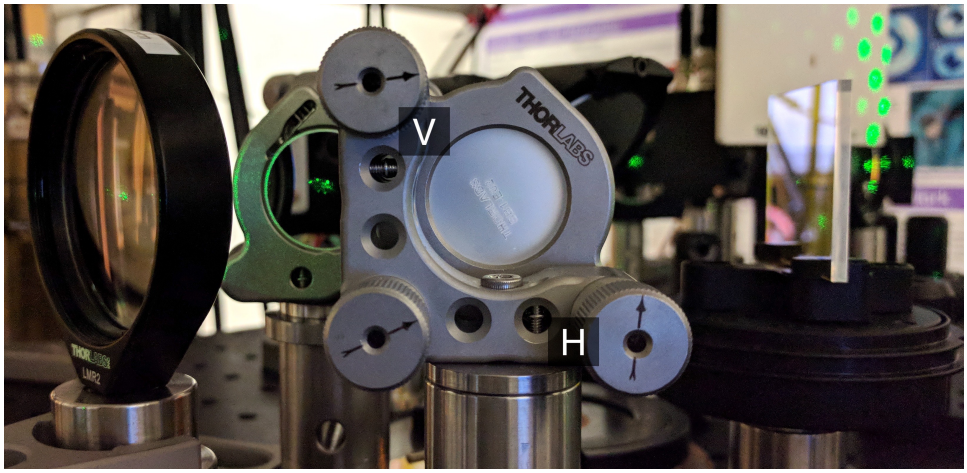

Figure A.19: Labeling of the knobs on the mirror M7.

(L3), align the beam so that it remains centered on the lens at both end positions of the translation stage.

- Use the mirrors M6 and M7 located between the last lens (L3) and the dichroic to align the beam so that it is centered on the top iris and an alignment target mounted on the top of the objective, see Fig. A.18.

- Once the initial alignment is completed proceed to image the atoms in the hybrid trap using the vertical camera for fine alignment.

Fine alignment procedure:

- Scan the position of the DMD beam using the H and V knobs on the last mirror (M7) right before the dichroic (see Fig. A.19) until the DMD beam depletes atoms in the hybrid trap, usually less than half a turn of the knobs is needed in order to align the traps.

- If the last step fails, a larger disk mask can be used for the initial alignment, once atoms are depleted from the hybrid trap switch to a smaller disk for fine

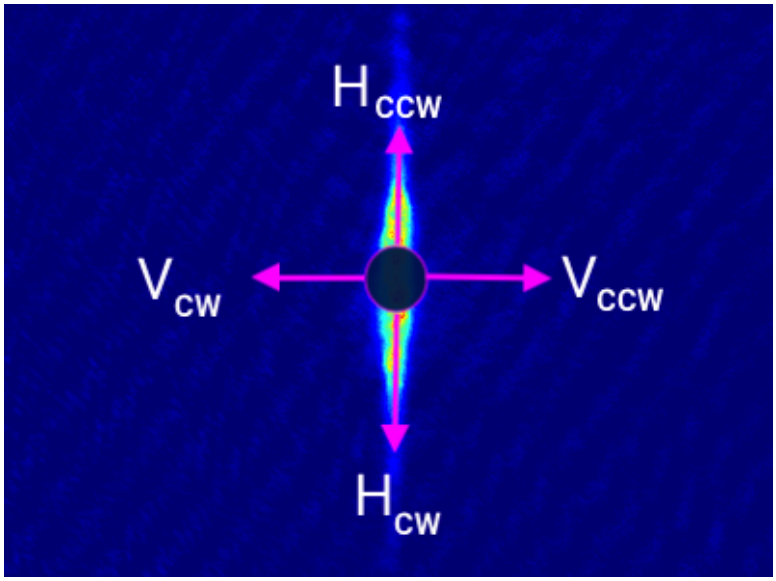

Figure A.20: Alignment of DMD diffracted beam as seen on the vertical camera. The figure illustrates the direction in which the DMD beam is steered by turning the horizontal (H) and vertical (V) knobs of the mirror M7 in clockwise (CW) or counter-clockwise (CCW) direction. When the beam is correctly aligned it will deplete atoms from the center of the hybrid trap as simulated in the figure.

tuning.

- Figure A.20 shows an image of the hybrid trap in-situ as seen from the top, the magenta arrows indicate the direction of displacement of the DMD beam when turning the knobs on M7, CW indicates clock-wise turn of a knob, CCW indicates counter-clock-wise rotation.

Appendix B: The Good, the Bad, and the Ugly

First of all I would like to acknowledge that the title of this appendix was inspired by a chapter's title in the doctoral dissertation of Ana Valdes-Curiel [99], and on the same spirit as the aforementioned chapter I would like to use this space to discuss a (non-comprehensive) list of aspects of the Sodium Rings Laboratory at UMD that, as the title indicates, are good, bad, or simply suboptimal (the ugly).

B.1 The Good

The magnetic coils. The magnetic coils and water manifold was designed by Madison Anderson, she did a great job designing and building a set of coils that have served their purpose without any issues. The coils are currently underutilized and I hope in the future someone will exploit their full capabilities.

The gate valve. Having a gate valve between the science chamber and the production chamber could have been an unnecessary precaution, yet it was not. When the bake-out of the production chamber did not go as expected (more on that point below) the gate valve saved the science chamber from being exposed to the environment, see Fig. B.1.

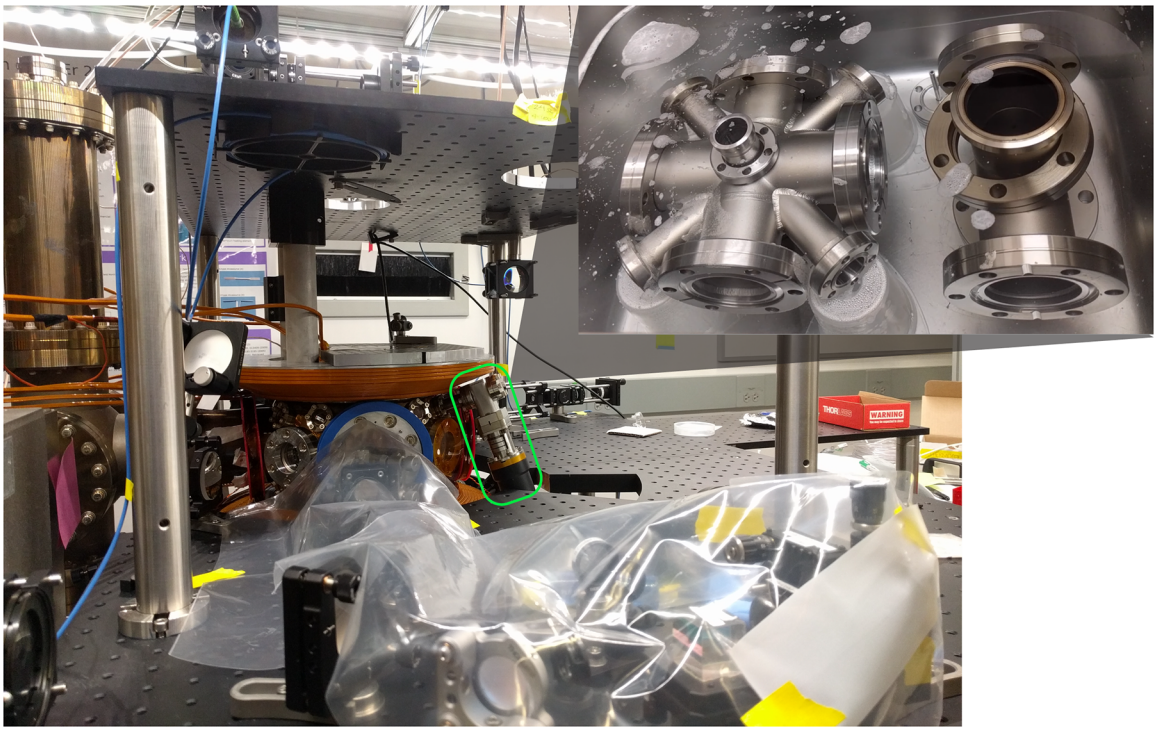

Figure B.1: Gate valve doing its job. The gate valve (marked in green) kept the science chamber away from exposure to the environment while the production chamber was washed (inset). The IR optics were protected with a plastic bag.

The imaging optics and the DMD. I am clearly biased on this point since I spent a fair amount of time thinking and designing the elements that form part of the imaging and projection optics. The system could be better but as it currently stands it works well and, of the three dipole traps in use, the DMD trap has proven to be the most robust. If I were to design the optics for these paths again I would consider an approach similar to the design presented in Ref. [72] since it offers the ability to directly image the light projected onto the atoms. Additionally, I would use a DMD that offers better diffraction efficiency at 532 nm—we have recently purchased a DMD that is more suitable to work with 532 nm light, the DLP9500, it is now a matter of integrating this DMD into the current system—.

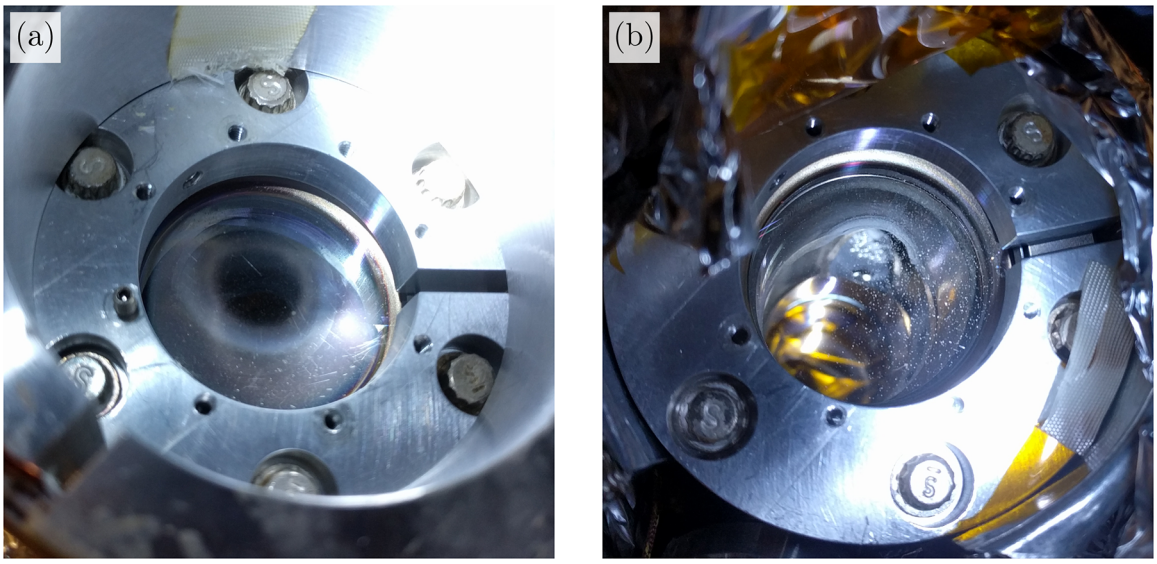

Figure B.2: Coated Viewport. The figure shows one of the viewports through which a 2D MOT cooling beam enters the production chamber. (a) Viewport with a halo of sodium that has accumulated on the inner surface of the glass rendering the window partially reflective. (b) Clear window after being heat treated.

B.2 The Bad

The production chamber. This is the source of sodium atoms and of 90% of the headaches in the laboratory. One of the constant struggles in our system has been trapping the same number of atoms day after day, while it is expected that slow drifts happen over time, we constantly found ourselves struggling to optimize many experimental parameters—alignment of the 2D MOT optics, optimization of shimming fields for the 2D MOT and 3D MOT, etc.—to produce condensates with $N \approx 4 \times 10^5$ atoms in the hybrid trap. This number is the empirical threshold below which working with the blue detuned ODTs becomes unreliable, for instance, it is not possible to observe a phonon oscillation. We mainly attribute the decline in atom number to the slow deposition of sodium on the viewports through which the 2D MOT cooling beams enter the production chamber (see Fig. B.2).

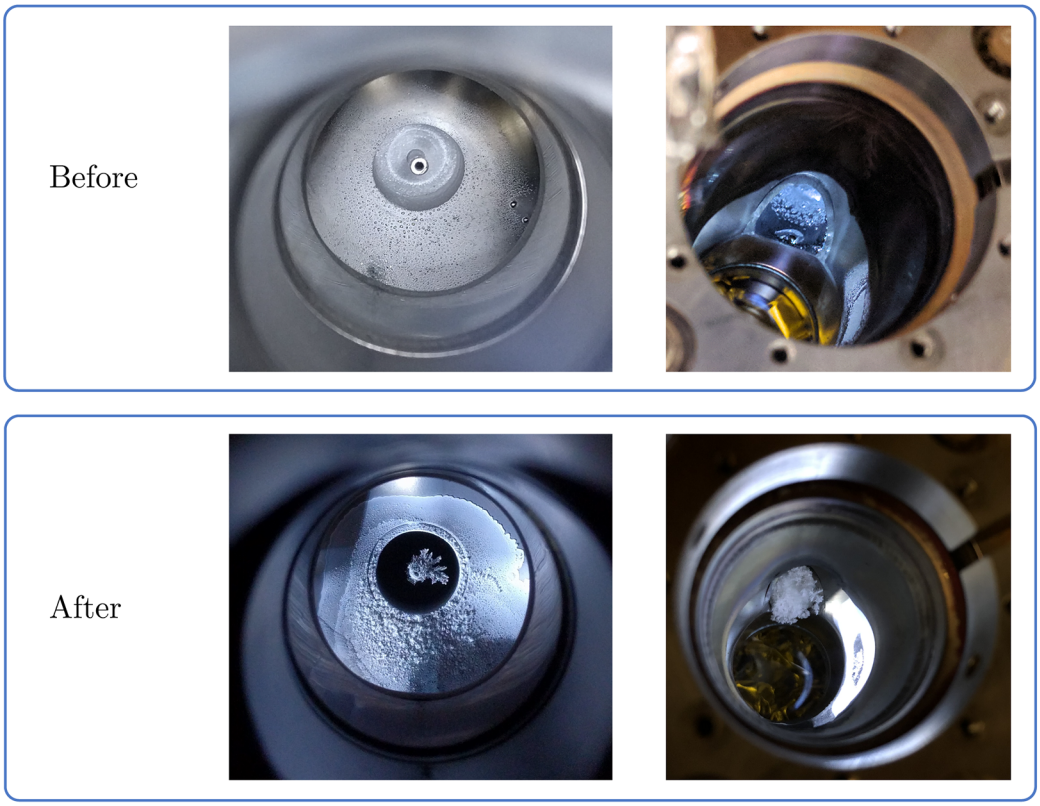

Figure B.3: Sodium hydroxide crystals. The images on the left show the differential pumping tube, the images on the right show the access to the sodium reservoir. The before images show how sodium had accumulated on various surfaces inside the vacuum chamber. The after images show sodium hydroxide crystals that formed after a vacuum leak that occurred while baking the chamber to clear the viewports coated with sodium.

A partial solution to the viewport coating problem is to heat treat the viewports (bake-out the viewports at $T \approx 120^{\circ}$ for a couple of days) to remove the sodium that has accumulated on them. However, and this is a big however, bake-out is a disruptive process that requires removing optics from around the chamber and poses the threat of misaligning many of the beam paths surrounding the production chamber. Additionally, vacuum leaks may occur while baking the system as we learned back in 2018 (see Fig. B.3); while baking the production chamber to

clear the viewports there was a vacuum leak[1] which resulted in sodium hydroxide crystals growing inside the chamber and which destroyed the NEXTorr pump and ion gauge on the production chamber.

A better solution to this problem would be to redesign the sodium oven so that it does not spray sodium onto the viewports. My suggestion is to have the reservoir at angle with respect to the plane defined by the 2D MOT beams and perhaps a cold surface in front of it. If this is ever done and the chamber is rebuilt I would also add a viewport that allows looking at the 2D MOT orthogonally, this brings us to the second major issue regarding the production chamber: lack of direct diagnostics.

Although we attribute the decline in atom number to the viewports getting coated, we do not have direct diagnosis of the 2D MOT performance—we optimize parameters related to the 2D MOT by looking at the atoms trapped in the 3D MOT. If there was a viewport that allowed us to directly monitor the 2D MOT—and if we had a direct measure of the flux of atoms from the production chamber into the science chamber—we could more easily troubleshoot whatever causes the decrease in atom number in the BEC.

B.3 The Ugly

The breadboards around the vacuum chamber. There are a total of 6 breadboards around the vacuum chamber[2], 4 on the intermediate level and two

[1] We hypothesized that a glass-metal seal broke—the temperature rating of the fused silica windows (200°C) was not exceeded during bakeout—, we do not know for sure what was the source of the leak. All windows were replaced with new parts.

[2] Not counting the breadboard mounted on the top coil form.

on the upper level. One of the disadvantages of having multiple breadboards is that the number of posts holding them in place restricts laying out optics around the chamber. The second disadvantage is that they are not fully attached to one another and vibrations between them pose a concern regarding pointing stability of the laser beams. A design that seems more convenient is the one implemented in the Sr II laboratory, documented in the dissertation of Neal Pisenti [100] (see figure 6.2 in his disseration), which consists on two large breadboards held by only six posts around the edge.

Finally, a word of caution in regards to the upper breadboards. All the optics for vertical imaging and projection[3] are mounted on the two upper level breadboards—the launching fiber for the DMD beam, the DMD and the Andor camera are all on one breadboard, the rest of the optics are on another breadboard—, I have clamped both of the breadboards together using two clamps (Thorlabs BA2), if the clamps are repositioned, based on my experience, both the DMD and the Andor path will be misaligned. Realigning the Andor camera is trivial since the probe can be used as a guide; however, realigning the DMD path is more convoluted, I suggest following the procedure described in appendix A.9.

The booster pump(s). We have killed about 4 booster water pumps (Berkeley Model MGPS7D), see Fig. B.4 for proof of this claim, it appears that this model is not ideal for our application since they are designed for high flow rates; however, our plumbing system has a high flow resistance—the result of long and narrow conduits—. If the pump breaks again one should consider replacing it with a model

[3]With the exception of the objective which is mounted as described in appendix A.

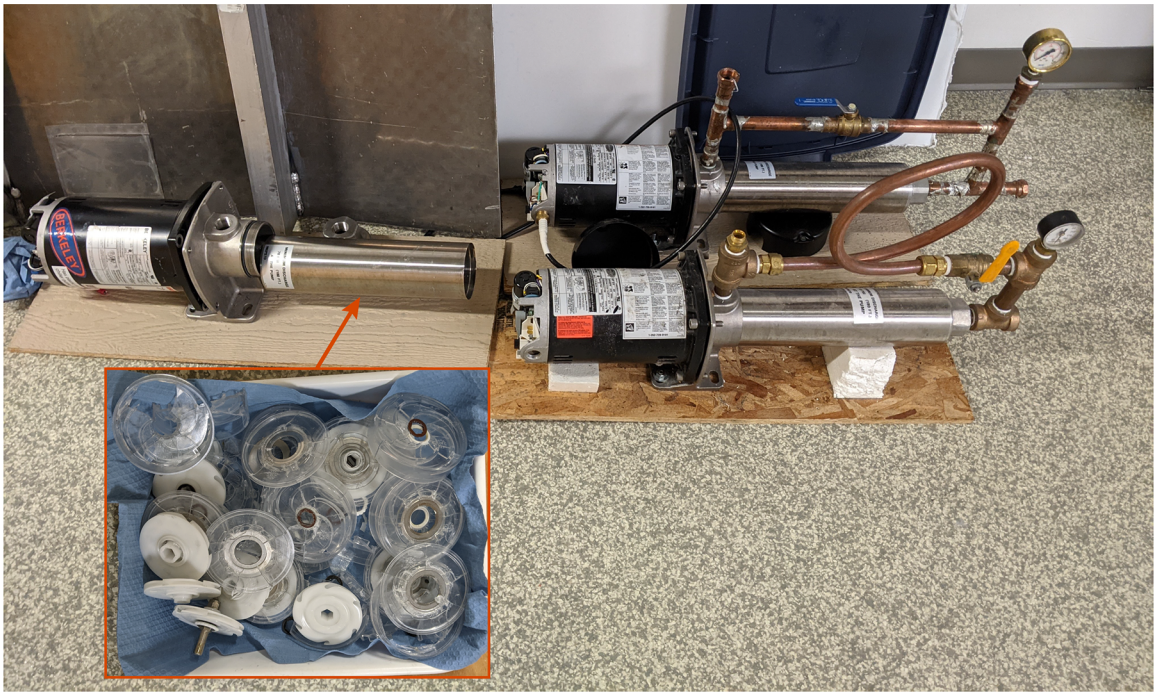

Figure B.4: Booster pump graveyard. The inset shows the shattered impellers that came out of one of the pumps.

better suited for our application.

The rust. There are some signs of rust in the copper wire that makes up the magnetic coils. We have always used Optishield Plus properly[4] to prevent corrosion, yet some of the brass Swagelok connections already show signs of rusting. Figure B.5 shows on panel (a) a segment of copper tube that was replaced with plastic tubing after the copper tubing came apart while servicing the water manifold, (b) shows the point where the Swagelock threaded connection split in two, half of it is stuck inside the receiving connector, which renders it useless. My suggestion is to weld enough replacement parts to have at hand in (the likely) case that more break.

[4]According to the manufacturer the system must be purged and replenished with fresh optishield plus solution once a year or whenever the pH drops below 9.0.

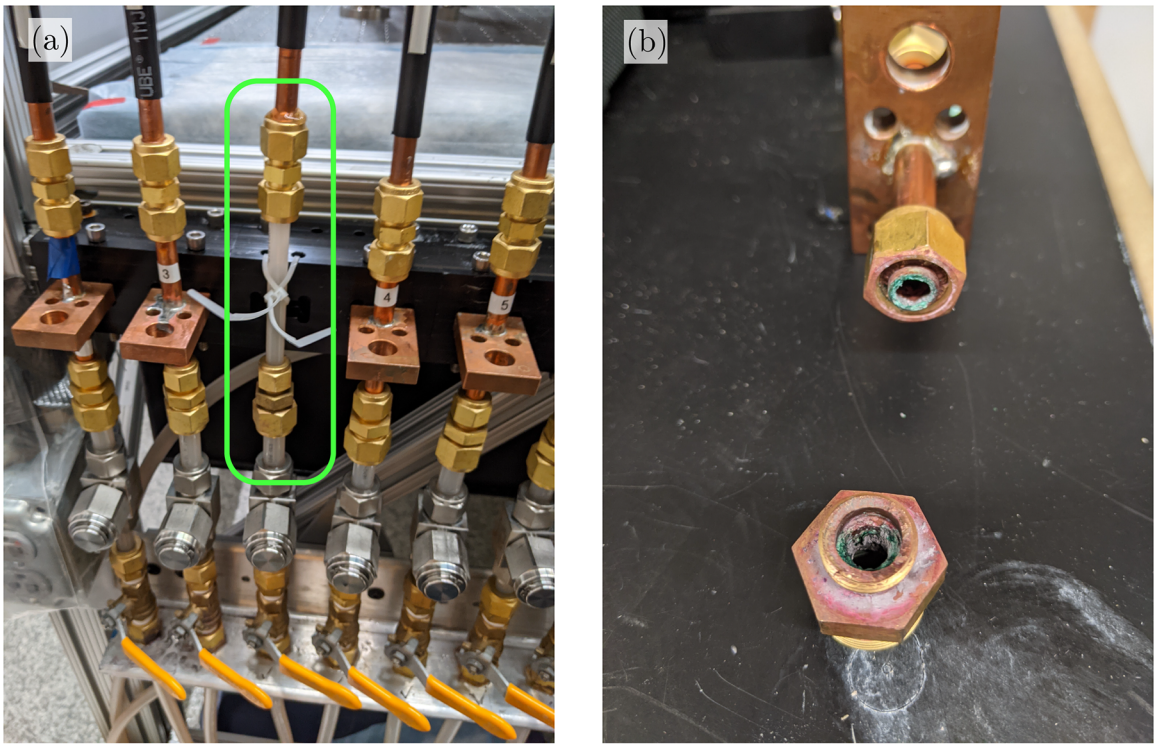

Figure B.5: Patchwork on the magnetic coils water manifold. (a) section of copper tube that was replaced with plastic tubing after the tubing came apart due to rusting (b).

Bibliography

[1] Daniel Steck. Sodium D Line Data, 2000.

[2] I Appenzeller. *Introduction to astronomical spectroscopy*. Cambridge University Press, Cambridge, 2013.

[3] Germain Rousseaux, Christian Mathis, Philippe Maïssa, Thomas G Philbin, and Ulf Leonhardt. Observation of negative-frequency waves in a water tank: a classical analogue to the hawking effect? *New J. Phys*, page 053015, May 2008.

[4] L.-P. Euvé, F. Michel, R. Parentani, T. G. Philbin, and G. Rousseaux. Observation of noise correlated by the hawking effect in a water tank. *Phys. Rev. Lett.*, 117:121301, Sep 2016.

[5] Thomas G. Philbin, Chris Kuklewicz, Scott Robertson, Stephen Hill, Friedrich Königl, and Ulf Leonhardt. Fiber-optical analog of the event horizon. *Science*, 319:1367–1370, Mar 2008.

[6] E. Rubino, J. McLenaghan, S. C. Kehr, F. Belgiorno, D. Townsend, S. Rohr, C. E. Kuklewicz, U. Leonhardt, F. König, and D. Faccio. Negative-frequency resonant radiation. *Phys. Rev. Lett.*, 108:253901, Jun 2012.

[7] H. S. Nguyen, D. Gerace, I. Carusotto, D. Sanvitto, E. Galopin, A. Lemaître, I. Sagnes, J. Bloch, and A. Amo. Acoustic black hole in a stationary hydrodynamic flow of microcavity polaritons. *Phys. Rev. Lett.*, 114:036402, Jan 2015.

[8] C. M. Wilson, G. Johansson, A. Pourkabirian, M. Simoen, J. R. Johansson, T. Duty, F. Nori, and P. Delsing. Observation of the dynamical casimir effect in a superconducting circuit. *Nature*, 479:376–379, Nov 2011.

[9] Matthias Wittemer, Frederick Hakelberg, Philip Kiefer, Jan-Philipp Schröder, Christian Fey, Ralf Schützhold, Ulrich Warring, and Tobias Schaetz. Phonon pair creation by inflating quantum fluctuations in an ion trap. *Phys. Rev. Lett.*, 123:180502, Oct 2019.

[10] J.-C. Jaskula, G. B. Partridge, M. Bonneau, R. Lopes, J. Ruaudel, D. Boiron, and C. I. Westbrook. Acoustic analog to the dynamical casimir effect in a bose-einstein condensate. *Phys. Rev. Lett.*, 109:220401, Nov 2012.

[11] F. Belgiorno, S. L. Cacciatori, M. Clerici, V. Gorini, G. Ortenzi, L. Rizzi, E. Rubino, V. G. Sala, and D. Faccio. Hawking radiation from ultrashort laser pulse filaments. *Phys. Rev. Lett.*, 105:203901, Nov 2010.

[12] Jeff Steinhauer. Observation of quantum hawking radiation and its entanglement in an analogue black hole. *Nature Physics*, 12(10):959–965, August 2016.

[13] Theo Torres, Sam Patrick, Antonin Coutant, Maurício Richartz, Edmund W. Tedford, and Silke Weinfurtner. Rotational superradiant scattering in a vortex flow. *Nature Physics*, 13:833–836, 2017.

[14] C. Cao, E. Elliott, J. Joseph, H. Wu, J. Petricka, T. Schäfer, and J. E. Thomas. Universal quantum viscosity in a unitary fermi gas. *Science*, 331(6013):58–61, 2011.

[15] W. G. Unruh. Experimental black-hole evaporation? *Phys. Rev. Lett.*, 46:1351–1353, May 1981.

[16] Jeff Steinhauer. Observation of self-amplifying hawking radiation in an analogue black-hole laser. *Nature Physics*, 10(11):864–869, 2014.

[17] Y. Ohashi, H. Tajima, and P. van Wyk. Bcs–bec crossover in cold atomic and in nuclear systems. *Progress in Particle and Nuclear Physics*, 111:103739, 2020.

[18] Victor I. Kolobov, Katrine Golubkov, Juan Ramón Muñoz de Nova, and Jeff Steinhauer. Observation of stationary spontaneous hawking radiation and the time evolution of an analogue black hole. *Nature Physics*, 17(3):362–367, 2021.

[19] L. J. Garay, J. R. Anglin, J. I. Cirac, and P. Zoller. Sonic analog of gravitational black holes in bose-einstein condensates. *Phys. Rev. Lett.*, 85:4643–4647, Nov 2000.

[20] Carlos Barceló, S. Liberati, and Matt Visser. Probing semiclassical analog gravity in bose-einstein condensates with widely tunable interactions. *Phys. Rev. A*, 68:053613, Nov 2003.

[21] Uwe R. Fischer and Ralf Schützhold. Quantum simulation of cosmic inflation in two-component bose-einstein condensates. *Phys. Rev. A*, 70:063615, Dec 2004.

[22] S. Eckel, A. Kumar, T. Jacobson, I. B. Spielman, and G. K. Campbell. A rapidly expanding bose-einstein condensate: An expanding universe in the lab. *Phys. Rev. X*, 8:021021, Apr 2018.

[23] A. Einstein. Quantentheorie des einatomigen idealen gases. *Sitzungber. Preuss.*, 9:3–14, 1925.

[24] Bose. Plancks gesetz und lichtquantenhypothese. *Zeitschrift für Physik*, 26(1):178–181, December 1924.

[25] F. London. The λ-phenomenon of liquid helium and the bose-einstein degeneracy. *Nature*, 141(3571):643–644, April 1938.

[26] M H Anderson, J R Ensher, M R Matthews, C E Wieman, and E A Cornell. Observation of Bose-Einstein Condensation in a Dilute Atomic Vapor. *Science*, 269(5221):198–201, jul 1995.

[27] K B Davis, M. O. Mewes, M R Andrews, N. J. van Druten, D S Durfee, D M Kurn, and W Ketterle. Bose-Einstein Condensation in a Gas of Sodium Atoms. *Physical Review Letters*, 75(22):3969–3973, nov 1995.

[28] L. P. Pitaevskii and S. Stringari. *Bose-Einstein condensation*. Clarendon Press, Oxford, 2003.

[29] Christopher Pethick. *Bose-Einstein condensation in dilute gases*. Cambridge University Press, Cambridge New York, 2008.

[30] W. Ketterle, D. S. Durfee, and D. M. Stamper-Kurn. Making, probing and understanding Bose-Einstein condensates. In M. Inguscio, S. Stringari, and C.E. Wieman, editors, *Proceedings of the International School of Physics "Enrico Fermi"*, volume 140, pages 67–176. IOS Press, 1999.

[31] M. Kardar. *Statistical Physics of Particles*. Cambridge University Press, 2007.

[32] R. K. Pathria. *Statistical mechanics*. Academic Press, Boston, 2011.

[33] Silvio Salinas. *Introduction to statistical physics*. Springer, New York, 2001.

[34] James Sethna. *Statistical mechanics : entropy, order parameters, and complexity*. Oxford University Press, Oxford New York, 2006.

[35] N. Bogoliubov. On the theory of superfluidity. *Acad. Sci. USSR. J. Phys.*, 11(1):23–32, 1947.

[36] J. J. Sakurai. *Modern quantum mechanics*. Benjamin/Cummings, Menlo Park, Calif, 1985.

[37] Franz Schwabl. *Quantum mechanics*. Springer, Berlin New York, 2007.

[38] H. J. Miesner, D. M. Stamper-Kurn, M. R. Andrews, D. S. Durfee, S. Inouye, and W. Ketterle. Bosonic stimulation in the formation of a Bose-Einstein condensate. *Science*, 279(5353):1005–1007, 1998.

[39] Eugene P. Gross. Hydrodynamics of a superfluid condensate. *Journal of Mathematical Physics*, 4(2):195–207, February 1963.

[40] L.P. Pitaevskii. *Zh. Eksp. Teor. Fys.*, 40:646, 1961.

[41] Franco Dalfovo, Stefano Giorgini, Lev P. Pitaevskii, and Sandro Stringari. Theory of bose-einstein condensation in trapped gases. *Rev. Mod. Phys.*, 71:463–512, Apr 1999.

[42] Y. Castin and R. Dum. Bose-einstein condensates in time dependent traps. *Physical Review Letters*, 77(27):5315–5319, 1996.

[43] D. S. Jin, J. R. Ensher, M. R. Matthews, C. E. Wieman, and E. A. Cornell. Collective Excitations of a Bose-Einstein Condensate in a Dilute Gas. In *Physical Review Letters*, volume 77, pages 457–460. WORLD SCIENTIFIC, jan 1996.

[44] Stephen Eckel and Ted Jacobson. Phonon Redshift and Hubble Friction in an Expanding BEC. *SciPost Phys.*, 10:64, 2021.

[45] Adam R. Brown. Hyperbolic Inflation. *Physical Review Letters*, 121(25):251601, 2018.

[46] J. M. Gomez Llorente and J. Plata. Expanding ring-shaped Bose-Einstein condensates as analogs of cosmological models: Analytical characterization of the inflationary dynamics. *Physical Review A*, 100(4):43613, 2019.

[47] Carlos Barceló, Stefano Liberati, and Matt Visser. Analogue Gravity. *Living Reviews in Relativity*, 14(1):3, dec 2011.

[48] Ming-Chiang Chung and Aranya B Bhattacherjee. Damping in 2d and 3d dilute bose gases. *New Journal of Physics*, 11(12):123012, dec 2009.

[49] Marlan O. Scully and M. Suhail Zubairy. *Quantum Optics*. Cambridge University Press, 1997.

[50] H.J. Metcalf and P. van der Straten. *Laser Cooling and Trapping*. Springer-Verlag New York Inc., New York, 1999.

[51] C.J. Foot. *Atomic Physics*. Oxford University Press Inc., New York, 2005.

[52] W. Demtroder. *Atoms, molecules and photons: an introduction to atomic-molecular and quantum-physiscs*. Springer, Berlin, 2006.

[53] Ettore Majorana. Atomi orientati in campo magnetico variabile. *Il Nuovo Cimento (1924-1942)*, 9(2):43–50, Feb 1932.

[54] Wolfgang Petrich, Michael H. Anderson, Jason R. Ensher, and Eric A. Cornell. Stable, tightly confining magnetic trap for evaporative cooling of neutral atoms. *Phys. Rev. Lett.*, 74:3352–3355, Apr 1995.

[55] Y.-J. Lin, A. R. Perry, R. L. Compton, I. B. Spielman, and J. V. Porto. Rapid production of ^{87}Rb bose-einstein condensates in a combined magnetic and optical potential. *Phys. Rev. A*, 79:063631, Jun 2009.

[56] L Allen. *Optical resonance and two-level atoms*. Dover, New York, 1987.

[57] Klaus Hueck, Niclas Luick, Lennart Sobirey, Jonas Siegl, Thomas Lompe, Henning Moritz, Logan W. Clark, and Cheng Chin. Calibrating high intensity absorption imaging of ultracold atoms. *Optics Express*, 25(8):8670, apr 2017.

[58] Anand Ramanathan, Sérgio R. Muniz, Kevin C. Wright, Russell P. Anderson, William D. Phillips, Kristian Helmerson, and Gretchen K. Campbell. Partial-transfer absorption imaging: A versatile technique for optimal imaging of ultracold gases. *Review of Scientific Instruments*, 83(8):083119, 2012.

[59] Erin Marshall Seroka, Ana Valdés Curiel, Dimitrios Trypogeorgos, Nathan Lundblad, and Ian B Spielman. Repeated measurements with minimally destructive partial-transfer absorption imaging. *Optics Express*, 27(25):36611, 2019.

[60] Anand Krishnan Ramanathan. *A Ring With a Spin: Superfluidity in a Toroidal Bose-Einstein Condensate*. PhD thesis, University of Maryland, College Park, 2011.

[61] Avinash Kumar. *Experiments with a superfluid BEC ring*. PhD thesis, 2018.

[62] G. Lamporesi, S. Donadello, S. Serafini, and G. Ferrari. Compact high-flux source of cold sodium atoms. *Review of Scientific Instruments*, 2013.

[63] Giacomo Colzi, Gabriele Ferrari, Giacomo Lamporesi, Thomas Bourdel, Leonardo Fallani, and Leonardo Ricci. *A new apparatus to simulate fundamental interactions with ultracold atoms*. Phd thesis, Università degli Studi di Trento, 2018.

[64] Daryl W. Preston. Doppler-free saturated absorption: Laser spectroscopy. *American Journal of Physics*, 64(11):1432–1436, nov 1996.

[65] Jürgen Appel, Andrew MacRae, and A. I. Lvovsky. A versatile digital GHz phase lock for external cavity diode lasers. *Measurement Science and Technology*, 20(5), 2009.

[66] Nathan Llewellyn Smith. *The Tilting Mode and Two Dimensional Confinement of a Bose-Einstein Condensed Gas*. PhD thesis, Oxford, 2005.

[67] N L Smith, W H Heathcote, G Hechenblaikner, E Nugent, and C J Foot. Quasi-2d confinement of a BEC in a combined optical and magnetic potential. *Journal of Physics B: Atomic, Molecular and Optical Physics*, 38(3):223–235, jan 2005.

[68] Eugene Hecht. *Optics*. Addison-Wesley, Reading, Mass, 2002.

[69] Max Born. *Principles of optics : electromagnetic theory of propagation, interference and diffraction of light*. Cambridge University Press, Cambridge New York, 1999.

[70] Joseph Goodman. *Introduction to Fourier optics*. McGraw-Hill, New York, 1996.

[71] Texas Instruments. Using lasers with DLP DMD technology. Technical Report TI DN 2509927, Sep 2008.

[72] G. Gauthier, I. Lenton, N. McKay Parry, M. Baker, M. J. Davis, H. Rubinsztein-Dunlop, and T. W. Neely. Direct imaging of a digital-micromirror device for configurable microscopic optical potentials. *Optica*, 3(10):1136–1143, 2016.

[73] Wolfgang Ketterle, Kendall B. Davis, Michael A. Joffe, Alex Martin, and David E. Pritchard. High densities of cold atoms in a dark spontaneous-force optical trap. *Phys. Rev. Lett.*, 70:2253–2256, Apr 1993.

[74] J. Dalibard and C. Cohen-Tannoudji. Laser cooling below the doppler limit by polarization gradients: simple theoretical models. *Journal of the Optical Society of America B*, 6(11):2023, November 1989.

[75] K. M. O'Hara, M. E. Gehm, S. R. Granade, and J. E. Thomas. Scaling laws for evaporative cooling in time-dependent optical traps. *Physical Review A - Atomic, Molecular, and Optical Physics*, 64(5):4, 2001.

[76] J.F. Jarvis, C.N. Judice, and W.H. Ninke. A survey of techniques for the display of continuous tone pictures on bilevel displays. *Computer Graphics and Image Processing*, 5(1):13–40, 1976.

[77] G. Edward Marti, Ryan Olf, and Dan M. Stamper-Kurn. Collective excitation interferometry with a toroidal bose-einstein condensate. *Physical Review A*, 91(1):013602, jan 2015.

[78] N. Katz, J. Steinhauer, R. Ozeri, and N. Davidson. Beliaev damping of quasiparticles in a bose-einstein condensate. *Phys. Rev. Lett.*, 89:220401, Nov 2002.

[79] S. Banik, M. Gutierrez Galan, H. Sosa-Martinez, M. Anderson, S. Eckel, I. B. Spielman, and G. K. Campbell. Hubble Attenuation and Amplification in Expanding and Contracting Cold-Atom Universes. 02(3):1–5, 2021.

[80] A Kumar, N Anderson, W D Phillips, S Eckel, G K Campbell, and S Stringari. Minimally destructive, doppler measurement of a quantized flow in a ring-shaped bose–einstein condensate. *New Journal of Physics*, 18(2):025001, feb 2016.

[81] Jeff Steinhauer, Murad Abuzarli, Tangui Aladjidi, Tom Bienaimé, Clara Piekarski, Wei Liu, Elisabeth Giacobino, Alberto Bramati, and Quentin Glorieux. Analogue cosmological particle creation in an ultracold quantum fluid of light. 02 2021.

[82] J. M. Gomez Llorente and J. Plata. Expanding ring-shaped bose-einstein condensates as analogs of cosmological models: Analytical characterization of the inflationary dynamics. *Phys. Rev. A*, 100:043613, Oct 2019.

[83] P. O. Fedichev and U. R. Fischer. Gibbons-Hawking effect in the sonic de Sitter space-time of an expanding Bose-Einstein-condensed gas. *Phys. Rev. Lett.*, 91:240407, 2003.

[84] P. O. Fedichev and U. R. Fischer. "Cosmological" quasiparticle production in harmonically trapped superfluid gases. *Phys. Rev. A*, 69:033602, March 2004.

[85] Angus Prain, Serena Fagnocchi, and Stefano Liberati. Analogue cosmological particle creation: quantum correlations in expanding Bose-Einstein condensates. *Phys. Rev. D*, 82:105018, 2010.

[86] E. A. Calzetta and B. L. Hu. Early universe quantum processes in BEC collapse experiments. *Int. J. Theor. Phys*, 44:1691–1704, October 2005.

[87] Antonin Coutant and Silke Weinfurtner. An acoustic probe for quantum vorticity in bose-einstein condensates. *arXiv:1504.00691*, 04 2015.

[88] Uwe R. Fischer and Matt Visser. Riemannian Geometry of Irrotational Vortex Acoustics. *Phys. Rev. Lett.*, 88:110201, 2002.

[89] Y. R. P. Sortais, H. Marion, C. Tuchendler, A. M. Lance, M. Lamare, P. Fournet, C. Armellin, R. Mercier, G. Messin, A. Browaeys, and P. Grangier. Diffraction-limited optics for single-atom manipulation. *Phys. Rev. A*, 75:013406, Jan 2007.

[90] Waseem S Bakr, Jonathon I Gillen, Amy Peng, Simon Fölling, and Markus Greiner. A quantum gas microscope for detecting single atoms in a Hubbard-regime optical lattice. *Nature*, 462(7269):74–77, 2009.

[91] Wolfgang Alt. An objective lens for efficient fluorescence detection of single atoms. *Optik*, 113(3):142–144, 2001.

[92] L M Bennie, P T Starkey, M Jasperse, C J Billington, R P Anderson, and L D Turner. A versatile high resolution objective for imaging quantum gases. *Opt. Express*, 21(7):9011–9016, 2013.

[93] J. D. Pritchard, J. A. Isaacs, and M. Saffman. Long working distance objective lenses for single atom trapping and imaging. *Review of Scientific Instruments*, 87(7), 2016.

[94] Daniel Schaeder Barker. *Degenerate Gases of Strontium for Studies of Quantum Magnetism*. PhD thesis, 2016.

[95] Francisco Salces Carcoba. *Microscopy Of Elongated Superfluids*. Phd, University of Maryland, 2020.

[96] Xiaolin Li, Min Ke, Bo Yan, and Yuzhu Wang. Reduction of interference fringes in absorption imaging of cold atom cloud using eigenface method. *Chinese Optics Letters*, 5(3):128–130, 2007.

[97] C. F. Ockeloen, A. F. Tauschinsky, R. J.C. Spreeuw, and S. Whitlock. Detection of small atom numbers through image processing. *Physical Review A - Atomic, Molecular, and Optical Physics*, 82(6), 2010.

[98] Steven Brunton. *Data-driven science and engineering : machine learning, dynamical systems, and control*. Cambridge University Press, Cambridge, United Kingdom New York, NY, 2019.

[99] Ana Valdes Curiel. *Topological dispersion relations in spin-orbit coupled Bose gases*. PhD thesis, University of Maryland, 2019.

[100] Neal Pisenti. *Isotope Shift Spectroscopy Of Ultracold Strontium*. PhD thesis, 2019.